The wave shapes of alpha – Cross-frequency relationships in the resting human brain

Dissertation

zur Erlangung des Grades eines

Doktors der Naturwissenschaften

der Mathematisch-Naturwissenschaftlichen Fakultät

und

der Medizinischen Fakultät

der Eberhard-Karls-Universität Tübingen

vorgelegt

von

Janet Giehl

aus Dannenberg, Deutschland

2024

Tag der mündlichen Prüfung: 12.09.2024

Dekan der Math.-Nat. Fakultät: Prof. Dr. Thilo Stehle

Dekan der Medizinischen Fakultät: Prof. Dr. Bernd Pichler

1. Berichterstatter: Prof. Dr. Markus Siegel

2. Berichterstatter: Prof. Dr. Andreas Bartels

Prüfungskommission: Prof. Dr. Markus Siegel

Prof. Dr. Andreas Bartels

Prof. Dr. Christoph Braun

Prof. Dr. Steffen Gais

Erklärung / Declaration:

Ich erkläre, dass ich die zur Promotion eingereichte Arbeit mit dem Titel:

"The wave shapes of alpha – Mapping and characterizing cross-frequency relationships in the resting human brain"

selbstständig verfasst, nur die angegebenen Quellen und Hilfsmittel benutzt und wörtlich oder inhaltlich übernommene Stellen als solche gekennzeichnet habe. Ich versichere an Eides statt, dass diese Angaben wahr sind und dass ich nichts verschwiegen habe. Mir ist bekannt, dass die falsche Angabe einer Versicherung an Eides statt mit Freiheitsstrafe bis zu drei Jahren oder mit Geldstrafe bestraft wird.

I hereby declare that I have produced the work entitled "The wave shapes of alpha – Mapping and characterizing cross-frequency relationships in the resting human brain", submitted for the award of a doctorate, on my own (without external help), have used only the sources and aids indicated and have marked passages included from other works, whether verbatim or in content, as such. I swear upon oath that these statements are true and that I have not concealed anything. I am aware that making a false declaration under oath is punishable by a term of imprisonment of up to three years or by a fine.

Tübingen, ...

Datum / Date Unterschrift / Signature

Statement of contributions:

The first project “Dissociating harmonic and non-harmonic phase-amplitude coupling in the human brain” (Giehl et al., 2021; https://doi.org/10.1016/j.neuroimage.2020.117648) uses publicly available data from the Human Connectome Project (HCP S1200) and data that was recorded at the MEG Center Tübingen in part by Jörg Hipp and Anna-Antonia Pape and in part by Janet Giehl. Markus Siegel, Nima Noury and Janet Giehl jointly conceived the concept and scope of the study. Janet Giehl conducted all formal data analysis. Janet Giehl, Markus Siegel and Nima Noury wrote the original draft and edited the manuscript to its final published form.

The second project “The wave shape of oscillations” uses publicly available data from the Human Connectome Project (HCP S1200). Janet Giehl conducted the project at the Department of Neural Dynamics and Magnetoencephalography of the Hertie Institute for Clinical Brain Research under the supervision of Markus Siegel. Markus Siegel and Janet Giehl jointly conceived the concept and scope of the project. Janet Giehl developed the Fourier-based waveform analysis method, conducted all formal data analysis and wrote the original draft. Markus Siegel and Janet Giehl edited the manuscript draft included in this thesis. A later version of this manuscript draft has since been published as Giehl and Siegel, 2024; https://www.biorxiv.org/content/10.1101/2024.03.16.585296v1.

Table of Contents

Table of figures

Abstract

The interaction of different neural networks is essential for cognition and for healthy brain function, and the cross-frequency interactions between different neuronal oscillations have been hypothesized to coordinate such interactions. However, little is understood about the distribution and the nature of the cross-frequency relationships in the human brain.

A prominently researched mode of cross-frequency interaction has been phase-amplitude coupling (PAC). Here, the phase of a low frequency oscillation is associated with the amplitude of a high frequency oscillation. As a methodological complication, however, measures for PAC do not only reflect the presence of a phase-to-amplitude interaction between two distinct oscillations, but they also reflect the presence of a neuronal single oscillation with a non-sinusoidal waveform. In the case of a non-sinusoidal waveform, the measured cross-frequency relationship reflects the wave shape of the oscillation. The underlying mechanisms and functions of two distinct oscillations that are phase-amplitude coupled to one-another differ from those of a a single oscillation with a particular waveform. Therefore, a clear dissociation between the two cases is essential to gain a meaningful understanding of the cross-frequency relationships in the human brain.

In the first study of this thesis, we systematically mapped PAC across the human cortex, and in a wide range of frequency pairs using magnetoencephalography (MEG) and source reconstruction. We distinguished neuronal PAC from non-neuronal PAC related to muscle activity and eye-movements, and we showed that phase-amplitude, phase-phase (PPC), and amplitude-amplitude (AAC) cross-frequency coupling measures are all sensitive to signals with higher harmonics. We used these measures in conjunction to dissociate non-harmonic and harmonic PAC. We found no evidence of non-harmonic PAC in the resting human brain. Instead, we observed widespread PAC that was driven by harmonic signals, predominantly in the alpha frequency range. That is, we observed widespread alpha oscillations with non-sinusoidal wave shape.

The results of the first study raised the question whether alpha oscillations in different brain areas may have different wave shapes. That is, if the wave shape of oscillations observed in human resting state MEG might be functionally relevant. To address this question in the second study, we first, determined spatial peaks of theta/alpha wave-shape stability using MEG, source-reconstruction and bicoherence. Then we assessed the wave shapes at these regions of interest (ROIs) with a novel method. With this method, wave shapes were analyzed in the frequency domain, by exploiting the characteristic cross-frequency patterns of signals with higher harmonics. We tested for wave-shape differences and distinguished six statistically different alpha wave shapes: three corresponding to the well-established functionally distinct sensorimotor-, occipital- and temporal alpha rhythms, and three additional parietal alpha waveforms.

These studies, to our best knowledge for the first time, systematically characterized the distribution and the nature of cross-frequency signals in the resting human brain. We showed that non-sinusoidal wave shapes were a prevalent phenomenon in the human cortex that dominated all observable cross-frequency patterns. Furthermore, we demonstrated that the characteristic cross-frequency patterns of non-sinusoidal wave shapes can be used to differentiate what are likely functionally distinct rhythms. Periodic wave shapes can be reconstructed in detail from their characteristic cross-frequency patterns, and the wave shape of oscillations might reflect rich information about underlying circuit physiology.

1 Introduction

The human brain is a highly complex system that allows us to perceive our environment, to remember our past, to imagine, to reason, to make decisions, and to actively shape our own future. Cognition depends not only on the different neural networks to each fulfill their own specific functions. The coordinated functional interplay between these different networks is equally essential (Canolty and Knight, 2010; Lakatos et al., 2005; Palva, 2005; Siegel et al., 2012).

Electrophysiology allows an insight into dynamic processing of neuronal networks with a millisecond temporal resolution. Possible spatial scales range from the recording of single-neuron activity, over the local field potential (LFP) that is measuring the combined activity of populations of tens of thousands of neurons and the electrocorticogram (ECoG) that is recorded with electrodes placed on the surface of the brain, up to non-invasive brain imaging techniques such as electroencephalography (EEG) or MEG with sensors distributed over the entire head (Buzsáki and Draguhn, 2004; Canolty and Knight, 2010). A common link between these spatial scales is the possibility to observe neuronal oscillations at all of these vastly different levels (Buzsáki and Draguhn, 2004; Canolty and Knight, 2010). Thus, neural oscillations can serve as a bridge between single-neuron activity and behavior, across all of the different spatial scales from large-scale non-invasive recordings to invasive single-neuron recordings (Buzsáki and Draguhn, 2004).

Neural oscillations occur in different frequency bands. These frequency bands can be roughly subdivided into delta (0.5-4 Hz), theta (4-8 Hz), alpha (8-12 Hz), beta (12-30 Hz), gamma (30-80 Hz) and a fast band (80-200 Hz) (Buzsaki, 2006; Buzsáki and Draguhn, 2004). The different frequency bands have been associated with different spatial scales of neural activity, with distinct neural functions and different brain states (Buzsaki, 2006; Canolty and Knight, 2010; Siegel et al., 2012).

The correlations between neural oscillations and cognitive functions demonstrated, that there seems to be a link between the two. However, this

link does not explain how oscillations subserve cognition. The mechanistic function that a single oscillation can have in the brain is relatively limited. One oscillation can establish a certain – indefinitely repeating – functional time window. By providing such functional time windows, one single oscillation can already provide a mechanistic explanation for how different brain areas interact with each other and how they transfer information efficiently and selectively between one another (Fries, 2015, 2005; Jensen and Mazaheri, 2010). The functional integration of two oscillations with different frequencies could combine two timing mechanisms operating at different scales. Such linked oscillations and linked timing mechanisms could explain functions that are qualitatively even more complex than the functions that could be explained by a sum of independent single oscillations with independent timing mechanisms. One example for how cross-frequency interactions might subserve cognition could be found in working memory: the interaction between theta and gamma oscillations has been suggested to be the functional mechanism of working memory encoding, of the maintenance of a sequence of items in working memory, and of the working-memory capacity limit of 7±2 items (Jensen and Lisman, 2005; Lisman and Idiart, 1995).

From a general perspective, it has been hypothesized, that cross-frequency interactions regulate the integration between oscillations of distinct frequency bands, and that they, in this way, regulate the integration between the different neuronal network computations that have been associated with the respective oscillations (Canolty and Knight, 2010). Hence, a well-regulated interplay between different neural networks that each serve different neural functions can be expected to be essential for normal cognition and for normal brain function. Therefore, cross-frequency coupling (CFC) between neural oscillations has been hypothesized to be a functionally significant mechanistic feature of brain function (Jensen and Colgin, 2007),

Likely due to this potential as a mechanism of higher brain functions, such as working memory, cross-frequency interactions have received considerable and increasing interest in recent years (Lisman and Idiart, 1995; Jensen and Colgin, 2007; Canolty and Knight, 2010; Tort et al., 2010; Jensen et al., 2012;

Aru et al., 2015; Colgin, 2015; Hyafil et al., 2015; McLelland and VanRullen, 2016; Dvorak and Fenton, 2014; Fell and Axmacher, 2011; Siebenhühner et al., 2020; Yakubov et al., 2022; Csicsvari et al., 2003). Two types of cross-frequency coupling received the most interest: cross-frequency phase coupling (phase-phase synchronization) and cross-frequency phase-amplitude coupling (PAC), which is characterized as the phase of a low-frequency oscillation modulating the power of a high frequency oscillation (Canolty et al., 2006; Canolty and Knight, 2010). From a theoretical point of view, there are two additional options: cross-frequency phase-frequency coupling, which is the phase of a slower oscillation modulating the frequency of a faster modulation, and amplitude-amplitude coupling, which is the power of one oscillation modulating the power of an oscillation with a different frequency (Jensen and Colgin, 2007). However, only phase-phase and phase-amplitude coupling have also been associated with clearly plausible physiological mechanisms of cross-frequency interaction (Canolty and Knight, 2010).

The precise physiological mechanisms of PPC may still remain unknown, but the observation of spiking activity that can be phase-locked to oscillations of different frequencies suggests, that this mechanism deserves further investigation (Canolty and Knight, 2010). Cells that are resonant at more than one frequency may play an important role (Fujisawa and Buzsáki, 2011). Such cells or circuits could serve as a common pacemaker across different frequencies, or as a frequency converter mediating the phase-synchronization between distinct oscillations with an integer-multiple frequency relationship (Fujisawa and Buzsáki, 2011). Poly-resonant cells or circuits could, thus, be involved in the orchestration and the functional integration of networks and of activity that operate at different rates.

Phase-amplitude coupling, on the other hand, could physiologically be generated by a lower frequency rhythm that reflects local neuronal excitability, e.g., in the theta frequency range. The phase of this rhythm would then modulate the amplitude of spontaneous local gamma oscillations (Jensen and Colgin, 2007). This mechanism could emerge, e.g., when inhibitory interneurons with slow GABAergic inhibition that contribute to the theta rhythm,

are connected to inhibitory interneurons with fast GABAergic feedback suppression that contribute to the spontaneous gamma rhythm (White et al., 2000). Depending on the depth of the modulation that theta imposes on gamma, this could be reflected as either pure phase-amplitude coupling, or it could be reflected as phase-amplitude coupling with concurrent phase-phase coupling. Concurrent phase-amplitude and phase-phase coupling could emerge, when a gamma oscillation and associated excitatory neuronal firing is effectively suppressed entirely during a defined phase of a theta rhythm, rather than only being reduced in power. The suppressed firing and the first gamma cycle could then reemerge as soon as this suppression subsides, and, thus, the gamma rhythm may appear as cross-frequency phase-locked to the theta rhythm, in addition to the cross-frequency phase-amplitude relationship; with the phase-locking being updated once during each theta cycle.

Phase-amplitude coupling, in particular, has been related to brain function and -dysfunction in numerous instances, including with non-invasive recordings in humans (Abubaker et al., 2021; Canolty and Knight, 2010; Yakubov et al., 2022). PAC has not only been hypothesized to link distinct oscillations and different functional time-scales locally, it has also been suggested that PAC could play an important role for the long-range synchronization of distant brain areas (Jensen and Colgin, 2007; Siebenhühner et al., 2020; van der Meij et al., 2012; von Nicolai et al., 2014; Nandi et al., 2019; González et al., 2020; Bonnefond et al., 2017)

Even though cross-frequency interactions have received considerable attention in recent years, still little is understood about the distribution and the nature of cross-frequency-coupling in the human brain. In this regard, it is essential to consider that measures of cross-frequency coupling may reflect different types of cross-frequency coupling patterns, instead of only reflecting a single cross-frequency-coupling concept of interest. Measured PAC, for example, could reflect a physiological interaction between the phase of one oscillation and the amplitude of a second oscillation and, thus, measured PAC might reflect an interaction between two neuronal oscillations that are physiologically and functionally distinct from one another. Measured PAC could,

however, also reflect cross-frequency patterns that emerge without any underlying physiological coupling between oscillations, e.g., in the form of a single oscillation with a temporally consistent non-sinusoidal wave shape (Aru et al., 2015; Chacko et al., 2018; Cole et al., 2017; Cole and Voytek, 2017; Gerber et al., 2016; Hyafil, 2015; Jensen et al., 2016; Kramer et al., 2008; Lozano-Soldevilla et al., 2016; Vaz et al., 2017; Velarde et al., 2019).

The wave shape of a neuronal oscillation may be understood in a similar way as the tone of a certain musical instrument: the sound of a violin and a piano playing the same musical note (e.g., A4 at 440 Hz) can be distinguished by the different overtones that the respective instruments produce. Overtones are cross-frequency related higher harmonic frequencies. They define the characteristic sound or timbre of an instrument in a very similar way, as the higher harmonics of a non-sinusoidal oscillation define the wave shape of a neuronal oscillation.

These two different examples of cross-frequency patterns – phase-amplitude-coupling- or wave-shape-related – are fundamentally distinct with respect to their generative mechanisms and to their potential neurophysiological functions. However, measures for PAC are equally sensitive to both types of cross-frequency relationships. Thus, measured cross-frequency coupling might either reflect the physiological properties of a single network of neurons, or reflect a physiological interaction between distinct oscillations and networks. (Giehl et al., 2021)

Measured cross-frequency relationships reflect valuable neurophysiological information in either of these two cases: if it is the interaction between the phase and the amplitude of two largely independent oscillations that underlies the measured PAC, as well as if the measured PAC, instead, reflects the characteristic spectral signature of a single non-sinusoidal wave shape. The ambiguity of measured cross-frequency coupling, however, is presenting a significant problem: it is only possible to interpret the observed cross-frequency coupling in a physiologically and mechanistically meaningful way, if a clear distinction between these two fundamentally different cases can be made (Giehl et al., 2021). For this reason, it was essential to not only map phase-

amplitude coupling in the human brain, but to also characterize the nature of these results; in particular, to carefully dissociate between the presence of canonical cross-frequency PAC and the presence of oscillations with non-sinusoidal wave shapes, while also considering physiological and non-physiological artifacts. This dissociation first paved the way to then investigate the resulting cross-frequency features further.

1.1 The aims of this thesis

The aim of this thesis was to map the distribution of phase-amplitude coupling in the human cortex during rest, and to characterize the nature of the observable cross-frequency relationships. To fulfill this aim, it was necessary to solve methodological challenges:

The interpretation of measured PAC is challenging. Measures of PAC are not only sensitive to physiological phase-amplitude coupling between two different oscillations (non-harmonic PAC). PAC measures are also sensitive to signals with higher harmonics, i.e., to signals with a temporally consistent non-sinusoidal wave shape (harmonic PAC) (Aru et al., 2015; Chacko et al., 2018; Cole et al., 2017; Cole and Voytek, 2017; Gerber et al., 2016; Hyafil, 2015; Jensen et al., 2016; Kramer et al., 2008; Lozano-Soldevilla et al., 2016; Vaz et al., 2017; Velarde et al., 2019). The harmonics of a wave shape are, by definition, phase-phase and amplitude-amplitude coupled to one-another. Thus, PPC and cross-frequency amplitude-amplitude coupling (AAC) measures are also sensitive to these signals. Thus, the results from all these CFC measures are inherently ambiguous, and it is challenging to characterize the functional nature of the measured cross-frequency relationships correctly. We aimed to combine these CFC measures to dissociate the different cross-frequency patterns of non-harmonic and harmonic PAC. (Giehl et al., 2021)

When phase-amplitude coupling between two distinct oscillations has been confirmed as the cause of measured CFC, the relationship between the involved oscillations can be characterized using available cross-frequency coupling measures. When non-sinusoidal wave shapes are the cause of

measured CFC, the situation is different. Most of the available methods that can characterize wave shapes operate in the time domain (Cole and Voytek, 2017), which is, however, associated with signal-to-noise related limitations (Bartz et al., 2019). This presents a limiting factor for the analysis of neuronal wave shapes; especially, but not only, in non-invasive recordings. As an additional significant limitation, all currently available wave-shape analysis methods that could be applied to neuronal data analyze only a select number of specific wave-shape features – therefore, these wave-shape analysis methods do not capture all potentially relevant wave-shape features (Cole and Voytek, 2017). The information that waveshapes could potentially provide about underlying physiological network properties is, however, directly limited by the accuracy to which a wave-shape analysis method can represent different wave shapes. Thus, the information that could potentially be gained from non-sinusoidal wave shapes about underlying physiological network properties has not yet been fully utilized by the currently available methods. This thesis aimed to overcome these limitations.

The aims of this thesis can be summarized as follows:

First, to map the spatial and spectral distribution of cross-frequency relationships in the human cortex and to carefully investigate the nature of the observed cross-frequency relationships. That is, to dissociate non-neuronal and neuronal PAC, and to dissociate non-harmonic and harmonic PAC. (Giehl et al., 2021)

Second, to characterize cross-frequency wave-shape features with a novel wave-shape analysis method that substantially increases the accuracy of the wave-shape representation, in combination with optimized signal-to-noise properties. Then, to use this novel method to characterize and to dissociate prominent wave-shape-related cross-frequency relationships in the human cortex. That is, to dissociate what may be functionally distinct alpha oscillations based on their distinguishable waveforms.

Together, the two studies of this thesis aimed to provide well-founded insights into the cross-frequency relationships of large-scale neuronal

oscillations in humans. We aimed to characterize the distribution and the nature of cross-frequency relationships in the resting human brain and to assess the potential functional and physiological relevance of the cross-frequency relationships that can be observed in large scale neural recordings.

The first project of this thesis, “Dissociating harmonic and non-harmonic phase-amplitude coupling in the human brain” corresponds directly to the published paper Giehl et al., 2021. This includes also the first four sections of chapter 3 of this thesis: “From (harmonic) PAC to the wave shape of oscillations“. The second project, “Fourier-based waveform analysis dissociates human cortical alpha rhythms” corresponds to a yet unpublished manuscript draft. This includes also the first four sections of chapter 5 of this thesis with the chapter title “Discussion”.

2 Dissociating harmonic and non-harmonic phase-amplitude coupling in the human brain[1]

(Giehl et al., 2021, https://doi.org/10.1016/j.neuroimage.2020.117648)

2.1 Scientific questions and aims[2]

Phase-amplitude coupling has been a prominently discussed mode of cross-frequency interactions. However, PAC has not been mapped systematically across the human brain and across frequency combinations. Therefore, the question of the distribution of PAC over the human brain, and of the involved frequency bands, remains open.

Furthermore, the interpretation of cross-frequency coupling results is challenging. Phase-amplitude coupling measures, as well as phase-phase and amplitude-amplitude coupling measures, are not only sensitive to interacting oscillations. These measures are all also sensitive to signals with higher harmonics, i.e., signals that contain a periodic, but non-sinusoidal component. In other words: these measures cannot readily distinguish between two interacting oscillations and a single signal with a non-sinusoidal wave shape, such as the typically arch-shaped motor mu rhythm. The two different cases are, however, associated with distinct generative mechanisms. Therefore, a clear distinction is essential for a mechanistically meaningful interpretation of

[1] This entire chapter and the following chapter up to and including section 3.4 correspond to the previously published paper with the same title (Giehl et al., 2021) which can be accessed with the following DOI link: https://doi.org/10.1016/j.neuroimage.2020.117648. While, section 2.1 has been modified and adapted to fit the structure of the present dissertation, the text, and the figures of sections 2.2 to 3.5 with all subsections correspond directly and entirely, word-by-word, to the text and the figures of the corresponding sections of this previously published paper. (Sub-)section titles that differ from the original will be marked separately.

[2] This section corresponds closely to parts of the “abstract” and “introduction” sections of Giehl et al., (2021), which have been adapted to fit the structure of the present dissertation. In consequence, the correspondence of this section 3.1 to the aforementioned sections in Giehl et al. (2021) is close, and some single sentences, or parts of sentences, overlap directly, that is, they correspond word-by-word.

any observation of phase-amplitude coupling, and of cross-frequency signal features in general. In fact, several studies have already cautioned for or reported that harmonic PAC is linked to non-sinusoidal waveform shapes of oscillations rather than the non-harmonic PAC of interest (Aru et al., 2015; Chacko et al., 2018; Cole et al., 2017; Cole and Voytek, 2017; Gerber et al., 2016; Hyafil, 2015; Jensen et al., 2016; Kramer et al., 2008; Lozano-Soldevilla et al., 2016; Vaz et al., 2017; Velarde et al., 2019). Thus, there is an inherent ambiguity in the results from these measures and it is challenging to not only map, but to also characterize the nature of any measured cross-frequency coupling correctly.

In this project, we addressed this question, by evaluating phase-amplitude coupling across a broad range of frequency combinations and the entire human cortex based on two independent source-reconstructed magnetoencephalography (MEG) datasets. We estimated PAC using two different measures: vectorlength-PAC (Canolty et al., 2006) and bicoherence (Shahbazi Avarvand et al. 2018). The first measure established continuity to previous studies, whereas the latter measure provided an increased frequency resolution that is essential for distinguishing between canonical and harmonic PAC.

To test if the measured PAC patterns reflected non-harmonic neuronal PAC, we assessed, first, if these patterns reflect muscle- or eye-movement artifacts, and second, to what extent they are affected by the non-sinusoidal shape of neuronal oscillations. To this end, we devised and systematically applied a novel procedure that allows distinguishing harmonic and non-harmonic PAC, by using phase-amplitude, phase-phase and amplitude-amplitude cross-frequency coupling measures in conjunction.

2.2 Materials and Methods[3]

2.2.1 Datasets

We used resting-state MEG data from two different datasets: the Human Connectome Project MEG data (HCP) (Van Essen et al., 2013), which is publicly available, and an independent MEG dataset recorded at the MEG-Center Tübingen.

2.2.2 Data acquisition

Unless specified otherwise, set-up, recording, and preprocessing of the HCP dataset (HCP S1200 Release), was as previously described (Van Essen et al., 2013). We used the first of three sessions of 6 minutes eyes-open resting-state MEG, which was available for 89 subjects. Subjects were in supine position and fixated a red fixation cross on dark background.

The Tübingen dataset comprised 28 healthy subjects (17 female, mean age 26.5 years), that all gave written informed consent and received monetary compensation. For this dataset, 10 minutes of resting-state MEG were recorded with 275 channels at a sampling rate of 2,343.75 Hz (Omega 2000, CTF Systems, Inc., Port Coquitlam, Canada). Participants were seated upright in a dimly lit magnetically shielded chamber and fixated a central fixation point. The recordings was approved by the local ethics committee and conducted in accordance to the Declaration of Helsinki. All participants gave written informed consent before participating. For both datasets, structural T1-weighted MRIs of all subjects were used to construct individual head and source models.

2.2.3 Preprocessing - HCP dataset

We down sampled the data to 1000 Hz, band-pass filtered between 0.1 and 400 Hz, and notch-filtered between 59 and 61 Hz (and harmonics) using zero-

[3] This section and all subsections correspond precisely to the corresponding section with the same title in Giehl et al., (2021). See also footnote 1 on page 19.

phase 4th-order Butterworth forward and reverse filters. We removed artifactual data segments as defined by the HCP pipeline (baddata). We manually identified and removed muscle-, eye- and heart-related artifacts using ICA (Hipp and Siegel, 2013). Heart-related artifact ICs were removed in all 89 subjects. Eye-related ICs were removed in 86 subjects. In this dataset, muscle-related ICs often contained prominent signal components in the alpha-band. To avoid accidentally removing components that may include neuronal interactions, we did not remove these components. Thus, we removed muscle-ICs in only 30 of the 89 subjects, which resulted in considerable residual muscle activity in this preprocessed dataset.

2.2.4 Preprocessing - Tübingen dataset

The data was down sampled to 1000 Hz, low-pass filtered at 300 Hz, notch-filtered between 49 and 51 Hz (and harmonics) and high-pass filtered at 0.5 Hz using zero-phase 4th-order Butterworth forward and reverse filters. Segments with jumps, eye blinks or strong muscle activity were removed manually in the time domain data. Remaining artifacts were removed using ICA analysis as described above for the HCP dataset. For this dataset, however, we removed muscle-ICs more stringently even if they contained a spectral peak in the alpha-band. Thus, for this dataset muscle-related ICs were removed in all subjects.

2.2.5 Source reconstruction

For both datasets, we used beamforming to reconstruct cortical activity at 457 positions on a shell that covered the entire cortex with even spacing approximately 1 cm beneath the skull (Hipp and Siegel, 2015). For the HCP dataset, we used the spatial transformation matrices that are available in the individual source models provided with the HCP dataset and applied them to our source model. We performed two distinct source space projections and frequency analyses for vectorlength-PAC and all other cross-frequency measures.

2.2.6 Spectral analysis and beamforming for vectorlength-PAC

We employed complex Morlet wavelets with logarithmically spaced center frequencies ranging from $2^{-0.25}$ Hz (~0.84 Hz) to 2^{8} Hz (256 Hz) in quarter-octave steps (factor of $2^{0.25}$).

Optimal for PAC detection is a relatively low frequency resolution for amplitude frequencies that must include the amplitude modulation side-peaks and a relatively high frequency resolution for the phase frequency (Aru et al., 2015). Therefore, we chose bandwidths of 0.5 octaves for the phase frequencies and 1 octave for the amplitude frequencies (bandwidth defined as $\log_2$ of the ratio of the cut-off-frequencies at the filter's half maximum gain). This corresponds to Morlet wavelets with $q = f/\sigma_f \sim 6.86$ for 0.5 octave and $q = f/\sigma_f \sim 3.53$ for 1 octave, where f is each wavelet's central frequency and σ_f is the standard deviation of its Gaussian function in the frequency domain (Tallon-Baudry and Bertrand, 1999). We computed time-frequency estimates with a temporal steps size of 7ms. Subsequently, we applied DICS beamforming with frequency specific filters (Gross et al., 2001) For each source, we computed filters in the dominant dipole direction.

2.2.7 Vectorlength-PAC

We estimated vectorlength phase-amplitude coupling between phase-frequencies (f_φ) of ~0.84 Hz ($2^{-0.25}$ Hz) to 128 Hz (2^{7} Hz) and amplitude-frequencies (f_A) of at least twice the phase frequency. We estimated vectorlength-PAC $V(f_\varphi, f_A)$ according to (Canolty et al., 2006):

$$V(f_\varphi, f_A) = | <_t A(t, f_A) e^{i\varphi(t, f_\varphi)} > |$$

Here, $\varphi(t, f_\varphi)$ is the phase, $A(t, f_A)$ the amplitude, $<_t \ldots>$ is the average over time and |…| is the absolute value.

2.2.8 Spectral analysis and beamforming for other cross-frequency measures

For all other cross-frequency coupling measures (bicoherence, cross-frequency amplitude-amplitude correlation, cross-frequency phase-phase coupling) we performed linearly constrained minimum variance (LCMV) beamforming (Van Veen et al., 1997) to estimate source level activity. This approach preserves the phase relationship between frequencies. The source-data was split into half-overlapping 1 s segments (2 s and 4s segments for two control analyses related to spectral leakage). Each segment was demeaned and a Hanning window was applied. Then, fast Fourier transformation was computed for each segment using zero-padding to 2 or 10 seconds, which results in frequency resolutions of 0.5 or 0.1 Hz, respectively.

2.2.9 Bicoherence

We estimated bicoherence for frequencies f_1 (0.5 to 64 Hz) and f_2 (1 to 200 Hz) in steps of 0.5 Hz with $f_2 \geq f_1 - 3$ Hz and the corresponding $f_3 = f_1 + f_2$ according to the formula with the normalization factor from (Hagihira et al., 2001):

$$b(f_1, f_2) = \frac{|<_t F_t(f_1)F_t(f_2)F_t^*(f_1+f_2)>|}{<_t |F_t(f_1)F_t(f_2)F_t^*(f_1+f_2)|>}$$

Here, $F_t(f)$ is the signal's time-frequency transformation at time t, $|\ldots|$ represents the absolute value, and $<_t \ldots >$ is the average over time. We use the terms "f_3" and "$f_1 + f_2$" interchangeably throughout the paper. Frequencies f_2 smaller than f_1 were included for accurate detection of bicoherence peaks at and close to $f_1 = f_2$, in particular after smoothing of the cross-frequency spectrum.

To locate delta-f_1-range bicoherence peaks, bicoherence was estimated in steps of 0.1 Hz for f_1 (0.1 to 2.5 Hz) and 0.5 Hz for f_2 (0.5 to 50 Hz), with $f_2 \geq f_1$.

2.2.10 Cross-frequency amplitude-amplitude coupling (AAC)

We computed the Pearson correlation coefficients between amplitude time-series, that were derived from the LCMV-beamformed Fourier time-series, between frequencies f_1 (0.5 to 64 Hz) and f_2 (1 to 200 Hz) in steps of 0.5 Hz where $f_2 \geq f_1 + 3$ Hz.

2.2.11 Cross-frequency phase-phase coupling (PPC)

We computed cross-frequency phase-coupling between frequencies n and m weighted and normalized by the signal amplitudes at these frequencies. The phase of the lower frequency n was accelerated by the factor m/n to match the higher frequency m. The resulting measure can be understood as computing coherence between signals of different frequencies.

$$xCoh(f_n, f_m) = \frac{| <_t A_n(t)A_m(t)e^{i\left(\varphi(t)_n * \frac{m}{n} - \varphi(t)_m\right)} > |}{<_t A(t)_n A(t)_m >}$$

$<_t \ldots >$ represents the average over time. Amplitude $A(t)$ and phase estimates $\varphi(t)$ were obtained from the time-frequency Fourier estimates. The measure approaches 0 for a random phase relationship and equals 1 for perfect m/n factor phase-coupling. The normalization matches the normalization used for bicoherence. Furthermore, the weighting by the signal amplitudes improves the robustness of the measure by favoring phase information during times of high signal amplitude. We computed this measure for the same frequency pairs as AAC.

2.2.12 Regions of interest (ROIs)

We defined 4 ROIs based on the local maxima of the group-level vectorlength-PAC averaged across frequencies in left/right sensorimotor (MNI: -44.4 -30.2 58.9 / 39.7 -20.0 61.0), visual (-19.1 -99.7 2.1 / 19.1 -99.6 1.7), parietal (-11.1 -81.3 45.3 / 11.1 -81.6 45.4) and superior temporal cortex (-62.5 -43.9 15.0 / 63.0 -8.6 15.0). We averaged coupling measures across hemispheres.

2.2.13 Statistical analysis of coupling measures

We employed a time-shifting surrogate procedure to assess the statistical significance of cross-frequency coupling. We generated 100 random circular time-shifts drawn from a uniform distribution from 0 to the length of the data. The same time-shift was applied for all sources and frequency combinations. For the vectorlength measure, the amplitude time-series of each subject was shifted circularly relative to the phase time-series and vectorlength-PAC was computed for each of the 100 shifts. For bicoherence, we shifted the time-series of f_3 relative to f_1 and f_2. For AAC and PPC, we shifted the timeseries of f_2 relative to f_1. AAC values and corresponding surrogate values were Fisher-z-transformed. For each measured coupling measure, a z-score was computed relative to the corresponding 100 surrogate values. To determine significant cross-frequency coupling while controlling for multiple comparisons, we employed a cluster permutation statistic across cross-frequency space or cortical space. For bicoherence and PPC statistics, cross-frequency spectra were smoothed with a 5-by-5 frequency-bin sized Hanning window. Clusters across cortical and cross-frequency space were defined based on the t-statistic of cross-frequency measures across subjects with a cluster threshold of $p < 0.01$. Clusters were then defined under the null-hypothesis by random sign flip across subjects before computing the t-statistic (1000 repeats). Cluster significance was defined as the probability to obtain a maximum cluster of at least this size across the null-hypothesis permutations with $p < 0.05$.

2.2.14 Analysis of the influence of artifacts

To study the potential influence of residual artifacts on the cross-frequency coupling results, we compared the spectral and spatial PAC patterns of artifactual signals defined during data preprocessing to the results of the cleaned data (Hipp and Siegel, 2013). To this end, we back-projected only the artifactual ICs to the sensors, beamformed these artifactual signals, and computed vectorlength-PAC and bicoherence on the source-localized artifacts. Finally, we compared the patterns of the artifactual signals with the patterns of

the cleaned signal. As residual heart-artifacts tend to be project to the brain center, we restricted this analysis to muscle- and eye-related artifacts.

2.2.15 Simulated signals with harmonic and non-harmonic PAC

We computed bicoherence, AAC and PPC of simulated signals with either higher harmonics or non-harmonic phase-amplitude coupling. These simulations illustrate typical cross-frequency coupling patterns expected for different signal types and cross-frequency measures.

In one of the non-harmonic PAC signals, the carrier frequency (f_c) and modulation side-peaks were distinct from the modulating frequency (f_m). To this end, we simulated coupling between f_m=10 Hz and f_c=40 Hz (resulting in side-peaks at 30 Hz and 50 Hz); once with 10-times smaller amplitude for f_c than f_m and once with 25-times smaller amplitude for f_c than f_m. Additionally, we simulated the special case of PAC, where the lower side-peak of the amplitude modulation (f_{c-m}) coincides with the modulating frequency (f_m=10 Hz and f_c=20 Hz, resulting in side-peaks at 10 Hz and 30 Hz, and with 4 times smaller amplitude for f_c than f_m).

For obtaining the raw signals at f_m and f_c ($x_{f_m}(t)$ and $x_{f_c}(t)$, respectively), we took 6 minutes of white noise and, at each time point, applied a Hanning window, calculated the FFT, extracted the frequency bin of interest, and applied the inverse Fourier transform. For each frequency, a Hanning window with a defined spectral width (full width at half maximum, FWHM) was used (FWHM = 1.5 Hz for f_m, and FWHM = 3 Hz and 2 Hz for f_c, for the two different signals, respectively). Then, non-harmonic PAC signals were generated by amplitude modulation of x_{f_c} according to the phase of x_{f_m} as follows:

$$x_{PAC}(t) = x_{f_m}(t) + \left(1 + 0.99 \cdot \cos\left(\Phi_{f_m}(t)\right)\right) \cdot x_{f_c}(t) + n(t)$$

$\Phi_{f_m}(t)$ is the phase of x_{f_m}, extracted from the above mentioned time-Fourier analysis. $n(t)$ is $1/f^2$-noise.

For the two simulated harmonic-PAC signals, we obtained the base component at 10 Hz ($x_{f_{10}}(t)$) using the procedure explained above for f_c, and added it up with 4 higher harmonics and $1/f^2$-noise ($n(t)$). Higher harmonics of $x_{f_{10}}$ were generated as:

$$x_{n \cdot f_{10}}(t) = a_n \cdot \left| F\left(x_{f_{10}}(t)\right) \right| \cdot \cos\left(\Phi_{f_{10}}(t) \cdot n + \vartheta_n\right)$$

Here, $\left| F\left(x_{f_{10}}(t)\right) \right|$ and $\Phi_{f_{10}}(t)$ are the instantaneous amplitude- and phase-time series of $x_{f_{10}}$, respectively, and n is the integer multiplier ($n \in \{2,3,4,5\}$). The relative amplitude and phase of the higher harmonics relative to the base component were controlled by the factors a_n and ϑ_n, respectively. In one simulation we used a_2 =0.25, a_3 =0.06, a_4 =0.025, a_5 =0.05, ϑ_2 =pi/2, ϑ_3=pi/4, ϑ_4=3/2*pi, and ϑ_5=2*pi. In the second simulation we used a_2=0.05, a_3=0.015, ϑ_2=pi/2 and ϑ_3=pi/4.

For all simulated signals, we applied the same processing as described for the estimated source-level data with a sampling rate of 4000 Hz excluding the line-noise filters. We calculated vectorlength, bicoherence, cross-frequency AAC and PPC as well as a time-average log-power spectrum.

2.2.16 Peak localization

To localize peaks in the frequency-frequency space for bicoherence, AAC, and PPC, we averaged the cross-frequency values across f_2 frequencies below 70 Hz. Then, we identified the f_1 with the maximum averaged cross-frequency measure (in the range 5 to 14 Hz for single subjects, 7.5 to 14 Hz for the average across subjects, and 0.1 to 2.5 Hz for the delta-f_1 peaks). Finally, we identified the corresponding f_2 frequency maxima for each maximum f_1.

2.2.17 Single-subject harmonic peaks in bicoherence

After observing harmonic peaks of theta/alpha PAC averaged across subjects, we tested for such a harmonic pattern across subjects. Specifically, we tested if f_2 frequencies of bicoherence peaks were at integer multiples of corresponding f_1 frequencies.

For localizing bicoherence peaks, we first smoothed the Z-scored bicoherence cross-frequency spectra by convolution with a 3x3 Hanning window. To more precisely detect peaks close to the $f_1 = f_2$ diagonal of the bicoherence cross-frequency spectrum, we extended the lower range of f_2-frequencies to f_1-3 Hz, but not lower than 0.5 Hz. Then, we created individual masks of single-subject significance by converting the Z-scores to p-values, false-discovery-rate correcting the p-values for multiple comparisons (Benjamini and Hochberg, 1995), and creating masks at the alpha level of 0.05. Next, we spline-interpolated both, the Z-scored cross-frequency spectra and masks, to 0.1 Hz resolution. Finally, we identified peaks of significant bicoherence as detailed above.

If bicoherence peaks reflected harmonics of an oscillator at the corresponding f_1 frequency, they should fit the following regression model:

$$\hat{f}_{2,peak}(n,\ subject,\ ROI) = f_{1,peak}(subject,\ ROI) \cdot n + error.$$

Here, n refers to the peak number. To avoid mislabeling of harmonic peaks, e.g. when a lower peak was not detectable, we set n to match the closest harmonic. In total, up to 6% of peaks per ROI were relabeled. For two peaks falling closest to the same harmonic, we omitted the peak associated with the weaker bicoherence Z-score. To rule out any bias due to peak relabeling, we tested the model fit against a permutation statistic that also entailed peak relabeling. For each ROI, we took peak positions of all subjects and 1000 times randomly reassigned f_2 and f_1 values across subjects, with the restriction that the same number of peaks had to fall within the 1st, 2nd, etc. peak groups as observed in the original data. For each of the 1000 surrogates, as well as for the original data, we computed the coefficient of determination (R^2) as a measure of model fit for each regression model (one for each nth harmonic at each ROI). Finally, we obtained p-values by comparing the original R^2 against the surrogates.

2.2.18 Simulating the bicoherence leakage pattern

In order to identify conspicuous caveats in the bicoherence analysis, such as leakage into remote frequency ranges, we simulated a 10-minute long signal (1000 Hz sampling rate) with higher harmonics that resembled the motor mu-rhythm with little noise and computed its bicoherence the same way as we did for a source reconstructed signal. To construct this signal, we took the same steps as explained above, with the only difference that the base component was reconstructed as $x_{f_{10}}(t) = 1 \cdot \cos(\varphi_{10}(t))$. The applied Hanning window was 4-s long, and the final signal was constructed using the following parameters: a_2=0.35, a_3=0.2, a_4=0.05, ϑ_2=pi, ϑ_3=0, and ϑ_4=pi.

2.2.19 Bicoherence leakage pattern

To test the observation that some of the bicoherence peaks with delta-f_1 reflect the leakage pattern of noisy harmonic signals of the alpha range, we made use of the predictable location of the leakage pattern. We constructed regression models to predict peak positions and tested the model fit of the data against a permutation statistic. Specifically, we applied the following regression model:

$$\hat{f}_{2,delta\ peak}(n, subj, ROI) = n \cdot f_{1,alpha\ peak}(subj, ROI) - f_{1,delta\ peak}(subj, ROI) + error$$

Here, for each subject and ROI, $f_{1,delta\ peak}$ represents delta range f_1 of the peaks, $\hat{f}_{2,delta\ peak}(n, subj, ROI)$ represents the n-th predicted f_2 peak corresponding to $f_{1,delta\ peak}$, and $f_{1,alpha\ peak}$ represents the alpha-range f_1-frequency that corresponds to the bicoherence peaks in that range. For each subject and ROI, $f_{1,alpha\ peak}$ was estimated as described above.

To locate ($f_{1,delta\ peak}$, $f_{2,delta\ peak}$) pairs more precisely, we used the z-scored bicoherence estimates with step size of 0.1 Hz for f_1 frequencies and 0.5 Hz for f_2 frequencies. Next, we interpolated the cross-frequency spectra along their f_2 axis to steps of 0.1 Hz, and smoothed the results by convolving

with a 3x3 Hanning kernel. Then, we localized the peaks at delta-range f_1 frequencies.

2.2.20 Analysis software

All analyses were performed in MATLAB (MathWorks Inc., Natick, USA) using the Fieldtrip toolbox (Oostenveld et al., 2011) and custom software.

2.3 Results[4]

2.3.1 Spectral structure of phase-amplitude coupling

We estimated vectorlength-PAC (Canolty et al., 2006) between a wide range of frequency pairs for 457 cortical sources in 89 subjects of the Human Connectome Project (HCP) resting-state MEG dataset (Fig. 1A). Averaged across the entire cortex, we observed significant coupling peaks in three different frequency ranges (Fig. 1A, top): between gamma phase frequencies and high gamma amplitude frequencies peaking at [f_φ, f_A] = [76.1 Hz, 152.2 Hz], between alpha phase frequencies and beta amplitude frequencies peaking at [f_φ, f_A] = [11.3 Hz, 22.6 Hz], and weak but significant between delta phase-frequencies and amplitude frequencies around 16 Hz. In the cortical space and averaged over all frequency pairs (Fig. 1A, bottom), the vectorlength measure peaked primarily in bilateral sensorimotor regions, with distinct peaks also in temporal, occipital and parietal areas. Do these patterns reflect true neuronal interactions between distinct oscillatory processes? To answer this, we first tested if these patterns were related to non-neuronal signals, i.e. muscle- or eye-movement artifacts.

[4] This section, including all subsections and figures, corresponds precisely to the corresponding section with the same title in Giehl et al., (2021). See also footnote 1 on page 19.

2.3.2 Phase-amplitude coupling reflects residual muscle- and eye-related artifacts

Despite using ICA-based artifact cleaning and beamforming, the data may well contain residual artifacts. To investigate the potential influence of such residual artifacts, we computed vectorlength-PAC of MEG signals that mainly contained artifacts (Fig. 1B and 1C, Materials and Methods). If results reflected residual artifacts, we should observe similar patterns for artifact signals. Indeed, vectorlength-PAC of muscle artifacts (Fig. 1B) showed a prominent peak that well matched the high frequency peak in the cleaned data. The cortical distribution of vectorlength-PAC for muscle artifacts peaked in inferior temporal and frontal regions, the latter reminiscent of a saccadic spike artifact (Carl et al., 2012) (Fig. 1B). This cortical distribution was significantly correlated with the cortical distribution of PAC for the cleaned signal in the corresponding frequency range [f_φ, f_A] = [45-76 Hz, 128-256 Hz] (Fig. 1A, small inset) (r^2 = 0.45, $p<0.001$). Together, these results suggested that high frequency PAC likely reflected muscle artifacts rather than neuronal coupling.

We repeated the same analysis for a potential contamination by residual eye-movement artifacts (Fig. 1C). Eye-movement artifacts showed low-frequency vectorlength-PAC for phase and amplitude frequencies below approximately 3 and 8 Hz, respectively. This only partially matched the weak but significant low frequency PAC for the cleaned data, which peaked for amplitude frequencies around 16 Hz reaching up to 64 Hz. Thus, low-frequency PAC could only be partially explained by residual eye-movement artifacts.

Next, we tested if these findings generalized to PAC estimation using bicoherence, which assess non-linear interactions between two frequencies by quantifying the phase consistency between these frequencies and their sum (Shahbazi Avarvand et al. 2018). Indeed, for high frequencies, we found a similar distribution of significant bicoherence for the cleaned data (Fig. 1D) and muscle artifacts (Fig. 1E). The cortical distribution of bicoherence of the cleaned data for this frequency range (Fig. 1D, left small inset) was significantly correlated with the cortical distribution of bicoherence for muscle-artifacts (Fig. 1E, left, r^2=0.25, $p<0.001$) as well as with the cortical distribution of

vectorlength-PAC of the cleaned data (Fig. 1A, small inset, r^2=0.92, p<0.001) and muscle-artifacts (Fig. 1B, r^2=0.46, p<0.001). This further suggested that residual muscle artifacts generated spurious high-frequency PAC in temporal, orbito-frontal and lateral inferior regions.

For eye movements artifacts, bicoherence could again not entirely explain PAC at low frequencies. Bicoherence of eye artifacts peaked at f_1 frequencies from 1 to 2.5 Hz and f_2 frequencies up to 20 Hz and above 30 Hz (Fig. 1F). In contrast, the cleaned data showed significant bicoherence over a broader low-frequency range (Fig. 1D). Moreover, the cortical distributions of bicoherence of eye-artifacts and the cleaned-data was only weakly correlated for low frequencies (r^2=0.15, p<0.01).

In sum, both measures, vectorlength-PAC and bicoherence, consistently identified significant PAC that likely reflects residual muscle- and eye movement artifacts in high and low frequency ranges, respectively.

2.3.3 Phase-amplitude coupling in the alpha frequency-range

Vector-length PAC and bicoherence showed prominent effects in the alpha-frequency range that could not be attributed to muscle or eye movement artifacts. Do these effects reflect true neuronal interactions between distinct oscillations?

For vectorlength-PAC, the coupling of the alpha phase-frequency peaked at the double-phase-frequency diagonal ($f_A = 2f_\varphi$), i.e. at the first higher harmonic of the phase frequency (maximum at [f_φ , f_A] = [11.3, 22.6]). Bicoherence showed several peaks at f_1= 10.5 Hz and f_2 of 11 Hz, 21 Hz, 30.5 Hz and 44 Hz, which are close to harmonics of f_1. Thus, we hypothesized that these peaks may merely reflect harmonics of alpha oscillations, rather than true neuronal interactions. To address this question, we next focused on why PAC measures are sensitive to rhythmic signals with higher harmonics and how harmonics and non-harmonic PAC could be dissociated.

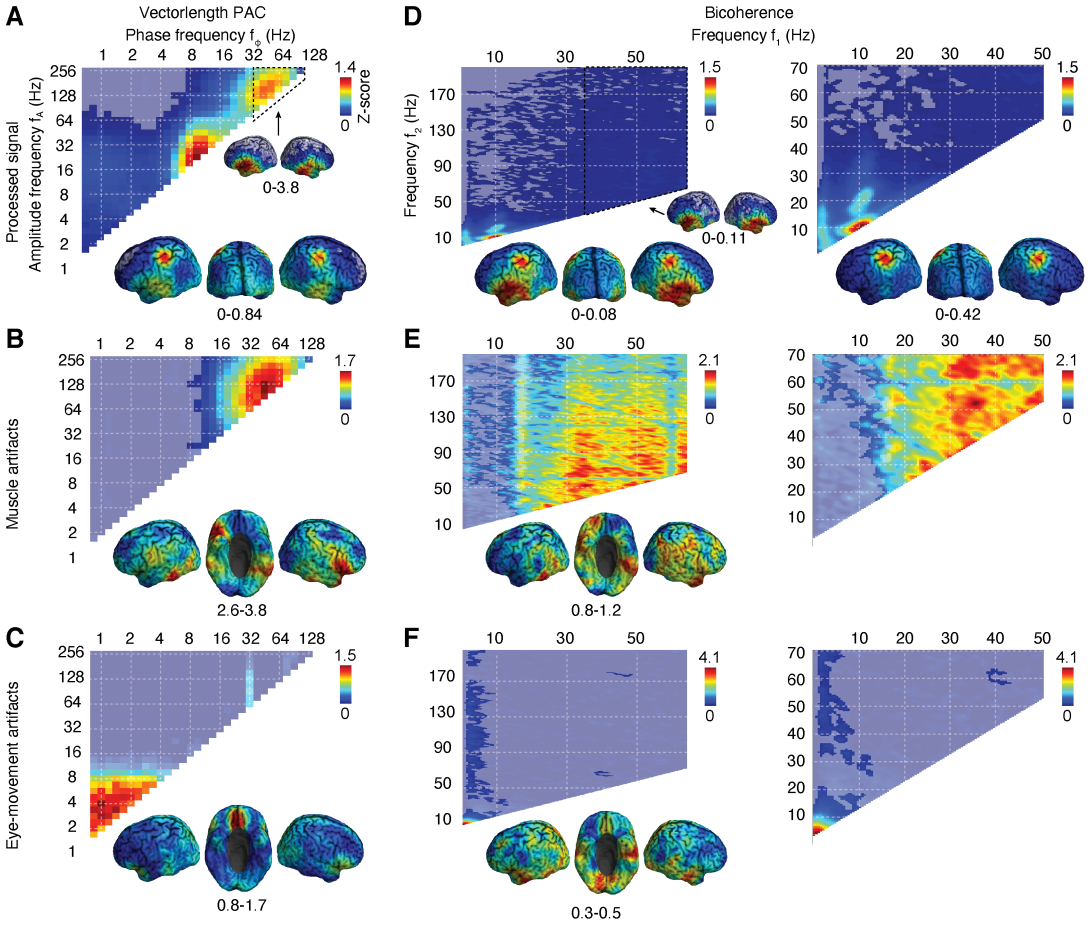

Figure 1. Vectorlength-PAC and bicoherence.

(A) Vectorlength-PAC averaged across the cortex (top), and its cortical distribution, averaged either across all (bottom) or high gamma frequencies (inset). **(B)** Vectorlength-PAC of rejected muscle artifacts (independent components) averaged across the cortex (top) and all significant frequency combinations (bottom). **(C)** Vectorlength-PAC of rejected eye-related artifacts (independent components) averaged across the cortex (top) and all significant frequency combinations (bottom). **(D)** Bicoherence averaged across the cortex for a large frequency range (left) and zoomed-in lower frequency range (right). Cortical distributions of bicoherence averaged for the corresponding frequency ranges are shown below. The inset shows the cortical distribution of bicoherence for a high-frequency range often associated with muscle activity. **(E)** Bicoherence of rejected muscle artifacts averaged across the cortex (top) and for significant frequency combinations (bottom) **(F)** Bicoherence of rejected eye-related artifacts averaged across the cortex (top) and for significant frequency combinations (bottom). All coupling measures are z-scores relative to surrogate statistics generated by circular data shuffling. Opacity indicates statistical significance ($p<0.05$; corrected; permutation statistic).

2.3.3.1 Harmonic and non-harmonic phase-amplitude coupling

Figure 2 compares non-harmonic PAC, i.e. phase-amplitude coupling between two independent oscillations (Fig. 2 left, 10 Hz to 40 Hz coupling), with

harmonic PAC, i.e. a rhythmic non-sinusoidal signal with higher harmonics (Fig. 2 right, 10 Hz base frequency with three harmonics).

Importantly, both bicoherence and vectorlength-PAC do not only yield cross-frequency phase-amplitude coupling for non-harmonic PAC, but also for harmonic PAC (Kovach et al., 2018; Shahbazi Avarvand et al., 2018). How can this be intuitively understood?

For vectorlength-PAC, the spectral bandwidth of higher frequency components needs to be wide enough (at least twice the low frequency) to capture their potential amplitude modulation (Aru et al., 2015; Dvorak and Fenton, 2014, compare high frequencies extracted with narrow and wide filters in Fig. 2). For harmonic signals, this implies that multiple harmonics of the base frequency can be captured, which results in an apparent amplitude modulation of high frequencies (Fig. 2B). This modulation is phase-consistent with the base frequency, which yields significant vectorlength-PAC in absence of an independent high frequency oscillator.

Bicoherence does not necessitate wide filters but is also sensitive to both, harmonic and non-harmonic PAC (Avarvand et al. 2018). This is, because for harmonic PAC (Fig. 2, right), there is always a stable phase relationship between the base frequency and its higher harmonics. Thus, bicoherence measures cross-frequency coupling for all frequency pairs, where each frequency and their sum coincide with the base frequency or a higher harmonic.

2.3.3.2 Dissociating harmonic and non-harmonic phase-amplitude coupling

How can we distinguish harmonic and non-harmonic PAC? Harmonics are only present at integer multiples of the base frequency. Thus, a first test is whether the frequencies at which PAC is observed could reflect harmonics of a base frequency. Bicoherence is particularly suited for this test, because it enables higher spectral resolution than vectorlength-PAC. However, if the observed PAC frequencies match a harmonic pattern, this may still reflect non-harmonic PAC at these frequencies (e.g. Fig. 2, left). Thus, for harmonic PAC frequency patterns, further tests are required.

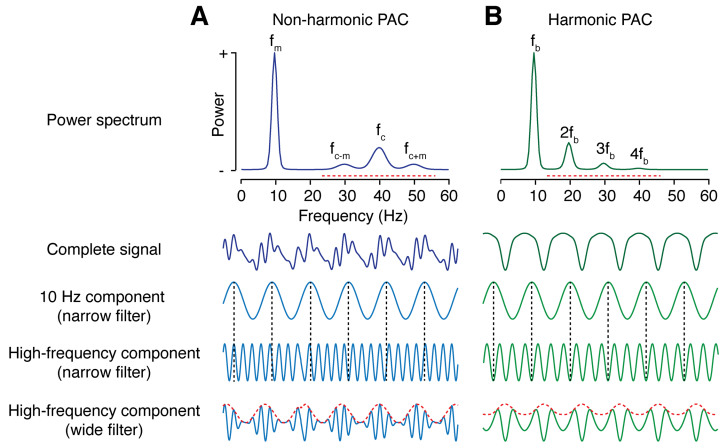

Figure 2. Non-harmonic and harmonic PAC.

(A) Simulated signals with non-harmonic PAC between a modulating frequency $\boldsymbol{f_m}$ = 10 Hz and a carrier frequency $\boldsymbol{f_c}$ = 40 Hz (left) **(B)** Simulated signal with harmonic PAC due to a non-sinusoidal signal with base frequency $\boldsymbol{f_b}$ = 10 Hz and three higher harmonics. First row: Power spectra. Red lines indicate the high-frequency bandwidth required for vectorlength-PAC. Second row: complete time-domain signals. Third row: low frequency component extracted with a narrow bandpass filter at 10 Hz. Fourth row: high frequency component of interest extracted with a narrow bandpass filter at $\boldsymbol{f_c}$ and $\boldsymbol{3f_b}$ for non-harmonic and harmonic PAC, respectively. The narrow filter prevents amplitude modulation (see subsection 3.3.1. for further explanation). For non-harmonic PAC, there is no stable phase relationship between the low and high frequency components. In contrast, for harmonic PAC, there is a stable phase relationship. Fifth row: high frequency components extracted with a wide filter (dashed red lines). Both signal types show an amplitude modulation of high-frequency components that is coherent with the 10 Hz component.

To investigate such potential tests, we simulated signals that contained either harmonic or non-harmonic PAC between 10 Hz and some of its integer multiple frequencies. For each signal, we computed not only the vectorlength measure and bicoherence to assess PAC, but also cross-frequency amplitude-amplitude coupling (AAC) and cross-frequency phase-phase coupling (PPC) (Fig. 3).

Vectorlength-PAC shows similar coupling patterns for harmonic PAC (Fig. 3A) and non-harmonic PAC (Fig. 3B). Harmonic-PAC shows two overlapping peaks at harmonically related frequencies, i.e. at $[f_\varphi, f_A] = [f_b, 2f_b]$ and $[2f_b, 3f_b]$. Non-harmonic PAC also shows two peaks. A first large peak is between the modulating and carrier frequencies, i.e. around $[f_\varphi, f_A] = [f_m, f_c]$. A second peak, which appears to be a byproduct of the large bandwidth of the spectral filters, is positioned at about $[f_\varphi, f_A] = [f_{c-m}, f_{c+m}]$. However, due to the low

spectral resolution of vectorlength-PAC, it is difficult to clearly dissociate the generated patterns.

The high spectral resolution of bicoherence allows for better resolving these patterns. For both, harmonic (Fig. 3A) and non-harmonic (Fig. 3B) PAC, bicoherence shows distinct peaks at all [f_1, f_2] combinations, at which f_1, f_2, and $f_3 = f_1 + f_2$ coincide with peaks in the power spectrum. For harmonic-PAC (Fig. 3A), power peaks at the base frequency and higher harmonics, which results in several corresponding bicoherence peaks. For non-harmonic PAC (Fig. 3B), power shows four peaks at the modulating frequency f_m, carrier frequency f_c and side-peaks $f_{m+/-c}$. This leads to exactly two bicoherence peaks at frequencies [f_1, f_2] = [f_m, f_c] and [f_1, f_2] = [f_m, f_{c-m}] (Fig. 3B) (Hyafil, 2015). Thus, bicoherence with more than two harmonic peaks cannot only be caused by non-harmonic PAC, but implies harmonic PAC.

Amplitude-amplitude and phase-phase coupling further dissociate harmonic and non-harmonic PAC and can be conveniently computed with the same spectral resolution as bicoherence (Fig. 3). By definition, harmonics imply AAC and PPC between the base frequency and any harmonics. AAC and PPC measures of harmonic-PAC signals well reflect these couplings (Fig. 3A). In contrast, non-harmonic PAC does not imply AAC or PPC between the modulating frequency and the carrier frequency or its side-peaks. Thus, for non-harmonic PAC (Fig. 3B), there is no AAC or PPC between the modulating frequency and any of the power peaks at higher frequencies. This provides a dissociating feature between harmonic and non-harmonic PAC.

One concern may be that the above features may not be detectable at low SNR of higher spectral peaks. To investigate this, we repeated our simulations with higher spectral peaks that were close to the noise level (Fig. 3C and D). For both harmonic (Fig. 3C) and non-harmonic PAC (Fig. 3D), cross frequency coupling measures showed patterns generally consistent with the high SNR case, although some peaks merged to one wider peak due to the lower SNR (bicoherence in Fig. 3D). Importantly, for harmonic-PAC (Fig. 3C), both AAC and PPC showed peaks at frequency combinations with $f_1 = f_b$, while such peaks were absent for non-harmonic PAC. Therefore, even at low SNR,

bicoherence, AAC, and PPC allow to dissociate harmonic and non-harmonic-PAC.

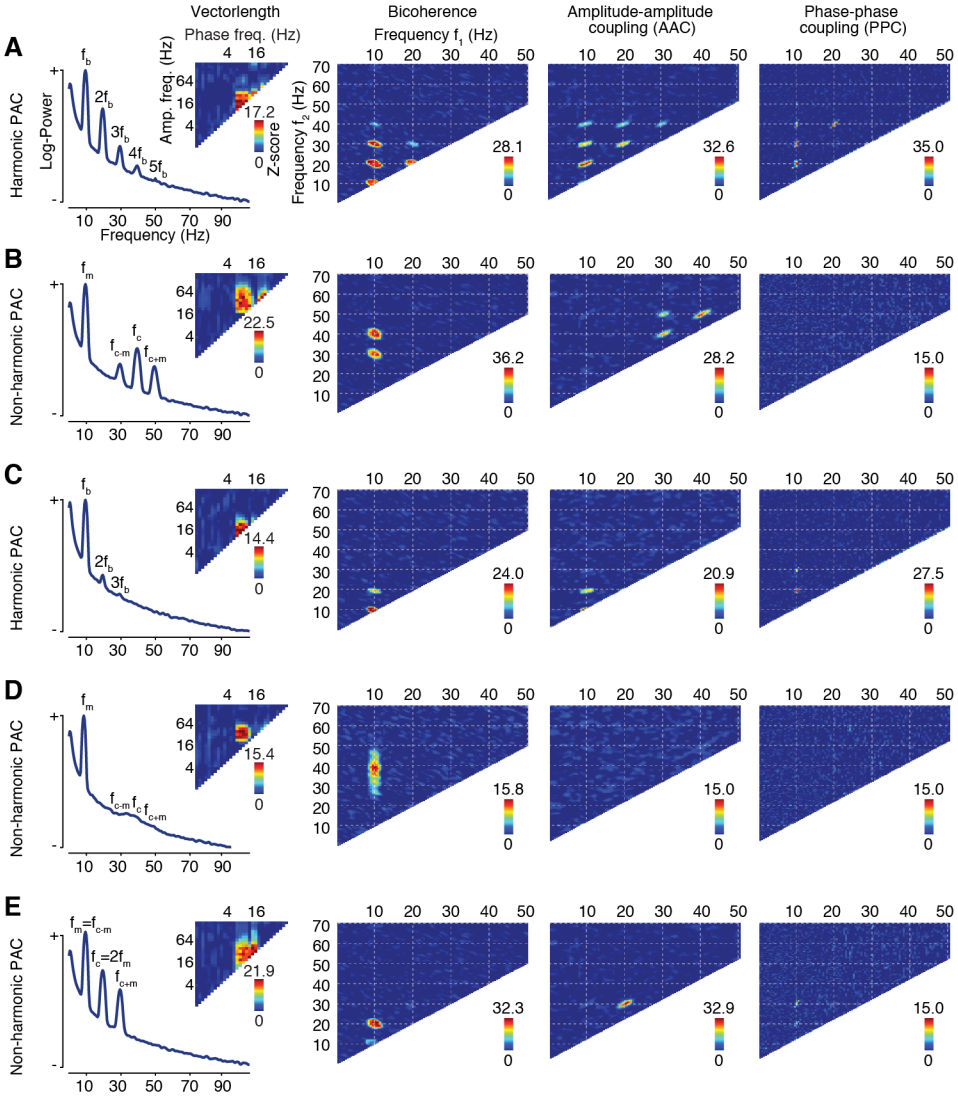

Figure 3. Dissociating harmonic and non-harmonic PAC.

Power spectra, cross-frequency vectorlength, bicoherence, amplitude-amplitude coupling (AAC) and phase-phase coupling (PPC) for three different simulated signals with harmonic or non-harmonic PAC. All signals contained oscillatory components and uncorrelated $1/f^2$-noise. (**A**) Power and cross-frequency measures for a 10 Hz signal with four higher harmonics. (**B**) Non-harmonic PAC between 10 and 40 Hz. (**C**) Power and cross-frequency measures for a 10 Hz signal with two higher harmonics of lower SNR. (**D**) Non-harmonic PAC between 10 Hz and lower SNR 40 Hz component (**E**) Special case of non-harmonic PAC, between 10 Hz and 20 Hz. In this case, the lower side-peak of the modulated frequency f_{c-m} coincides with the modulating frequency f_m. All coupling measures are z-scores relative to surrogate statistics generated by circular data shuffling.

Finally, there is one special case of non-harmonic PAC, which is more ambiguous. This is when the carrier frequency is twice the modulating frequency (Fig. 3E). In this special case, the lower side-peak of the amplitude modulation coincides with the modulating frequency itself (10 Hz in Figure 3E). This leads to vectorlength, bicoherence and PPC patterns similar to patterns for a non-sinusoidal oscillator with only two higher harmonics. However, in this case, the relative strength of bicoherence and AAC peaks allows for dissociating harmonic and non-harmonic PAC, because the signal at the modulating frequency mixes with the lower-frequency side peak of the carrier frequency. For bicoherence, this leads to weaker coupling at [f_1, f_2] = [f_m, f_m] as compared to [f_1, f_2] = [f_m, f_c]. This is in contrast to harmonic PAC, which shows the opposite relative strength due to the lower power of harmonics as compared to the base frequency. Along the same line, for AAC coupling at [f_1, f_2] = [f_m, f_c] is absent or weaker than coupling at [f_1, f_2] = [f_c, $f_c + f_m$], which again is opposite to harmonic-PAC.

In sum, several features allow to assess if PAC is harmonic or non-harmonic in nature. A first useful heuristic is to test if the observed frequencies are multiples. Bicoherence is well suited for this assessment due to its high spectral resolution. If the observed frequencies are clearly not multiples, non-harmonic PAC is the cause. Otherwise, if the observed frequencies are multiples, bicoherence, AAC and PPC together are decisive. Bicoherence with more than two harmonic peaks implies harmonic PAC. Furthermore, bicoherence, AAC, and PPC between the base frequency and its harmonics imply harmonic PAC, in particular if bicoherence is strongest for identical f_1 and f_2 at the base-frequency. We next applied this approach to test if the observed PAC in the alpha range (Fig. 1A and 1D) reflected harmonic or non-harmonic PAC.

2.3.3.3 Alpha phase-amplitude coupling reflects harmonics

As indicated above, average vectorlength PAC peaked between alpha phase- and beta amplitude frequencies (Fig. 1A and 4A). Average bicoherence peaked between alpha-frequencies f_1 and harmonic frequencies f_2 (1D and 4A). This was also the case for every individual cortical region with prominent PAC, i.e. sensorimotor, parietal, occipital and temporal areas with an apparent

variability of the fundamental alpha frequency between regions (Fig. 4B-E), as well as for the average across the remaining cortical areas (Fig. 4F). Therefore, we next computed AAC and PPC across the entire cortex and for the mentioned regions to assess the nature of alpha PAC (Fig. 4, middle and right column).

The average across the cortex (Fig. 4A), all four regions of interest (Fig. 4B-E) and the average across the remaining cortical areas (Fig. 4F) showed prominent AAC and PPC with strongest peaks at $[f_1, f_2]$ = [10, 20] Hz and several effects at higher harmonics. Harmonic coupling was particularly strong for sensorimotor cortex, which showed prominent amplitude and phase coupling even between the second (20 Hz) and fourth (40 Hz) harmonic. We concluded that the observed PAC reflected harmonic-PAC, rather than non-harmonic PAC of independent oscillations.

If bicoherence, AAC and PPC all reflect the same harmonic PAC, their cortical distribution should be correlated. This is what we found. Averaged across all frequency pairs, the cortical patterns of bicoherence, AAC and PPC were strongly correlated (bicoherence vs. AAC: $r = 0.89$, $p < 0.0001$; bicoherence vs. PPC: $r = 0.93$, $p < 0.0001$; AAC vs. PPC: $r = 0.88$, $p < 0.0001$; Pearson correlation; Fig. 4A).

Single subject data further supported the conclusion of harmonic-PAC. In particular, while it was difficult to identify clear harmonic peaks in the averaged power spectra (Fig. 4A-F), such harmonic peaks could well be identified in the power spectrum of many individual subjects along with corresponding cross-frequency coupling peaks (one example is shown in Fig. 4G). This is because the single subject results are not affected by inter-subject variance of the alpha peak-frequency, and therefore more closely resemble the simulation of harmonic coupling (compare Fig. 3A and Fig. 4G).

In sum, converging evidence suggested that PAC for low frequencies in alpha/beta range was harmonic in nature, and, thus, most likely reflected rhythmic signals with a non-sinusoidal waveform shape.

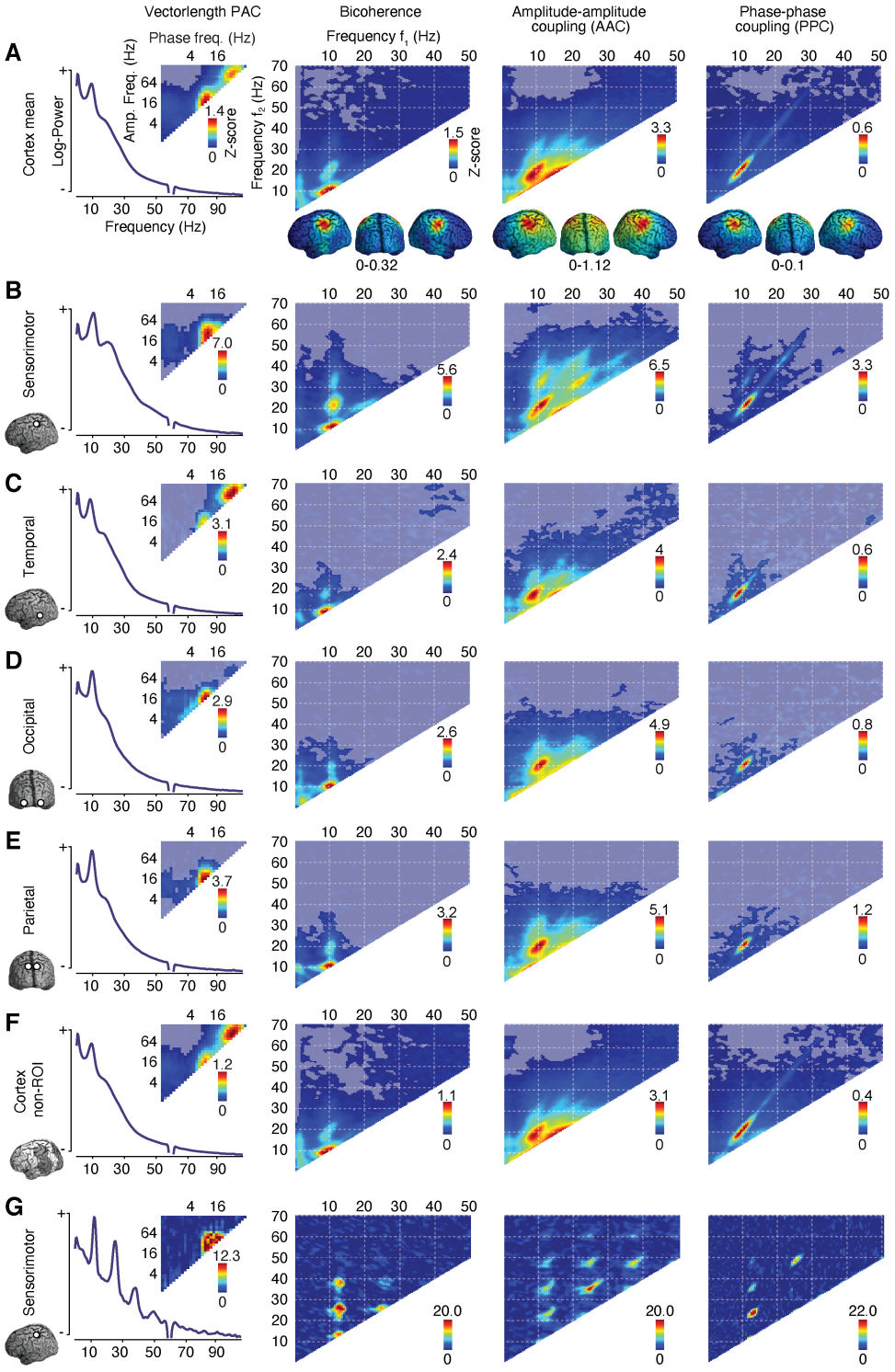

Figure 4. Cortical cross-frequency coupling.

(**A**) Left panel: Log-power spectrum and vectorlength PAC averaged across the cortex. Remaining panels: Spectral and cortical distribution of bicoherence, cross-frequency amplitude-amplitude coupling and cross-frequency phase-phase coupling averaged across the cortex and across all frequency combinations, respectively. (**B-E**) Left panel: Log-power spectrum and vectorlength PAC for four different cortical ROIs. Remaining panels: Cross-frequency coupling measures for four different cortical ROIs. (**F**) As (B-E) for all remaining cortical sources, after excluding the four ROIs and their neighbouring sources.

(**G**) As (B) for an exemplary single-subject. All coupling measures are z-scores relative to surrogate statistics generated by circular data shuffling. Opacity (not applied in G) indicates statistical significance (p<0.05; corrected; permutation statistic).

2.3.3.4 Harmonic phase-amplitude coupling reflects individual alpha rhythms

In a control analysis, we next exploited the variability of the alpha-rhythm across subjects to further ascertain the harmonic nature of alpha PAC. For harmonic-PAC, the observed bicoherence peaks should scale with the variable alpha frequency across subjects. Thus, for each subject, we extracted all [f_1, f_2] peak frequencies for f_1 in the alpha band and tested if these peaks were integer multiples of the individual alpha frequency (i.e. $f_2 = n\, f_1$, for $n = 1,2,3$).

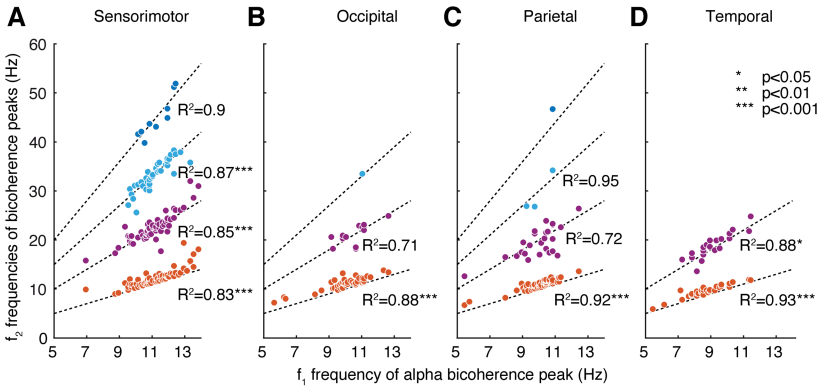

Figure 5. Harmonic PAC at individual alpha frequencies.

(**A**) Bicoherence peak positions [f_1, f_2] with f_1 frequencies in the alpha range across all individual subjects for all four ROIs. Dashed lines indicate harmonic models along with R^2 values of model fits and statistical significances. [sic]

For all regions, peak positions were compatible with the harmonic model (Fig. 5). The model fit of the lowest bicoherence peak to the first harmonic at $f_2 = f_1$, which implies coupling between the base frequency and the second harmonic, was significant for all ROIs (motor ROI: r^2 = 0.83, p<0.001; visual ROI: r^2 =0.88, p<0.001; parietal ROI: r^2 =0.92, p<0.001; temporal ROI: r^2 =0.93, p<0.001). The model fit for the second harmonic ($f_2 = 2f_1$) was significant for motor and temporal cortex (motor ROI: r^2 = 0.85, p<0.001; temporal ROI: r^2 = 0.88, p<0.05). For the motor cortex, also the model fit for the third harmonic ($f_2 = 3f_1$) was significant (r^2 = 0.87, p<0.001). Thus, for all regions of interest, the

frequencies of bicoherence in individual subjects were well explained by alpha harmonics.

2.3.4 Replication in an independent dataset

We replicated the above findings in a second, independent dataset that was recorded with another MEG system at another research site (Fig. 6; Tübingen dataset). As for the HCP data, we found prominent vectorlength-PAC between alpha phase- and beta amplitude frequencies and prominent bicoherence peaks at alpha f_1 frequencies and at harmonic frequency combinations. Again, harmonic coupling was also present for AAC and PPC with decreasing coupling strengths for higher frequencies. We tested if the cortical distribution of PAC was similar between the two datasets. Indeed, the pattern of bicoherence, AAC and PPC was highly correlated between the two datasets (bicoherence r=0.85, $p < 0.0001$; AAC r = 0.85, $p < 0.0001$; PPC r = 0.77, $p < 0.0001$).

In sum, the results were highly consistent between the HCP and independent replication datasets. We concluded that, also for the replication dataset, PAC for low frequencies in the alpha range was harmonic in nature, and, thus, related to non-sinusoidal rhythmic signals rather than due to non-harmonic PAC between independent oscillators.

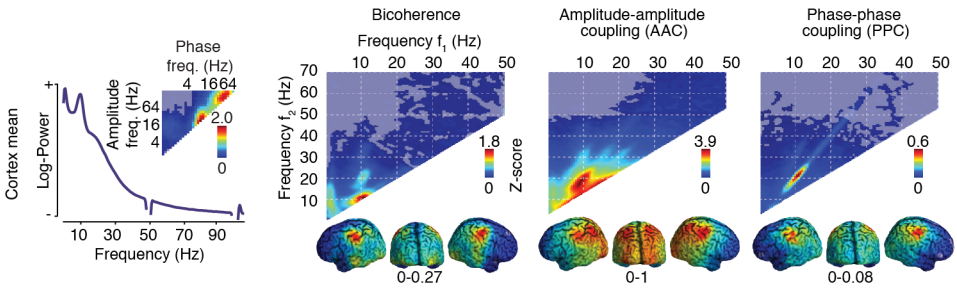

Figure 6. Replication of key results.

Left panel: Log-power spectrum and vectorlength-PAC averaged across the cortex. Remaining panels: Spectral and cortical distribution of bicoherence, cross-frequency amplitude-amplitude coupling and cross-frequency phase-phase coupling averaged across the cortex and across all frequency combinations, respectively, for the replication dataset. All coupling measures are z-scores relative to surrogate statistics generated by circular data shuffling. Opacity indicates statistical significance ($p<0.05$; corrected; permutation statistic).

2.3.5 Sub-alpha phase-amplitude coupling

Our initial vectorlength-PAC (Fig. 1A) and bicoherence analysis (Fig. 1D) revealed PAC at frequencies below 8 Hz that could not entirely be explained by eye-movement artifacts. In a final set of analyses, we investigated the nature of coupling in this sub-alpha frequency range.

The sensorimotor bicoherence of several subjects showed distinct peaks at sub-alpha f_1 frequencies that seemed to mirror the harmonic peaks at the individual f_1 alpha frequency (Fig. 7A). Thus, we hypothesized that these sub-alpha peaks might be caused by alpha-frequency harmonics. To investigate this, we analyzed low frequency bicoherence of a simulated 10 Hz signal with higher harmonics (Fig. 7B). Indeed, this revealed a characteristic "leakage pattern" at sub alpha frequencies with horizontal, vertical and anti-diagonal leakage lines that intersect at the harmonic 10 Hz peaks (f_2=n*10, f_1=n*10 and f_1+ f_2= n*10, respectively, for integer n). This specific pattern can be intuitively understood by the frequency combination used for bicoherence. Along horizontal, vertical or anti-diagonal lines, either the f_1, f_2 or f_3 frequency stays constant. Consequently, the leakage of bicoherence is falling off slower along these lines than in any other direction.

We next tested if such a leakage pattern was present in the MEG data. In each subject, we located up to three sub-alpha f_1 bicoherence peaks and tested if their position was in line with the predicted leakage pattern (Fig. 7C). Indeed, peak positions were significantly correlated with the predictions of the leakage model across subjects (first peaks: R^2=0.82, p <0.001; second peaks: R^2 =0.89, p<0.01, third peaks R^2 =0.89, p>0.05). This provided strong evidence that sub-alpha bicoherence peaks reflected spectral leakage of alpha oscillations with higher harmonic components. If this is correct, the cortical distribution of sub-alpha bicoherence should be correlated with the cortical distribution of alpha bicoherence. Indeed, we found a strong correlation of the cortical distribution of bicoherence in the leakage-related sub-alpha range ([f_1, f_2] = [0.5 to 4 Hz, 2.5 to 40 Hz]) and in the range of alpha harmonics ([f_1, f_2] = [7 to 14 Hz, 7 to 40 Hz] (r^2 =0.81, p<0.001, Fig. 7D).

Notably, the above spectral analyses were based on temporal windowing using a 1 s Hanning taper. We hypothesized that the peak position of the leaked sub-alpha bicoherence was related to the spectral cut-off of this temporal windowing near 1.5 Hz. To test this, we repeated the analyses based on 2 s and 4 s Hanning windows (Fig. 7E). As hypothesized, the peak of leaked sub-alpha bicoherence shifted towards lower frequencies for longer temporal windows. Thus, the employed windowing modulates the exact spectral profile of PAC that is leaked below the frequency of non-sinusoidal oscillations

3 From (harmonic) PAC to the wave shape of oscillations[5]

We systematically investigated cross-frequency PAC across the human brain using MEG. Consistent across two independent datasets, we observed cortically and spectrally wide-spread PAC. However, we found no evidence for PAC that could be unequivocally attributed to non-harmonic coupling between distinct neural oscillators. Instead, the observed PAC could well be explained by remaining eye- and muscle artifacts, and by alpha oscillations with a non-sinusoidal waveform shape.

3.1 Dissociating harmonic and non-harmonic PAC

Non-harmonic and harmonic PAC likely involve distinct underlying neuronal mechanisms. Therefore, it is necessary to carefully distinguish between these two cases in order to arrive at a correct interpretation of cross-frequency coupling results (Cole and Voytek, 2017).

Non-harmonic PAC is generally thought to reflect an interaction between two distinct oscillatory neuronal processes in which the phase of a slower rhythm modulates the amplitude of a faster rhythm (Hyafil et al., 2015). Accordingly, non-harmonic PAC has been suggested to coordinate the activity of cell-assemblies across different rhythmic processes, which may in turn also coordinate activity across different spatial distances (Hyafil et al., 2015; Jensen and Colgin, 2007; Lisman and Idiart, 1995; von Nicolai et al., 2014).

Concerning harmonic coupling, little is known about its physiological basis, which may indeed vary for different cases. Harmonic coupling may result from the non-sinusoidal waveform shape of rhythmic processes, which has been demonstrated for various rhythms with M/EEG, ECoG and LFPs (Bartz et al.,

[5] This chapter, up to and including section 3.4, corresponds precisely to the section with the title “Discussion”, and to the respective subsections with corresponding titles, in Giehl et al., (2021). See also footnote 1 on page 19.

2019; Buzsáki et al., 1985; Chacko et al., 2018; Cole et al., 2017; Cole and Voytek, 2017; Dellavale et al., 2020; Kuhlman, 1978; Vaz et al., 2017). Such non-sinusoidal waveform shapes might be caused by a single rhythmic circuit mechanism (Cole and Voytek, 2017; Meidahl et al., 2019; Sherman et al., 2016), or by simultaneous phase- and amplitude-coupling of distinct harmonically related oscillations.

Our results show that the combination of three different cross-frequency coupling measures (bicoherence, amplitude coupling and phase coupling) allows to reliably distinguish harmonic and non-harmonic PAC. This approach well complements other methods or heuristics that can be used to dissociate harmonic and non-harmonic PAC. E.g. cross-frequency coupling could be related to neuronal spiking, PAC could be related to power, or PAC could be investigated between areas with distinct low- and fast oscillations (Jensen et al., 2016).

Based on our approach, we characterized the nature of the observed cross-frequency interactions between alpha and higher frequencies. We identified harmonic-PAC as underlying the abundant and strong local PAC observed in this frequency range: i.e. alpha oscillations with apparently non-sinusoidal waveform shapes.

Our findings accord well with previous reports that linked phase-amplitude coupling to alpha harmonics. Barnett et al. (1971) observed harmonic bicoherence, strongest over occipital and central areas, in subjects with strong alpha activity. Lozano-Soldevilla (2016) reported harmonic bicoherence of alpha $\boldsymbol{f_1}$ frequencies in central and occipital MEG sensors. Following the increasing interest in cross-frequency interactions, the problem that PAC measures reflect harmonics has received growing attention (Aru et al., 2015; Chacko et al., 2018; Cole et al., 2017; Cole and Voytek, 2017; Gerber et al., 2016; Hyafil, 2015; Jensen et al., 2016; Kramer et al., 2008; Lozano-Soldevilla et al., 2016; Vaz et al., 2017; Velarde et al., 2019). Our approach builds on previous efforts that have used bicoherence to aid the identification and characterization of harmonic coupling (Bartz et al., 2019; Kramer et al., 2008;

Lozano-Soldevilla et al., 2016; Sheremet et al., 2019), and extends them by suggesting a pipeline to distinguish harmonic- and non-harmonic bicoherence.

It is worth mentioning that, although we cannot entirely exclude the presence of any weak and potentially masked non-harmonic PAC, it is clearly no prominent feature in resting-state MEG data. One remaining concern might be, that a potentially low signal to noise ratio of the recordings might have resulted in limited sensitivity for the estimation of phases and amplitudes, which in turn might have impeded the identification of non-harmonic PAC. However, a previous study that used the same dataset, similar source-reconstruction and spectral analysis identified robust cross-area within-frequency phase- and amplitude coupling (Siems and Siegel, 2020). Thus, the source-reconstructed data likely provided adequate signal to noise ratio for valid estimates of phases and amplitudes.

Here we focused on local PAC. Cross-area PAC (Chella et al., 2014; Nandi et al., 2019; Siebenhühner et al., 2020; van der Meij et al., 2012; von Nicolai et al., 2014) also needs to be carefully assessed with respect to harmonic signals. This is because local harmonics together with cross-area phase-coupling of the base-frequency may also result in measuring cross-area PAC without any underlying cross-area cross-frequency interaction between independent oscillations.

3.2 Physiological artifacts

Our results show that physiological artifacts such as eye-movements and muscle activity can cause cross-frequency coupling and need to be carefully distinguished from brain activity. We observed strongest muscle artifacts in high frequency ranges reaching down to the alpha range. Eye-movement artifacts were observed in the sub-alpha and sub-alpha to high-gamma range, which might be reflecting coupling between eye-muscle related high frequency activity and slow neural- or neuromuscular activity. Notably, we observed PAC due to these artifacts although subjects fixated continuously, the data was cleaned for artifacts and source-reconstruction using beamforming further

suppressed extracranial activity (Hipp and Siegel, 2013). This highlights the sensitivity of PAC measures to artifacts and the need to carefully exclude artifacts as causes of spurious PAC. This also includes other physiological artifacts such as heart-activity (Shahbazi Avarvand et al., 2018), which is typically projected to deeper sources.

3.3 Spectral leakage

Our results show that spectral leakage is an important caveat when assessing PAC. The simulation of a noisy non-sinusoidal alpha oscillation revealed a wide-spread pattern of spectral leakage of bicoherence between frequencies that were all linked to harmonics of alpha. We identified a matching leakage pattern in the MEG data suggesting that also sub-alpha PAC reflects leakage of harmonic alpha PAC. Critically, the leakage pattern was observed at lower frequencies than the base-frequency of the non-sinusoidal oscillator. Thus, non-sinusoidal signals can not only drive PAC at higher harmonics, but, due to spectral leakage, can also drive spurious PAC at lower frequencies than the base frequency at hand. This mechanism may be particularly problematic for muscle artifacts and may cause spurious PAC at very low frequencies typically not associated with muscle artifacts (compare Figs. 1E and 1F).

In this context, it should be noted that, while spectral leakage may be negligible for power, it may become particularly problematic for bicoherence and other cross-frequency measures. This is because, in contrast to power, these cross-frequency measures are sensitive to the preserved phase-consistencies between leaked signal components.

3.4 Spectral resolution

In sum, our results show that alpha harmonics, leakage and residual muscle activity can impact broad frequency ranges. Thus, investigating only a few pre-defined frequency bands may lead to misinterpretations of PAC results. In other words, a comprehensive characterization of cross-frequency coupling across a

broad frequency spectrum is required to unequivocally assess the nature of cross-frequency coupling. This in turn necessitates proper selection of spectral resolution.

Vectorlength-PAC requires a broad resolution (or wide filters) to detect phase-amplitude coupling (Aru et al., 2015). However, as our results show, this low resolution potentially masks informative spectral coupling patterns such as harmonic structures. Along the same line, also the use of a variable frequency resolution across the cross-frequency spectrum may be problematic, as it may mask informative spectral patterns. Bicoherence allows to avoid these problems and to obtain high-resolution PAC spectra (Shahbazi Avarvand et al. 2018). Our results show, how such bicoherence spectra can reveal harmonic coupling patterns and how they can be readily combined with cross-frequency amplitude- and phase-coupling spectra.

3.5 The wave shape of oscillations

The first study of this thesis investigated the presence and the nature of cross-frequency relationships in the resting human brain that can be measured with MEG. After considering physiological artifacts and methodological caveats, we concluded that the dominant neuronal cross-frequency relationships that we observed in this data are best characterized as harmonic PAC. That is, we observed cortically wide-spread non-sinusoidal activity in a wide, alpha-band-dominated, frequency range. In other words, we observed the spectral cross-frequency patterns of non-sinusoidal oscillations (Giehl et al., 2021)

Going forward, the most significant neuroscientific finding of this first study was the abundant presence of non-sinusoidal wave shapes in the human brain. This observation accords well with other recent findings, which, taken together, indicate that non-sinusoidal wave shapes are a wide-spread, highly prevalent phenomenon in human EEG-, MEG- as well as ECoG (Electrocorticography) recordings (Giehl et al., 2021; Lozano-Soldevilla et al., 2016; Schaworonkow and Voytek, 2021). In the first study of this thesis, our findings were, however,

limited to demonstrating the presence and a temporal consistency of these waveforms. We did not yet analyze the shapes of these waveforms.

From a theoretical point of view, the importance of analyzing the wave shape of oscillations can be understood as follows: any local oscillation has a frequency, an amplitude, and a wave shape. The first two aspects alone do not define all potentially relevant features of non-sinusoidal oscillations. The wave shape includes additional dimensions of information about an oscillation, beyond frequency and power. This additional information has generally been available from neurophysiological recordings, but it has only sparsely been investigated before (Cole and Voytek, 2017). Studying wave shapes, therefore, equates to studying (additional) features of brain activity that are commonly present in electrophysiological recordings of oscillations, but that have previously remained largely uninvestigated.

Wave shapes may differ between functionally distinct brain areas and -oscillations, due to genetic variation, in relation to brain disorders, and wave shapes may change dynamically due to task demands (Cole and Voytek, 2017). In other words: wave shapes might be physiologically and functionally relevant; and the wave shapes of oscillations that can be recorded non-invasively with MEG might reflect characteristic physiological properties of the underlying neural networks. Moreover, recent evidence highlighted a functional significance of wave shapes in Parkinson's disease (Cole et al., 2017; Jackson et al., 2019) and a changed sensorimotor waveform in schizophrenic patients (Bartz et al., 2019).

Together, theoretical considerations and initial findings that non-sinusoidal wave shapes are not only a prevalent phenomenon, but also functionally significant, point to wave shapes as relevant and promising for basic and applied neuroscientific research in the future. Investigating the wave shapes of the non-sinusoidal alpha oscillations that we found in the first study was, thus, a logical next step. We aimed to answer the question, if the shape of these neuronal waveforms, as they can be observed in large-scale non-invasive resting-state MEG data, might potentially be physiologically or functionally relevant.

The most well-known example of a characteristic neural waveform in the human cortex may be the prominent alpha frequency range “mu” rhythm (Gastaut et al., 1952; Pineda, 2005; Tiihonen et al., 1989). This arch-shaped rhythm can be observed over the sensorimotor cortex, and its salient wave shape distinguishes it from the more sinusoidal occipital alpha rhythm (Kuhlman, 1978). Together with a third temporal “tau” rhythm, there are at least three functionally distinct alpha oscillations in the human cortex (Klimesch, 1999; Lehtelä et al., 1997; Niedermeyer, 1991, 1990; Tenke and Kayser, 2005). The actual number of distinct alpha oscillations may, however, currently still be unknown (Hari et al., 1997).

These three well-described different alpha oscillations have originally been distinguished based on their distinct responses to different tasks (Feshchenko et al., 2001; Klimesch, 1999; Tenke and Kayser, 2005; Tiihonen et al., 1991). If the wave shape of non-invasively recorded large-scale oscillations were to be functionally relevant, we would expect that functionally distinct rhythms could also be dissociated based on their wave shape – independent of task demands. The seconds study of this thesis aimed to address the question.

Any potential differences between independent waveforms, as well as any dynamic changes of wave shapes over time, can, however, only be studied to the extent to which their characteristic features can be measured and statistically represented. The methodology of wave-shape analysis was, therefore, a limiting factor for studying the wave shape of oscillations.

3.6 Current limitations of wave-shape analysis

The spectral analysis of non-sinusoidal wave shapes of oscillations has previously been suspected to be infeasible: a single narrow frequency band filter artificially imposes a quasi-sinusoidal wave shape, which effectively erases any wave-shape information. Broadband frequency analysis, in contrast, practically doesn’t permit the study of any one specific oscillation in isolation from other activity that is present concurrently. For these reasons, the study of wave shapes in the frequency domain is impossible with the use of a single

Fourier-based frequency band (Cole and Voytek, 2019). In consequence, wave shape has predominantly been studied in the time-domain.

To study wave shape in the time-domain, a select number of wave-shape characteristics are defined, and these features are evaluated on individual oscillation cycles that can be tracked in the time domain (e.g. Cole and Voytek, 2019). These select wave-shape features, however, do not describe wave shapes comprehensively, and additional functionally relevant wave-shape features may be missed (Cole and Voytek, 2017). Moreover, to assess the shape of waveform cycles in the time domain, an excellent signal-to-noise ratio is necessary. Because of this signal-to-noise limitation, wave-shape analysis in the time domain is generally limited to the most dominant rhythms, and non-invasive recordings such as MEEG and EEG are largely excluded.

Wave shapes cannot be analyzed in the frequency domain with the use of a single frequency band. However, wave shapes can be analyzed in the frequency domain by investigating the relationships between different frequency bands. That is, by evaluating the cross-frequency patterns that are associated with non-sinusoidal wave shapes. In this way, the most commonly used wave-shape features that were originally defined in the time-domain, have recently been evaluated in the frequency domain (Bartz et al., 2019): it was demonstrated that bicoherence, a measure that captures stable phase relationships between different frequencies, is directly related to the wave-shape features “peak-trough symmetry” and “rise-decay symmetry”. In other words, bicoherence is directly related to the two most prominently investigated wave-shape features: the relationship between the width of the peaks of a waveform relative to the width of its troughs (the “peak-trough symmetry”), and the relationship between the steepness of the rising phase of a waveform and the steepness of its decay phases (the “rise-decay symmetry”). Importantly, bicoherence was shown to be particularly robust in the presence of noise, indicating a clear advantage of the frequency-domain approach, when compared to time-domain based methods (Bartz et al., 2019). Other recent studies have, as well, already evaluated waveform features in the frequency domain by exploiting the cross-frequency relationship between different

frequency bands (Alian et al., 2022; Krishnakumaran et al., 2022; Milkovich et al., 2022).

What remained missing, however, was a spectral analysis method that fulfills both of two fundamental requirements: robustness in the presence of noise and overlapping neural activity; and thoroughly capturing all potentially relevant wave-shape properties. The second study of this thesis, therefore, used a novel wave-shape analysis method that fulfills both fundamental requirements.

4 Fourier-based waveform analysis dissociates human cortical alpha rhythms

4.1 Scientific questions and aims

We investigated how many, and which alpha oscillations may be dissociable in MEG resting-state recordings, solely based on their wave shape. If alpha oscillation waveforms that correspond to the three established alpha oscillations would be dissociable in MEG resting-state recordings, this could indicate that physiologically relevant wave-shape features may be assessed based on non-invasive data. The presence of more than three distinguishable wave shapes might indicate the presence of additional functionally distinct alpha oscillations, which could contribute to a more fine-grained understanding of the different neural oscillations that jointly inhabit the alpha-frequency range.

To date, the wave shape of neuronal oscillations has only been studied sparsely (Cole and Voytek, 2017), which may largely be a consequence of the current limitations of waveform-analysis methods. Currently available wave-shape analysis methods for neuronal data assess a select number of wave-shape characteristics; they do not to capture all potentially relevant wave-shape features (Cole and Voytek, 2017). In addition, the most common approach to analyze wave shapes is to assess wave shapes in the time domain, with inherently associated limitations regarding the signal-to-noise ratio (Bartz et al., 2019). This limitation is largely rendering systematic wave-shape analysis in non-invasive data impossible, other than, perhaps, for the very most prominent rhythms.

To avoid these limitations for the present study, we developed a novel wave-shape analysis method that assesses all potentially relevant wave-shape features and that is highly resistant to noise. This method assesses wave shape in the frequency domain, by exploiting the intimate relationship that exists between the observable wave shape in the time domain and the cross-

frequency patterns that define a periodic non-sinusoidal wave shape from the spectral perspective.

This novel waveform analysis approach permits the detailed reconstruction of a typical wave shape in the time-domain. Therefore, it is also possible to analyze established waveform features such as peak-trough- and rise-decay symmetries (e.g. Cole and Voytek, 2019): these time-domain-defined wave-shape features can be assessed directly on the detailed waveform reconstructions. To demonstrate the practicability of this approach, we used this additional approach to distinguish alpha waveforms based on peak-trough and rise-decay symmetry, besides using the complete set of waveform features as they are defined by the Fourier-based waveform analysis. In this way, the signal-to-noise advantages of our novel frequency-domain-based wave-shape analysis method can be combined with the freedom to investigate specific, previously defined wave-shape features.

4.2 Materials and methods

4.2.1 MEG recording & preprocessing

We used MEG recordings from the Human Connectome Project (Van Essen et al., 2013). The first two 6-minute resting-state sessions were available for n=89 subjects. Subjects were in supine position and fixating on a red fixation cross on a dark background during the recording.

The data was band pass filtered between 0.1 and 400 Hz, and notch filters were applied at 60±1 Hz and at the higher harmonics. Temporal segments with prominent artifacts were removed as defined in the “baddata” HCP pipeline. Muscle-, eye- and heart-related artifact components were identified by visual inspection and subsequently removed.

T1 weighted MRIs were used to warp the individual subject space onto common space for the construction of individual source models. We used the resulting transformation matrices that were available in the data set to warp individual subject space onto a source model with 457 source positions (Hipp

and Siegel, 2015). Source-level activity was estimated using linearly constrained minimum variance (LCMV) beamforming (Van Veen et al., 1997).

To compute bicoherence for the detection of ROIs with alpha waveform stability peaks, we used a frequency analysis with Hanning windowed FFT on 1-second-long segments of data. Windows were centered at intervals of 0.5 seconds, and zero-padded to a length of 2 seconds, which resulted in frequency bins that were spaced at 0.5 Hz intervals.

To extract most wave shape parameters, we used a frequency analysis with Hanning windowed FFT on 1-second-long segments of data, spaced at intervals of 0.125 seconds. The windows were padded to a length of 10 seconds, which resulted in frequency bins that were spaced at 0.1 Hz intervals.

The set-up and recording is described in detail in (Van Essen et al., 2013) and
http://www.humanconnectome.org/storage/app/media/documentation/s1200/HCP_S1200_Release_Reference_Manual.pdf.

4.2.2 Bicoherence

Bicoherence was computed for each of the two resting state recording sessions in every subject according to the following formula:

$$B(f_1, f_2) = \frac{<_t F_t(f_1) F_t(f_2) F_t^*(f_1+f_2) >}{<_t |F_t(f_1) F_t(f_2) F_t^*(f_1+f_2)| >} = \frac{\langle A_{f1}(t) A_{f2}(t) A_{f3}(t) e^{i(\varphi_{f1}(t)+\varphi_{f2}(t)-\varphi_{f3}(t))} \rangle}{\langle \left| A_{f1}(t) A_{f2}(t) A_{f3}(t) e^{i(\varphi_{f1}(t)+\varphi_{f2}(t)-\varphi_{f3}(t))} \right| \rangle}$$

(Equation 1)

$F_t(f)$ represents the complex time-frequency transformation at frequency f and time t. $<_t \ldots >$ indicates the temporal average, which was taken over the entire recording session of 6 minutes. $A_{f1}(t)$ is the amplitude time-series at frequency f_1 and $\varphi_{f1}(t)$ the corresponding phase time series. The numerator is the bispectrum and the denominator the normalization factor according to Hagihira et al. (2001). For estimates of coupling strength or “wave-shape consistency”, we used the absolute value of bicoherence.

For the localization of group-level spatial peaks of bicoherence, we normalized the absolute values of bicoherence to standard Z-scores against the distribution of 100 circularly time-shifted surrogates. To compute the absolute value of bicoherence for a surrogate, the time-series of f_3 ($f_3 = f_1 + f_2$) was shifted relative to f_1 and f_2.

4.2.3 ROI selection

To estimate alpha wave-shape consistency on the group level, we averaged the bicoherence Z-score values from the first recording session in the extended alpha frequency range: between f1 frequencies of 7 to 14 Hz, inclusive, and f2 frequencies up to 1.5 times the respective f1 frequency. The average over this frequency range was calculated per subject and at each cortical source location and then averaged over subjects. This resulted in a cortical distribution of the coupling strength between the fundamental alpha frequency and its first higher harmonic, which we used as a measure of alpha-frequency wave-shape stability.

The resulting cortical distribution was used to locate spatial peaks of alpha waveform shape stability. We selected spatial peaks from the subject average that exceeded an average bicoherence Z-score cutoff of 0.8 and that were not located on the caudal surface of the brain. For the two unilateral non-midline peaks (on the right superior parietal cortex and the left occipital cortex, respectively), the homologue locations on the other hemisphere were included, additionally.

For each single subject, we allowed a minimal variance of the individual source locations that were used for the respective ROI: we selected the source with the strongest individual alpha-range bicoherence from the source matching the subject-average peak location, or one of the adjacent source locations. Adjacent source locations that would be directly neighboring possible neighbors of a different ROI location were not selected.

4.2.4 Fourier series waveform analysis

The parameters characterizing waveform shape can be defined in the form of a Fourier series (see also Figure 7):

$S(t) = \sum_{k=1}^{n} A_k \cdot \cos(k \cdot 2\pi f_1 t + \phi_k)$ (Equation 2)

with $A_1 = 1$ and $\phi_1 = 0$.

S(t) represents a periodic waveform in the time domain (see Figure 7, middle). As a Fourier series, a periodic wave shape can be defined by three types of parameters: the first parameter, f_1, is the fundamental frequency of the waveform. A_k represents the amplitude of the phase-coupled k-th harmonic relative to the amplitude of the fundamental frequency, with $A_1 = 1$, and ϕ_k represents the relative phase between the fundamental frequency and the coupled k-th harmonics, with $\phi_1 = 0$.

In a waveform that is stable over time, the relationship between all harmonic waveform components is constant, or stationary, over time. Due to this stationarity of the cross-frequency relationship between the harmonic waveform components, it is possible to estimate the Fourier series waveform parameters by using adapted bicoherence-based measures. Below, we describe how we retrieved these three different waveform parameters from ROI source time courses with stationary alpha waveforms.

4.2.4.1 Fundamental alpha frequency (f_1) and the number of coupled harmonics (k)

To obtain the fundamental alpha frequency (f_1) for each subject, at every ROI and in each of the two sessions, we first located the individual bicoherence alpha peaks in the two-dimensional bicoherence cross-frequency spectrum ($B(f_1, f_2)$). For peak detection, f_2 frequencies up to 80 Hz, as well as f_2-frequency bins reaching 1 Hz below each f_1 frequency were included. Bicoherence cross-frequency spectra had been computed with bin spacings of 0.5 Hz. To improve the spectral precision of the detected fundamental and harmonic bicoherence peak frequencies, we first interpolated the absolute

values of the individual bicoherence cross-frequency spectra using splines to obtain bicoherence estimates at intervals of 0.1 Hz. Then, we averaged over the f_2 -frequency axis in the bicoherence cross-frequency spectrum and we located the maximum peak frequency between f_1 frequencies in the extended alpha range from 7 to 14 Hz.

To define the harmonics that were coupled to this f_1 frequency, we used the column of the bicoherence cross-frequency spectrum that corresponded to this f_1 frequency. We located the peak f_2-frequencies in this column. For a non-sinusoidal alpha oscillation, we expected consecutive alpha-harmonic f_2 -frequency peaks to be located at integer multiples of the alpha f_1 frequency. The significance of each f_2 peak was judged based on a significance mask of the entire cross-spectrum of the respective ROI at p<= 0.05, which was corrected for multiple comparisons using false-discovery-rate correction (Benjamini and Hochberg, 1995). Any consecutive significant harmonic (f_2-) frequency bicoherence peaks that were located within f_2-frequency ranges of $f_1 \cdot (k \pm 0.4)$ were then defined as the coupled harmonics. The number of significantly coupled harmonics corresponded to the number of these k significant consecutive harmonic peaks.

All subsequent analyses below were performed using the frequency analysis with estimates at every 0.125 seconds and 0.1 Hz, unless specified otherwise.

4.2.4.2 Relative harmonic phase ϕ_k

We reconstructed the pairwise relative harmonic phases (ϕ_k) from bicoherence phase angles. We defined $\phi_1 = 0$ and the relative harmonic phases ϕ_{k} for coupled harmonics k>1 were reconstructed as the cumulative sum over the harmonic bicoherence phases:

$$\phi_{\mathrm{k}} = \measuredangle e^{(-i \cdot \sum_{n=1}^{k-1} \measuredangle B(f_1, n \cdot f_1))} \qquad \text{(Equation 3)}$$

$\measuredangle$ denotes the angle (i.e., the argument) and $\measuredangle$B denotes the angle of bicoherence. This formula exploits a direct mathematical relationship between the phase of the harmonic bicoherence estimates and the pairwise relative harmonic phases that we needed to obtain; this formula is valid if and only if

harmonic coupling has already been confirmed (see Appendix A). We used this formula to obtain the pairwise relative phase between the kth harmonic and the fundamental alpha frequency f_1 for all significant higher harmonics.

We further ensured that these alpha harmonic bicoherence peaks indeed reflected harmonic coupling and could not be due to phase-amplitude coupling as follows. The presence of the first three or more consecutive harmonic bicoherence peaks indicates harmonic coupling. In the case of less than the first three harmonic bicoherence peaks, the first peak should be substantially stronger than a potential second peak for an unequivocal decision (Giehl et al., 2021). We checked if there were any cases with two alpha-harmonic bicoherence peaks, where the first harmonic peak was substantially weaker than the second peak.

4.2.4.3 Relative harmonic amplitude

To estimate the relative harmonic amplitude, we used the bispectrum with a custom-designed normalization factor. This normalization factor was designed specifically to retrieve the relative harmonic amplitudes from the bispectrum.

The relative amplitude between the first harmonic (k=1) and itself was defined as $\boldsymbol{A_{f1}} = 1$. Estimates of the relative harmonic amplitudes $\boldsymbol{A_k}$ for higher harmonics (k>1) were reconstructed as:

$$\boldsymbol{A_k} = \frac{\langle A_{f1}(t) A_{(k-1)\cdot f1}(t) A_{kf1}(t) e^{i(\varphi_{f1}(t) + \varphi_{(k-1)\cdot f1}(t) - \varphi_{k\cdot f1}(t))} \rangle}{\langle A_{f1}(t) A_{(k-1)\cdot f1}(t) A_{f1}(t) e^{i(\varphi_{f1}(t) + \varphi_{(k-1)\cdot f1}(t) - \varphi_{k\cdot f1}(t))} \rangle} \text{ (Equation 4)}$$

The dividend of Equation 4 is the bispectrum between a fundamental frequency $f1$ and integer multiples of this fundamental frequency and the divisor is the custom-designed normalization factor. $A_{k\cdot f1}(t)$ represents the amplitude time course, $\varphi_{k\cdot f1}(t)$ the phase time course of the k th alpha harmonic frequency, and $\langle\ \rangle$ denotes the average over time. Equation 4 is valid if and only if there is pairwise cross-frequency phase-coupling between all possible pairs of f_1, f_{k-1}, and f_k; which is the case for signals with higher harmonics (Appendix B). The obtained measure $\boldsymbol{A_k}$ is, in theory, a real number. Numerically and in a realistic setting, it is a complex number with a phase angle

close to zero. We used $\mathrm{real}(\boldsymbol{A_k})$ as the measure for the relative harmonic amplitude.

To confirm a distribution of $\measuredangle \boldsymbol{A_k}$ close to 0° phase angle, we calculated the circular variance over the phase angles of all estimates of $\measuredangle \boldsymbol{A_k}$. We defined circular variance as:

$Var_{circ}(Z) = E[|Z - E[Z]|]^2$ (Equation 5)

where $Z = 1e^{i\measuredangle \boldsymbol{A_k}}$ and $\measuredangle \boldsymbol{A_k}$ is the cosine phase angle of $\boldsymbol{A_k}$.

To compute $Var_{circ}(Z)$, we used the following computational form of Equation 5:

$Var_{circ}(Z) = E[ZZ^*] - E[Z^*]E[Z]$ (See Appendix C for the derivation of the computational form).

Here, $E[\,]$ indicates the expected value, | | the absolute value, $\measuredangle$ the cosine phase angle and Z^* the complex conjugate of Z. Equation 5 computes the distribution's average squared distance from the mean, fulfilling the definition of variance. For inputs in the form of $Z = 1e^{i\varphi}$, $Var_{circ}(Z)$ ranges between 0 if all phases φ are equal, and 1 for a uniform distribution of phases (Fisher, 1993). Equation 5 makes no assumptions about an underlying distribution.

Any estimates with an absolute phase angle of $|\measuredangle \boldsymbol{A_k} \geq \frac{\pi}{3}|$, as well as any estimates of a relative amplitude $\mathrm{real}(\boldsymbol{A_k}) > 1$, were excluded from further analyses.

4.2.5 Coupling strength

We used bicoherence to evaluate the temporal consistency of wave shapes, i.e., wave-shape stability. To evaluate the individual wave-shape stability, we extracted the absolute values of bicoherence at every harmonic peak for each subject, session, and ROI.

4.2.6 Handling the MEG phase-ambiguity

The 180° phase-ambiguity in the source-reconstructed MEG data might induce spurious differences in the relative harmonic phases between sources. In other words, a difference in the relative harmonic phases between sources might be due to only a random 180º phase-flip of one source with respect to a second source; that is, if the identical waveform at one source was mirrored across the time axis at the second source. We used a conservative approach to avoid this possibility: we commonly aligned all individual wave shapes into only one of the two possible directions. We determined which source time-series needed to be flipped by 180º based on the reconstructed waveforms' peak-trough and rise-decay symmetries. Together, peak-trough symmetry and rise-decay symmetry span a centrally symmetric space that contains all wave shapes independent of frequency, where a sinusoidal shape would be represented in the center, and more asymmetric shapes represented more distally. To determine the peak-trough and rise-decay symmetries of the theta/alpha waveshapes, we first reconstructed each typical alpha wave shape $x(t)$ for every subject and ROI in the time domain using Equation 1 and the derived wave shape parameters. We reconstructed 5 cycles of each waveform with 1000 equally spaced samples. Peak-trough symmetry (pt) is equal to Pearson's moment coefficient of skewness (s) of the signal (Elgar, 1987) and it was computed on the reconstructions $x(t)$ as follows:

$$pt_{x(t)} = s\big(x(t)\big) = \frac{E\left(\big(x(t) - E\big(x(t)\big)\big)^3\right)}{\sigma\big(x(t)\big)^3}$$

The rise-decay symmetry (rd) is equal to the negative skewness of the imaginary part of the Hilbert transform $\mathcal{H}$ (Elgar, 1987) and it was computed as:

$$rd_{x(t)} = -s(imag(\mathcal{H}(x(t)))$$

In the space spanned by pt on the x-axis and rd on the y-axis, we located that axis through the origin (using an axis width of 0.2, estimated in steps of 1°) that intersected the least number of wave-shape estimates in the joint distribution of all wave-shape estimates. This axis was the axis connecting

through 82°-0°-262°. Waveforms with $[pt, rd]$ representations located to the bottom-right of this axis were mirrored across the temporal axis and the waveform parameters of the flipped version were used. In this way, we enforced the highest possible similarity between all waveform shapes, given the 180° ambiguity of MEG recordings.

4.2.7 Waveform statistics

4.2.7.1 Distinguishing wave shapes

We used multivariate permutation statistics akin to nonparametric within-subject (repeated measures) MANOVAs. Effects were evaluated using 7 dependent variables: the fundamental alpha frequency f_1, the relative harmonic amplitudes A_k and relative harmonic phases ϕ_k for $k \in \{2,3,4\}$.

The testing protocol was outlined as follows:

1) We tested for significant waveform shape differences across sessions, separately for all 10 cortical ROI locations. Since no session difference was found, we kept "session" as an additional, untested factor in the following tests.
2) We tested for significant hemisphere differences, separately for all 4 pairwise ROIs. Since no significant side-difference was found, we kept "side" as an untested additional factor in the following tests.
3) We performed the main test of the study, assessing waveform shape difference across ROIs.
4) The main test was followed up with pairwise post-hoc tests, assessing differences between all possible ROI-pairs.
5) Second-order post-hoc results characterized the wave-shape differences: which wave shape parameters at which higher harmonics were different.

All the different nonparametric permutation MANOVAS followed the same logic:

1) We computed F values, as for a parametric within subject ANOVA, separately for f_1, the three A_k and for the three ϕ_k (the adaptations to

obtain F values for the circular ϕ_k-data is detailed further below). In this way, we obtained 7 separate F values, one for each of the dependent variables.

2) We used 5000 permutations of randomly reassigned ROI-labels. For each of these respective permutations we computed 7 permutation-F values. Testing against the permutations, we obtained one p-value for each of the 7 unpermuted F values, as well as one permutation-p-value for each of the 5000x 7 permutation-F values.
3) We applied Fisher's method (Mosteller and Fisher, 1948) and derived one X^2 value from the 7 p-values computed as:

$$\mathrm{X}^2 \sim -2\sum_{i=1}^{7}\log\left(p_i\right)$$

and we derived 5000 permutation-X^2 using the permutation-p-values
4) The X^2 value was then tested against the distribution of the 5000 permutation-X^2 values to obtain one p-value for each nonparametric permutation MANOVA. For the post-hoc pairwise MANOVAS, that is, for the pairwise ROI-comparisons, these p-values were corrected for multiple comparisons using false discovery rate correction (FDR, Benjamini and Hochberg, 1995).
5) In the pairwise ROI-comparisons only, the 7 separate F- and p-values of each pairwise MANOVA served as the second-order post-hoc statistic to characterize the nature of the waveform difference. These p-values were all together FDR-corrected for multiple comparisons.

To obtain ANOVA-analog F values for the circular relative harmonic phases ϕ_k, we transformed all ϕ to the form $Z = 1e^{i\phi}$ (with $\phi \in [-\pi;\pi)$).

Using the definition of circular variance given in Equation 5, we computed circular sums of squares (SS_{circ}) in the form of:

$SS_{circ}(Z) = \sum(ZZ^*) - \frac{\sum(Z)\cdot\sum(Z^*)}{N}$ (Equation 6)

where Z^* denotes the complex conjugate of Z (The derivation of Equation 6 is detailed in Appendix C). Apart from this adaptation, F values for the circular data were computed as for a regular parametric repeated-measures ANOVA.

4.2.7.2 Cross-session stability

We used Spearman correlation to correlate the fundamental alpha frequency, the relative harmonic amplitudes, and the bicoherence coupling strengths across the two recording sessions. The relative harmonic phases were correlated using a custom bootstrap permutation test, where the phase correlation (r_ϕ) between the two sessions (here A and B) was calculated as:

$$r_\phi = real(\langle 1e^{i\phi_B} \cdot 1e^{-i\phi_A} \rangle)$$

Here, ϕ_A represents the relative harmonic coupling phase of one subject at one ROI and one harmonic in session A, and $\langle\ \rangle$ denotes the average.

The resulting p-values were FDR-corrected for multiple comparisons, separately for each waveform parameter type, and jointly over all six ROIs and three higher harmonics (Benjamini and Hochberg, 1995).

4.2.7.3 Phase non-uniformities

We tested the non-uniformity of the distributions of the reconstructed relative harmonic phase, and the bicoherence phase, at every ROI and higher harmonic up to the sixth higher harmonic. We computed the mean vector length (vl) over subjects at every ROI and higher harmonic:

$$vl(\phi_1 \dots \phi_n) = \left| \frac{1}{N} \sum_{s=1}^{N} e^{i\phi_s} \right|$$

Here, s represents subjects. Significance of non-uniformity was determined with respect to the distribution of 1000 $vl_U(u_1 \dots u_n)$ drawn from $u_s \sim \mathcal{U}([0,2\pi))$. The resulting p-values were FDR-corrected (Benjamini and Hochberg, 1995).

4.2.8 Wave shape reconstruction

4.2.8.1 Group-level waveform shape reconstruction

To reconstruct the typical waveform shapes on the group level, we averaged the waveform-shape parameters of fundamental alpha frequency (f_1) and relative harmonic amplitudes (A_k) over subjects. The group-level relative harmonic coupling phases (ϕ_k) were reconstructed from the subject average bicoherence phases. We used Equation 1 and these group-level waveform parameters to reconstruct the group-level typical waveform shape for every ROI.

Following the results of the tests for phase non-uniformity, subject average waveforms were reconstructed including the waveform parameters from all $k = 1 \ldots K$ higher harmonics. The last higher harmonic (K) to be included was determined as the last higher harmonic that fulfilled the following requirements: at least 15 observations, and rejection of phase uniformity of the bicoherence phases at $p<0.05$ after FDR correction. This resulted in using $K = 5$ for the sensory-motor and the lateral parietal ROIs, $K = 4$ for the occipital ROI and $K = 3$ for the remaining ROIs.

4.2.8.2 Single subject waveform shape reconstruction and temporal excerpts

We reconstructed the typical alpha waveform of each ROI for two example subjects using Equation 1 with the respective waveform parameters. In this way, we obtained time-domain representations of the “typical” wave shape of these subjects at each ROI, as assessed by the Fourier-based waveform analysis method. To allow a visual comparison between these Fourier series waveform reconstructions and the original data, we additionally obtained corresponding time-domain data excerpts. We extracted one second of source reconstructed data from each respective ROI, centered around the time of maximum alpha amplitude. The time of maximum alpha amplitude was identified by repeating the time frequency analysis as described above, but using estimates in steps of 10ms, and smoothing the resulting amplitude time series of the individual alpha peak frequency by convolving it with a 1.5-second-long Hanning window

before locating the temporal maximum. The resulting excerpts were low pass filtered at 55 Hz using a fourth order Butterworth filter with forward and backward filtering.

4.2.9 Peak-trough and rise-decay symmetry for wave-shape distinction

We computed the peak-trough- and rise-decay symmetry for each individually reconstructed waveform $x(t)$ as described in section 5.2.6, and we tested for waveform differences as detailed in section 5.2.7.1. using the three dependent variables alpha frequency f_1, peak-trough symmetry pt and rise-decay symmetry rd.

4.2.10 Software

All analyses were performed in MATLAB (MathWorks Inc., Natick, USA) using the Fieldtrip toolbox (Oostenveld et al., 2011) and custom software.

4.3 Results

We developed a novel wave-shape analysis method that we applied to distinguish different cortical alpha oscillation wave shapes. In the first section of the results, we give a conceptual introduction to the Fourier series waveform analysis method. Whereas the remaining sections outline the scientific results of this study.

4.3.1 Fourier series waveform analysis

In this section, we first outline, how a periodic wave shape is represented in the frequency domain, and we summarize which parameters characterize a non-sinusoidal wave shape. Then, we explain the general working principles of how the Fourier series waveform analysis algorithm derives these parameters from the frequency domain data. Last, we point out the critical advantages of this novel wave-shape analysis approach.

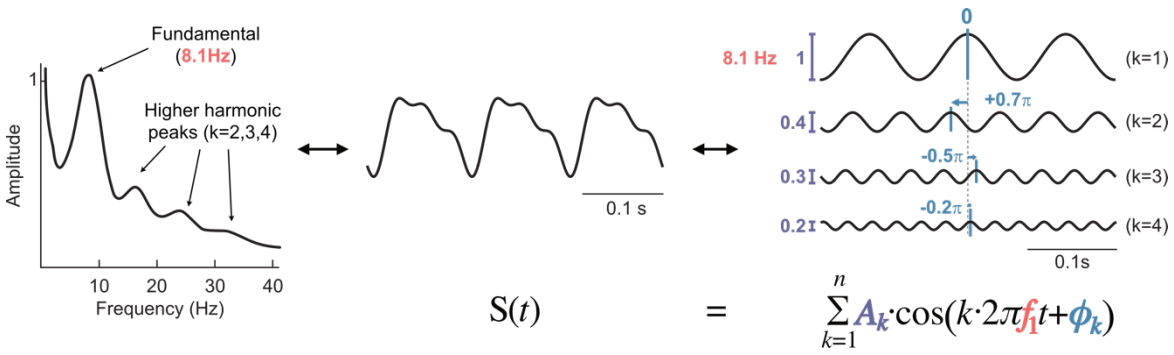

Figure 7. Wave shape represented as a Fourier series.

An example waveform (middle), harmonic peaks in the frequency spectrum (left) and the corresponding harmonic sinusoids (right) that, in their sum, reconstruct the shape of the waveform. The formal representation of this sum is a Fourier series (bottom). Each of the sinusoidal harmonic waveform components (right) contains amplitude-, as well as phase-shift information relative to the sinusoidal component at the fundamental frequency of the waveform. The relative amplitudes and -phases of each harmonic sinusoid jointly encode the wave-shape information. The three waveform parameters of alpha frequency (red), relative harmonic phase (blue) and relative harmonic amplitude (purple) are color-coded. The color-codes correspond to the representation of these parameters in a classical Fourier series (bottom), which formally characterizes non-sinusoidal periodic waveforms. Thus, the sum over all harmonically related sinusoids (right) reconstructs the original wave shape (middle).

The representation of a wave shape in the frequency domain can be understood as follows: a non-sinusoidal waveform in the time-domain (Figure 7, middle) can be defined by sinusoidal components (Figure 7, right), which are located at integer multiples of the waveform's fundamental frequency (Figure 7, left). The fundamental frequency of the waveform alone can only represent a (quasi-)sinusoidal signal (top sinusoid in Figure 7, right), whereas the entire wave shape can be reconstructed as the sum over all the separate sinusoidal waveform components. In other words, the non-sinusoidal shape of the waveform is defined by the combination of all its harmonic sinusoidal components. Each of the separate harmonic components contains a specific phase-shift relative to the fundamental waveform component, and a certain amplitude relative to the fundamental component (blue and purple, respectively, in Figure 7) and, jointly with the fundamental frequency (red in Figure 7), this information defines the specific wave shape. Formally, the spectral representation of a periodic wave shape can, thus, be defined in the form of a discrete Fourier series (Figure 7, bottom), with the Fourier series parameters characterizing the wave shape.

From the spectral perspective, the shape of a periodic waveform is, therefore, defined by the following three waveform parameters:

1) The fundamental waveform frequency f_1
2) The amplitude of the higher harmonic components relative to the fundamental component – their constant relative harmonic amplitude A_k
3) The phase of the higher harmonic components relative to the fundamental component – their constant relative harmonic phase ϕ_k

For a theoretical periodic wave shape signal without any additional noise, the harmonic frequencies could be extracted from a frequency representation of the signal and the relative amplitude and relative phase parameters could be derived directly. For neuronal data, however, this approach is not feasible, as there will always also be noise, or other neuronal activity, in these frequency bands. This noise or overlapping other activity will be affecting the relevant amplitude and phase information. Therefore, a different approach to extract the waveform parameters was necessary.

Our approach exploits a characteristic property of non-sinusoidal periodic wave shapes: for a particular wave shape, the fundamental waveform frequency, as well its characteristic relative phases and relative amplitudes, are constant over time, whenever the identical waveform is present. This means, that “relative” amplitude and “relative” phase imply a consistent cross-frequency relationship here. In other words: the wave-shape information is inherently encoded in the cross-frequency relationships between the harmonic wave-shape components. These cross-frequency relationships are consistent over time if the wave shape itself is consistent over time. In contrast, there is no such consistent cross-frequency relationship expected between, e.g., different frequencies of random noise. In consequence, it is generally possible to derive all relevant time-domain wave-shape features from the characteristic cross-frequency relationships of non-sinusoidal signals.

The bispectrum specifically captures stable phase relationships between different frequencies, while disregarding activity without such a relationship (Sigl and Chamoun, 1994) and it is particularly noise resistant (Bartz et al.,

2019; Giehl et al., 2021). This makes the bispectrum well-suited for wave-shape analysis. Even though the bispectrum does not readily provide all the relevant cross-frequency relationships in the required form, it does allow their reconstruction.

Using bicoherence (the normalized bispectrum), the fundamental frequency (f_1) can be located directly. The fundamental waveform frequency can be identified by determining the presence and spectral location of harmonic bicoherence peaks (Bartz et al., 2019; Giehl et al., 2021; Lozano-Soldevilla et al., 2016). The bispectrum does, however, not as readily provide the remaining Fourier series waveform parameters. As a solution to this problem, we devised an analytical approach that allowed us to derive these parameters: we reconstructed the relative harmonic phases (ϕ_k) from the bicoherence phase estimates of the relevant harmonic bicoherence peaks; and we derived the relative harmonic amplitudes A_k by using a custom designed, bicoherence-based normalization factor (see methods section for details). Our algorithm is effectively translating the relevant bispectrum estimates into the critical Fourier series waveform parameters. We will refer to this method below as “Fourier-based waveform analysis” (FWA).

FWA comes with several critical advantages:

1) FWA evaluates the stable relationship between different spectral signal components. Therefore, the FWA estimates are particularly resistant to spectrally overlapping random noise, or to overlapping neural activity without such a cross-frequency relationship. This property substantially increases the noise-resistance of the frequency-domain approach, compared to the time-domain approach (Bartz et al., 2019).
2) FWA can also be expected to segregate comparatively well between two spectrally overlapping non-sinusoidal oscillations that do each have a stable relationship between their respective harmonic signal components. This is the case, because FWA uses the two-dimensional bispectrum, which increases the overall distance between the signal components of spectrally overlapping non-sinusoidal oscillations, when compared to the one-dimensional power spectrum. A spectral distance

of, e.g., 1 Hz between peak frequencies translates to a spectral distance of 1 Hz in the power spectrum, as well as to a spectral distance of 1 Hz between the corresponding first harmonic bicoherence peaks. However, the spectral distance between the respective second (or third) harmonic bicoherence peaks in the two-dimensional bicoherence spectrum is already twice (or three times) as large. This naturally results in less overlap and less signal mixing between the higher harmonic components of different non-sinusoidal oscillations. In consequence, it leads to a more effective segregation, as well as to a more precise respective spectral localization of two spectrally overlapping oscillations, than could be achieved when using only the corresponding power-spectral representations.

3) FWA makes it possible to reconstruct a comprehensive and parsimonious waveform model (in the form of a Fourier series) from neuronal data. This approach is purely data-driven, and the full space of possible waveform features is accessible for statistical analysis. To our best knowledge, this is now possible for the very first time.

As an additional benefit, FWA allows the computation of traditionally time-domain based waveform parameters on FWA-based waveform reconstructions. This approach preserves the waveform-isolating advantages of FWA, while still allowing the use of specific, pre-defined waveform features.

4.3.2 Dissociating alpha wave shapes

We analyzed MEG resting-state data from two sessions and n=89 subjects of the human connectome project (HCP, (Van Essen et al., 2013)). We used source-reconstruction (Van Veen et al., 1997) and we focused on the alpha frequency range (7-14 Hz) to study cortical alpha waveform shapes. We located sources that were spatial peaks of alpha wave-shape stability, where wave-shape stability was operationalized as the bicoherence coupling strength between alpha and the first higher alpha harmonic. We then tested for differences between the wave shapes at these distinct alpha-waveform source locations using FWA waveform parameters. Moreover, we used the FWA waveform parameters to reconstruct individual- as well as subject-averaged

typical waveform shapes. These reconstructions were used to illustrate the performance of FWA, and to establish a bridge to time-domain-based wave shape measures.

4.3.2.1 Detecting spatial peaks of alpha waveform shape stability

If functionally distinct cortical alpha networks were associated with distinct alpha wave shapes, then these different cortical alpha networks could be located as distinct spatial peaks of alpha waveform shape stability. To localize such regions of interest (ROIs) with potentially distinct alpha wave shapes, we mapped the first harmonic bicoherence peak in the alpha-frequency-range (Figure 8A) over the brain (Figure 8B) and identified the most prominent cortical peak locations (Figure 8C). Alpha-waveform stability-peaks were found in sensory-motor, parietal, temporal, and occipital areas, as well as on the inferior parietal and superior parietal midlines. In occipital and lateral parietal areas, an evident peak in bicoherence was detected unilaterally, on the left occipital- and right lateral parietal cortex, respectively. For these latter unilateral peaks, we additionally included the respective homologue locations on the second hemisphere. The Z-scores of these two homologue locations differed by less than 0.05 to the respective peak on the opposite hemisphere.

In this way, six alpha waveform ROIs were identified at 10 ROI locations in total. Four of these six ROIs were bilateral, and two were midline ROIs. These peak locations of waveform shape stability served as the ROIs at which we subsequently analyzed the alpha waveforms.

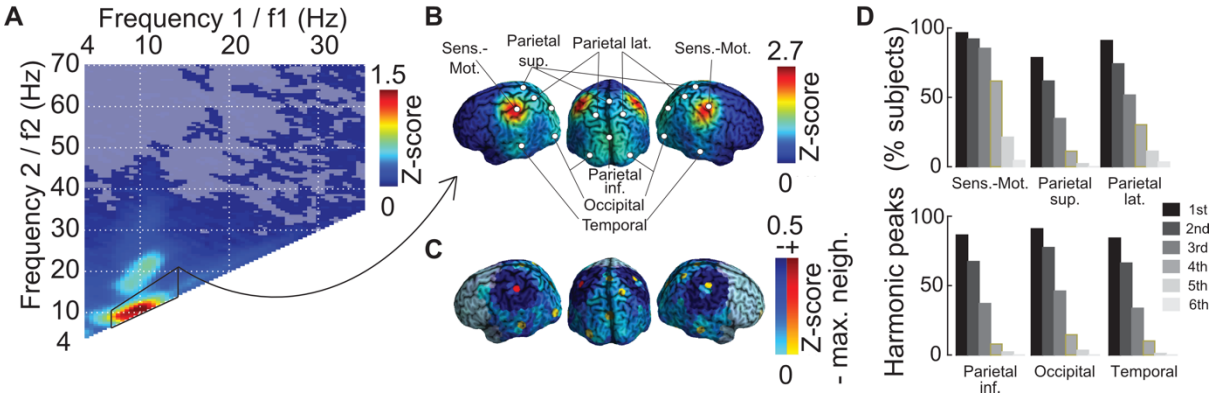

Figure 8. ROI selection.

(**A**) Bicoherence averaged across the brain. The alpha frequency range is marked in black around the first alpha-harmonic bicoherence peak. (**B**) Cortical distribution of the averaged cross-frequency range marked in A; average over subjects. ROI locations are indicated (**C**) Difference between local- and the maximum neighbouring bicoherence Z-score; local Z-scores < 0.5 are masked. Values greater than 0 indicate spatial bicoherence peaks which were used as ROI locations indicated in B. (**D**) Percentage of subjects with 1-6 consecutive significant harmonic bicoherence peaks at the different ROIs, corresponding to the number of coupled higher harmonics of alpha.

In every subject, ROI, and session, we located the strongest fundamental alpha frequency, based on the corresponding bicoherence spectrum. We then located up to six consecutive alpha harmonic bicoherence peaks and extracted the corresponding waveform parameters. We found two or more harmonic bicoherence peaks, that is, three or more harmonic components, in more than 50% of subjects at each of the six ROIs (Figure 8D). In the lateral parietal ROI, we identified three- and in the sensory-motor ROI we identified four or more harmonic bicoherence peaks in over 50% of subjects, in at least one of the two hemispheres. The lowest percentage of subjects with three consecutive harmonic peaks was found in the temporal ROI with 33.7%, the highest in the sensory-motor ROI with 85.4%. The percentage of subjects with four or more consecutive harmonic peaks ranged from 7.9% in the inferior parietal to 61.8% in the sensory-motor ROI. Due to the low percentage of subjects with four or more harmonic bicoherence peaks, we limited our statistical analyses of wave-shape differences between ROIs to the first three harmonic bicoherence peaks and, thus, we included waveform parameters of harmonic frequencies up to 4xf_α.

4.3.3 Reconstructing robust harmonic amplitude- and phase relationships

The FWA depends on robust estimates of the relative harmonic amplitude and relative harmonic phase between alpha and the higher alpha harmonics. These estimates were reconstructed using novel methodology that is based on the bispectrum. This bispectrum-based reconstruction is only valid where harmonic coupling has already been confirmed (see methods section for details). Harmonic coupling can be confirmed for significant bicoherence coupling peaks, when three or more consecutive harmonic bicoherence peaks have been detected, or when the first of two consecutive harmonic bicoherence peaks is not considerably weaker than the second peak, or when only the first harmonic bicoherence peak can be detected (Giehl et al., 2021).

In 89 subjects and 10 cortical locations we found 22 observations (1.8% of observations) where the second of two alpha-harmonic bicoherence peaks was numerically stronger than the first, thus, not unequivocally confirming harmonic coupling. For the remaining 98.2% of observations harmonic coupling was confirmed. The mean and standard deviation (SD) of the absolute value of the first bicoherence peak (not z-scored) over all observations was 0.39 and 0.19, respectively, and the mean and SD of the absolute value of the second bicoherence peak was 0.29 and 0.17, respectively. The mean absolute value of the first bicoherence peak of the 22 unclear observations was 0.16, with a SD of 0.8, for the second bicoherence peak the mean absolute value was 0.19 and SD 0.07. For the 22 unclear observations, the difference in coupling strength was small, and coupling overall was comparatively weak. Therefore, these observations were not excluded from further analyses.

The reconstructed relative amplitude is, in theory, represented by a real number; that is, by a complex number with a phase angle of zero (see methods section). Empirically, the joint distribution of the phases of the reconstructed relative amplitudes, over all subjects, ROIs, harmonics, and sessions, was centered on phase 0º with a circular variance of 0.06. Any estimates with a relative amplitude phase angle equal to or greater than $\pi/3$ (absolute value), or

with a relative amplitude real part greater than 1 were not counted as harmonic peaks and these observations were excluded from further analyses.

4.3.4 Distinct alpha waveform shapes

We tested for wave-shape differences using custom permutation-based nonparametric within-subject MANOVAs. These permutation MANOVAs were used to test for "wave-shape difference" by combining all separate waveform parameters and harmonics into a single statistical test using Fisher's method (Mosteller and Fisher, 1948). The p-values corresponding to these Fisher's X^2-statistics were obtained using a custom permutation test.

Before testing waveform differences between ROIs, we first tested for waveform differences between sessions and, where applicable, between hemispheres. We found no significant differences between sessions for any of the 10 cortical ROI locations (sensory-motor left: X^2=7.53, p=0.89; sensory-motor right: X^2 =14.49, p=0.41; superior parietal: X^2 =7.58, p=0.89; lateral parietal left: X^2=14.94, p=0.38; lateral parietal right: X^2=23.63, p=0.07; inferior parietal: X^2 =15.49, p=0.35; occipital left: X^2 =12.26, p=0.57; occipital right: X^2=9.38, p = 0.80; temporal left: X^2=11.53, p=0.64; temporal right: X^2=13.56, p=0.47; not corrected for multiple comparisons). Between hemispheres, no significant wave-shape hemisphere difference was found for any of the 4 bilateral ROIs (sensory-motor: X^2=19.61, p=0.16; lateral parietal: X^2=17.68, p=0.23; occipital: X^2=12.60, p=0.55; temporal: X^2=13.37, p=0.49; not corrected for multiple comparisons).

Subsequently, we tested for waveform differences between any of the six ROIs. The Null-Hypothesis of no wave-shape difference was rejected (X^2 =107.67, p<0.001). This main test was followed up with pairwise permutation-MANOVAs between all 15 pairwise combinations of ROIs (Figure 9A). We found significant wave-shape differences between all pairs of ROIs.

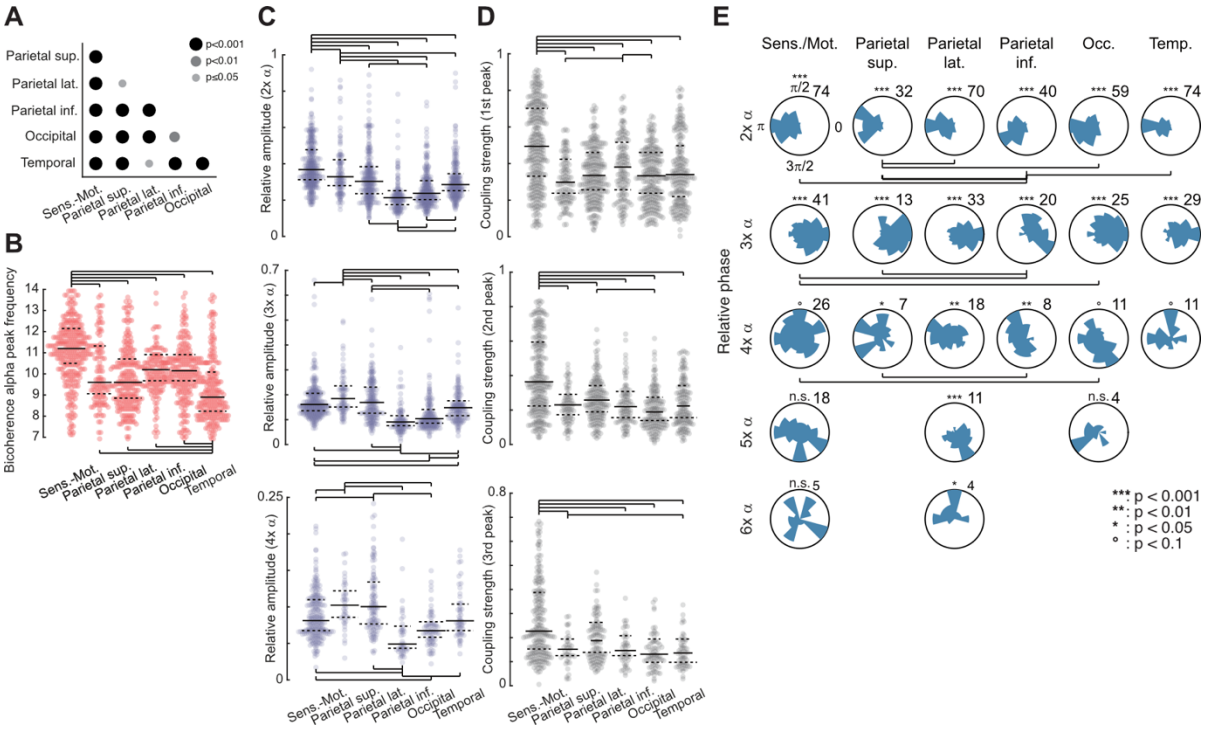

Figure 9. Waveform parameters.

(**A**) Pairwise wave-shape differences (corrected p-values) (**B-E**) Distributions of the different waveform parameters and of the coupling strength within each ROI. Medians are marked with solid lines in the violin plots and the dotted lines mark the 25th and 50th percentiles, respectively. Statistically significant distinctions are marked with solid lines above or beyond individual plots (p<0.05; corrected; permutation statistic). The color-coding matches the schematic representation of waveform shape parameters in Figure 7, except for grey: absolute value of bicoherence, a measure for waveform stability (**B**) Bicoherence alpha peak frequency (**C**) Reconstructed relative harmonic amplitude of the first three higher harmonics of alpha (**D**) Coupling strength / absolute value of bicoherence of the first three higher harmonics of alpha (**E**) Histograms of reconstructed relative harmonic phase of alpha, for all higher harmonics with ≥15 single observations, as it was used for single-subject waveform reconstructions and for all statistical analyses (only the first three relative harmonic phases were used for statistical analyses). Asterisks indicate significant phase non-uniformity (corrected for multiple comparisons). The numbers at the top right of the circular distributions indicate the axis labelling at the circle, representing number of observations.

The post-hoc tests that detailed in which specific parameters the waveforms between the respective ROI pairs differed, were obtained from within the permutation-MANOVAS, as the separate p-values which originally constituted the combined pairwise X^2-statistic. These separate p-values were derived by computing F-statistics as for parametric within-subject ANOVAs (in the case of the relative coupling phase we used a closely related circular adaptation), and

testing against random permutations (see methods section for details). The results are detailed in Figure 9 B,C and E, as well as in the text below:

The bicoherence alpha peak frequency differed significantly between the sensory-motor ROI and all other ROIs, as well as between the temporal ROI and all other ROIs (Figure 9B). There was no significant frequency difference between the parietal and occipital ROIs. There was only a non-significant tendency of a lower alpha peak frequency in the superior parietal and lateral parietal ROIs than in the inferior parietal and occipital ROIs.

Besides having the significantly highest bicoherence alpha frequency compared to all other ROIs, the motor ROI had the highest relative amplitude in the 2x α harmonic (Figure 9C). In the 3x and 4x α harmonic, the relative amplitude of the motor ROI was significantly higher than in the inferior parietal and occipital ROI and significantly lower than in the superior parietal ROI. In the 3x α harmonic, it was significantly higher than in the temporal ROI and in the 4x α harmonic it was significantly lower than in the lateral parietal ROI. The relative coupling phase of the sensory-motor ROI differed significantly to the parietal inferior ROI in the 2x α harmonic and to the occipital ROI in the 3x and 4x α harmonics (Figure 9E)

The superior parietal ROI had the second highest mean relative amplitude in the 2x α harmonic behind the motor ROI; it was significantly higher than in all other ROIs, except for the lateral parietal ROI (Figure 9C). Its mean relative amplitude in the 3x α harmonic was significantly higher than in any other ROI, including the sensory-motor ROI. In the 4x α harmonic, it was significantly higher than in the motor and the inferior parietal and temporal ROIs. The relative coupling phase of the superior parietal ROI differed significantly to the occipital ROI in the 2x α harmonic and to the inferior parietal ROI in the 3x and 4x α harmonic (Figure 9E). The only significant wave-shape differences between the superior parietal- and the lateral parietal ROI were found in the 3x α harmonic relative amplitude and 2x α harmonic relative phase. Furthermore, the distribution of the alpha frequency in the superior parietal ROI did not appear to be as clearly clustered as in the other ROIs (Figure 9B).

In all 3 higher harmonics, the relative harmonic amplitude of the lateral parietal ROI was significantly higher than that of the inferior parietal and occipital ROIs (Figure 3C). It was significantly lower than in the superior parietal ROI and significantly higher than in the temporal ROI in the 3x α harmonic. It was significantly lower than in the motor ROI in the 2x α harmonic, but significantly higher in the 4x α harmonic. The lateral parietal ROI had no significant coupling phase differences to any other ROIs except for the superior parietal ROI (Figure 9E). However, it had a non-uniform coupling phase distribution up to the 6x α harmonic, unlike any other ROI.

The inferior parietal ROI had the lowest relative amplitude in all 3 higher harmonics, although the difference to the occipital ROI was not significant in the 3x and 4x α harmonic (Figure 9C). The relative coupling phase of the inferior parietal ROI differed significantly to the sensory-motor, superior parietal and temporal ROIs in the 2x α harmonic (Figure 9E). It differed significantly to the sensory-motor and superior parietal ROI in the 3x α harmonic and to the superior parietal ROI in the 4x α harmonic. The only significant wave-shape difference between the inferior parietal- and the occipital ROI was found in the 2x α harmonic relative amplitude.

The occipital ROI had the second-lowest relative amplitude above the inferior parietal ROI, or at least a similarly low relative amplitude, in all three higher harmonics (Figure 9C). In the 2x α harmonic, its relative amplitude differed significantly from all five other ROIs. In the 3x harmonic, it was significantly lower than at all other ROIs, except for the inferior parietal ROI. In the 4x α harmonic, it was significantly lower than at the superior- and lateral parietal ROIs as well as at the sensory-motor ROI. The relative coupling phase of the occipital ROI differed significantly to the superior parietal ROI in the 2x α harmonic and to the sensory-motor ROI in the 3x and 4x α harmonic (Figure 9E).

The temporal ROI had the significantly lowest alpha bicoherence frequency, compared to all other ROIs (Figure 9B). It's relative amplitude in the 2x and 3x α harmonics was significantly higher than that of the inferior parietal and

occipital ROIs and significantly lower than that of the sensory-motor, superior- and lateral parietal ROIs (Figure 9C). In the 4x α harmonic it was significantly higher than in the inferior parietal ROI. The relative coupling phase of the temporal ROI in the 2x α harmonic differed significantly from the inferior parietal 2x α harmonic coupling phase (Figure 9E).

The coupling strength (Figure 9D), that is, the absolute value of bicoherence, was tested separately and was not included as a wave shape parameter. The sensory-motor ROI had the highest average coupling strength throughout the 2-4x α harmonics. The second highest coupling strength in the 2x α harmonic, in the inferior parietal ROI, differed significantly from that in the superior parietal ROI and the occipital ROI. The second highest coupling strength in the 3x and 4x α harmonic differed significantly from that in the occipital ROI in the 3x α harmonic. The superior parietal coupling strength was significantly higher than the temporal coupling strength in the 4x α harmonic. All other pairwise comparisons between ROIs were not significant.

In summary, we distinguished six cortical alpha wave shapes. A bilateral sensory-motor waveform, a medial superior parietal waveform, a bilateral parietal waveform, a medial inferior parietal waveform, an occipital waveform, and a temporal alpha wave shape. However, the occipital and inferior parietal waveforms only differed in a single parameter and the alpha frequency in the superior parietal ROI did not appear to be as clearly clustered as in the other ROIs. The inter-subject variability generally appeared high in all ROIs and for all wave shape parameters (Figure 9 B-E).

4.3.5 Alpha wave-shape stability

To quantify wave-shape stability across sessions, we correlated the waveform parameters over the two recording sessions. We found mostly moderate to strong correlations in all three waveform parameters, as well as for coupling strength (Spearman correlations for all parameters, except for coupling phase where we used a custom circular correlation statistic). The lowest cross-session correlation was generally found in the right occipital ROI, whereas the lateral parietal ROIs generally tended to have the strongest or one

of the strongest cross-session correlations. The bicoherence alpha frequency was correlated significantly ($p \leq 0.05$, corrected) at all ROIs and hemispheres and ranged between r=0.30 at the right occipital ROI and 0.70 at the right motor ROI with a mean of r=0.54. The 2xα relative harmonic amplitude was correlated significantly at all ROIs and hemispheres and ranged between r=0.39 at the right occipital and r=0.75 at the right lateral parietal ROI with a mean of r=0.60. The 3xα relative harmonic amplitude was correlated significantly at all ROIs except for the right occipital and right temporal ROIs and the significant correlations ranged between r=0.50 at the left occipital- and r=0.77 at the superior parietal ROI with a mean of r=0.65. The 4xα relative harmonic amplitude was still correlated significantly at the sensory-motor, lateral parietal and the inferior parietal ROI ranging between r=0.42 at the right motor ROI and r=0.87 at the right lateral parietal ROI with a mean of r=0.64. The 2xα relative harmonic coupling phase was correlated significantly across sessions at all ROIs, except for the superior parietal ROI. The range of significant correlations was between r=0.71 at the left superior parietal ROI and r=0.88 at the inferior parietal ROI with a mean of r=0.78. The 3xα coupling phase was correlated significantly across sessions at all ROIs, ranging between r=0.51 at the left occipital- and r=0.75 at the left temporal ROI with a mean of r=0.65. the 4xα coupling phase was significantly correlated at the sensory-motor, lateral parietal, inferior parietal, and temporal ROIs, ranging between r=0.40 at the left lateral parietal- and r=0.71 at the right temporal ROI with a mean of r=0.59 and at the left occipital ROI significance was missed barely with r=0.50 and p=0.053. P-values did not decrease linearly with increasing r-values, since the available number of observations differed across ROIs.

The additional parameter of bicoherence coupling strength correlated significantly at all ROIs at the 2xα coupling peak except for the superior parietal ROI. The significant correlations ranged between r=0.30 at the right occipital and r=0.70 at the right sensory-motor ROI with a mean of r=0.54. 3xα bicoherence was significantly correlated at all ROIs except the superior parietal ROI, and the left occipital ROI (p=0.07), ranging between r=0.39 at the right occipital and r=0.75 at the right lateral parietal ROI with a mean of r=0.60. 4xα

bicoherence was correlated significantly at the sensory-motor, superior- and lateral parietal ROIs, ranging between r=0.55 at the left lateral parietal- and r=0.77 at the superior parietal ROI with a mean of r=0.65.

4.3.6 Reconstructing typical alpha wave shapes

We used the FWA to reconstruct the typical waveform shapes from the waveform shape parameters. We used the average waveform parameters to reconstruct group-level typical time-domain waveform signals for each cortical waveform peak location; with the relative harmonic coupling phases being derived from the average bicoherence phases. The group-level waveform parameters uniquely characterized the typical local alpha waveform shapes (Figure 10A). In the case of the sensory-motor waveform, for example, the typical waveform evidently includes secondary peaks and troughs nested on top of the fundamental 11.2 Hz crests. The reconstructed waveform characterizes the observable wave shape in a purely descriptive manner. It does not make assumptions about underlying circuit dynamics that lead to a particular wave shape. In other words, the wave shape characterization does not answer questions such as whether this wave shape is typically caused by a single complex-shaped 11.1 Hz process, or by two or more independent processes with a harmonic frequency-relationship that are stationarily phase-coupled.

The relationship between the FWA wave-shape reconstruction and the source data time courses, centered on the time of maximum alpha amplitude, is displayed in Figure 10B (left and right, respectively) for two example subjects and all six ROIs. The individual wave shape examples were reconstructed using waveform parameters that were estimated over the entire first recording session. For all these examples, a close resemblance between the reconstructions and at least some of the waveform cycles of the excerpts can be observed. The waveform variability observable in the data excerpts can be caused by variability in the neural waveform generating process itself, by interference from other neural processes in frequency-ranges that overlap the frequency ranges of one or more harmonic components of the reconstructed waveform, or by a combination of the two.

All features that are observable in the FWA time-domain reconstructions are based in- and, thus, are directly related to the Fourier-domain based waveform parameters of wave frequency, relative harmonic amplitudes and relative harmonic coupling phases. Therefore, every observable aspect of the reconstructions was accessible to the statistical waveform analysis.

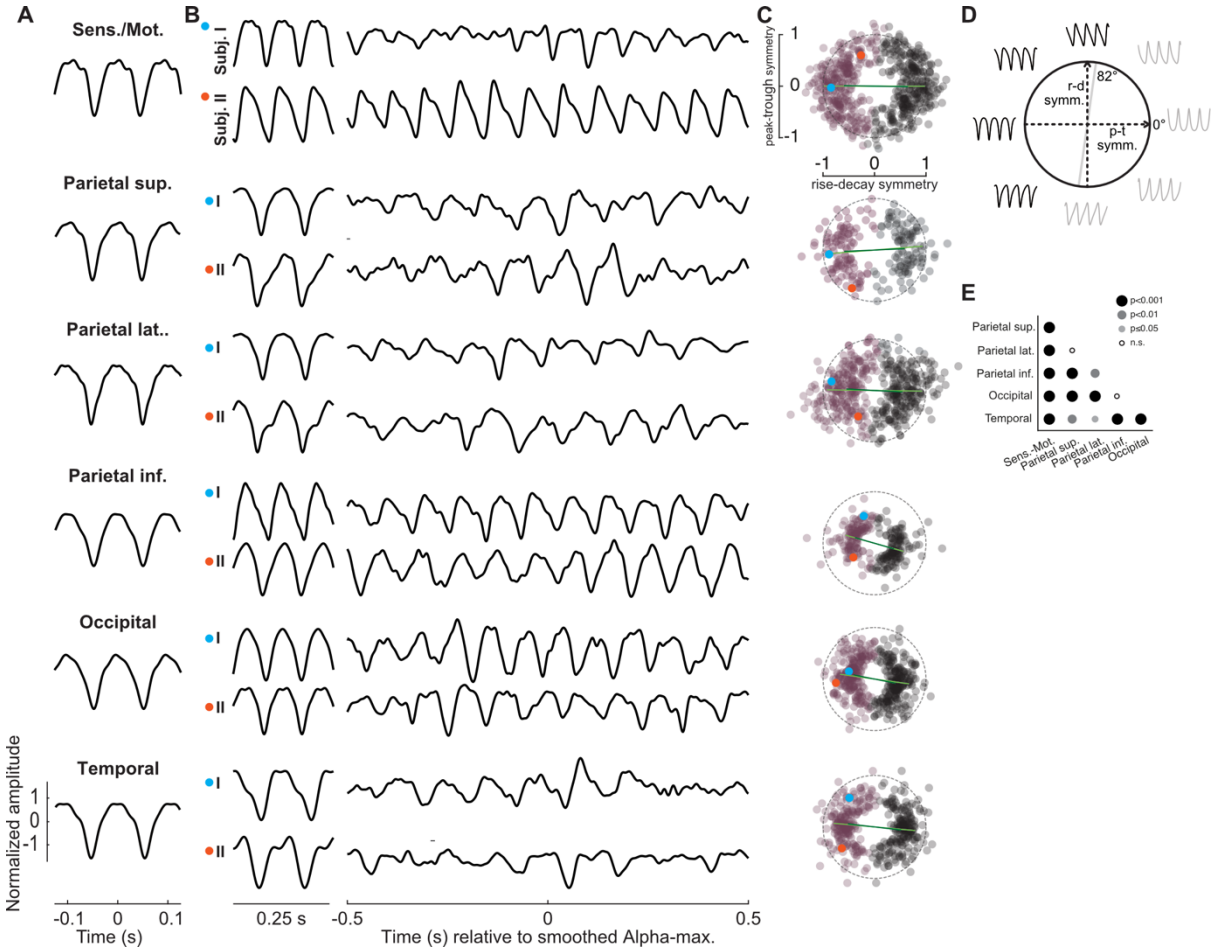

Figure 10. Waveform shape reconstructions.

(A) Waveform reconstructions for the six ROIs (top to bottom) using the respective averaged bicoherence alpha frequency, the average reconstructed relative harmonic amplitudes and the relative harmonic phase reconstructed from the average harmonic bicoherence phases. **(B)** Individual wave shape reconstructions of two exemplary subjects (I - blue & II - orange) at each of the six ROIs using the individual local bicoherence alpha frequency, the individual reconstructed relative harmonic amplitude, and the individual reconstructed relative harmonic phase (left). Corresponding source time-course excerpts centred around the time with maximum alpha amplitude, low-pass filtered at 55 Hz (right). (**C**) Distribution of rise-decay and peak-trough (a)symmetry of all reconstructed waveforms at each of the six ROIs (red) and of the same waveforms mirrored across the temporal axis (black; 180° phase-flip). The single subject examples from B are marked in blue (example subject I) and orange (example subject II). Dotted: unit circle; dark green lines: average peak-trough symmetry plotted against the average rise-decay symmetry; light green lines: group-level reconstructions' peak-trough symmetry plotted against the rise-decay symmetry. A

location closer to the center of the circle corresponds to a more sinusoidal waveform, whereas a less centralized location corresponds to a more non-sinusoidal waveform (**D**) Schematic of approximate waveform shape based on the ratio (the angle) of peak-trough- (p.-t.-) to rise-decay symmetry (r.-d. symm.) (Appendix D). The least amount of single-subject, single-ROI waveform observations fell into the axis through 82°-0°-262° (± a parallel border region of 0.1) and time courses corresponding to waveform signals to the right side of this axis (wave shapes in grey, black circles in C) were mirrored along the time axis (wave shapes in black, red circles in C) prior to any statistical waveform analysis, to account for the 180° phase-ambiguity. (**E**) Pairwise wave-shape differences based on peak-frequency, rise-decay and peak-trough symmetry (corrected p-values)

4.3.7 FWA based rise-decay and peak-trough (a)symmetry

Time-domain based waveform statistics such as the peak-trough- and rise-decay symmetry can be estimated directly from the FWA time-domain reconstructions (Figure 10C). We repeated the tests for waveform shape differences between sessions, hemispheres and ROIs using the waveform frequency and reconstruction-based peak-trough and rise-decay symmetry as waveform parameters. These traditionally time-domain based waveform parameters performed nearly as well in waveform differentiation as directly using the native FWA parameters. No significant statistical differences were found only in the pairwise permutation-MANOVAs between the superior- and lateral parietal ROIs, and between the inferior parietal and occipital ROIs (Figure 10E). As with the native FWA parameters, no significant waveform difference was found between sessions (sensory-motor left: X^2=2.80, p=0.84; sensory-motor right: X^2 =1.62, p=0.95; superior parietal: X^2 =4.07, p=0.67; lateral parietal left: X^2=8.91, p=0.18; lateral parietal right: X^2=2.56, p=0.84; inferior parietal: X^2=5.83, p=0.45; occipital left: X^2=9.26, p=0.16; occipital right: X^2=7.10, p = 0.31; temporal left: X^2=6.24, p=0.39; temporal right: X^2=9.07, p=0.17; not corrected for multiple comparisons) or hemispheres (sensory-motor: X^2=-1.29, p=0.09; lateral parietal: X^2=-0.25, p=0.65; occipital: X^2=0.53, p=0.24; temporal: X^2=1.04, p=0.13; not corrected for multiple comparisons).

5 Discussion

In the second study of this thesis, we introduced FWA, a new framework that characterizes the wave shape of neuronal oscillations based on their harmonic profile in the frequency spectrum. That is, based on the characteristic cross-frequency features of non-sinusoidal waveforms. Using this new approach we show, to our knowledge for the first time, that multiple cortical alpha waveforms can be detected and distinguished in human resting-state MEG data. Besides the well-established occipital, sensory-motor and temporal alpha rhythms, we found evidence for the presence of additional alpha rhythms with a distinct waveform. The observed waveform parameters, moreover, remained stable across recording sessions. This suggests that they may reflect characteristics of underlying alpha oscillations that may be stable over time.

5.1 Analyzing the waveform shape of oscillations in the frequency domain

Our new approach to analyse wave shape distinguished neural alpha waveforms by extracting detailed information about the wave shape using the conventional Fourier spectrum. This approach critically extends previous approaches in characterizing wave shapes.

The methodology of FWA critically relies on measures of the bispectrum. Bicoherence, one bispectral measure, was already proven a measure with high robustness to noise and to unrelated neural activity (Bartz et al., 2019; Giehl et al., 2021). It performs better than wave-shape analysis in the time domain and is still applicable even when the signal may not be directly observable in the time domain (Bartz et al., 2019). This advantage of the bispectrum can be easily explained as follows: the bispectrum, in difference to the more familiar power spectrum, specifically characterizes the dependencies between different spectral frequencies of a recorded signal, while disregarding unrelated contents of the signal (Sigl and Chamoun, 1994). As such dependencies are a particular feature of non-sinusoidal waveforms, the bispectrum is perfectly

suited to specifically extract the wave-shape information from the frequency spectrum. FWA capitalizes on this advantage of particular noise resistance and on the disregard for unrelated signal components, which may be impossible to achieve using time-domain based approaches. Thus, FWA allows studying the wave shape of comparatively weaker waveforms with a signal-to-noise ratio that may be insufficient to even allow any wave-shape analysis in the time domain. This advantage of FWA over the time-domain based approach is particularly relevant for the study of non-invasively recorded neuronal waveforms, such as MEG or EEG.

FWA analyses wave shapes holistically. It is not limited to any pre-defined wave shape parameters, but it encompasses all the wave-shape information that can be extracted from the data. That notwithstanding, we demonstrated that it is still possible to obtain already well-established wave shape parameters such as peak-trough symmetry and rise-decay symmetry from the FWA waveform reconstructions. This approach to compute the traditionally time-domain-derived measures conserves the noise-resistance of FWA and it may be useful for applications that rely on specific pre-defined wave-shape markers. We also showed that peak-trough symmetry and rise-decay symmetry, in conjunction with waveform frequency, were still outperformed by the native FWA waveform parameters in terms of their sensitivity to distinguish between different wave shapes. FWA can make even very detailed waveform patterns accessible to statistical analysis if they are present in the frequency domain data and sufficiently stable over the time being analyzed.

It could be argued, that FWA, in contrast to wave-shape analysis in the time domain, does not allow a time-resolved wave-shape analysis. We did not apply a temporally resolved version of FWA in the present study. However, the frequency, relative harmonic phases and relative harmonic amplitudes of a stationary waveform are stationary over time. Therefore, these parameters could be obtained, and they could be analyzed in a time-resolved fashion, if and at the times when the presence of one non-sinusoidal alpha oscillation at a certain frequency has already been confirmed; and if it seems advantageous

for a particular application or research question. FWA does not generally preclude a time-resolved study of wave shapes.

5.2 Dissociating multiple alpha rhythms

It is already well-known, that “the” alpha rhythm is not a single oscillation. Yet, it currently remains uncertain how many alpha rhythms there may be. To date, three alpha rhythms have been generally recognized in the human brain, that have been distinguished based on their distinct functional responses and cortical source locations (Feshchenko et al., 2001; Klimesch, 1999; Tenke and Kayser, 2005): a prominent visual alpha (Berger, 1929), the idiosyncratic motor mu rhythm (Gastaut et al., 1952; Pineda, 2005) and a “third”/”tau” alpha rhythm that is located over the temporal cortices and which is generally less easily observable than the other two (Niedermeyer, 1991, 1990). The distinct temporal, sensory-motor and occipital alpha waveforms that we observed appear to conform well with these previously identified alpha oscillation sources.

5.3 Parietal alpha as a fourth alpha rhythm

We did not only distinguish three different alpha waveforms, but six. It could be argued, that volume conduction and signal mixing between different non-sinusoidal alpha sources might have resulted in some intermediary wave shapes to be recorded at some intermediary located source positions (Bartz et al., 2019), and we cannot entirely refute this argument. It is, in fact, very unlikely that we recorded alpha waveforms at sources without at least some alpha signal mixing; particularly so, because the group-level ROIs may not have been an optimal match for every single subject.

In the midline superior parietal ROI, there may be considerable signal mixing at play. This ROI’s 2x α harmonic coupling phase and 2x α harmonic coupling strength were not correlated across the two recording sessions. This could indicate that the waveform observed at this ROI may not be representing a consistent alpha oscillation. This ROI was particularly similar to the lateral

parietal ROI, differing only in the 2x α harmonic coupling phase and 3x α harmonic relative amplitude. This ROI location might only have appeared as a separate spatial peak on the midline surface due to our use of a source model that is restricted to the outer cortical surface. Thus, we can currently not exclude, that this ROI's relatively flatter distribution of bicoherence alpha frequency, in combination with its location on the midline, could indicate, that there may be some influence from sensory motor- or even inferior parietal alpha sources besides the lateral parietal alpha at this location, and that the limited wave-shape difference to the lateral parietal ROI might be explained by these effects.

Furthermore, we can currently not exclude the possibility that the occipital and inferior parietal waveforms might be reflecting a single underlying alpha oscillation. Their waveform difference is small and was limited exclusively to the relative amplitude of the 2x α harmonic. As an additional difference, the coupling strength of the occipital ROI was significantly lower than that of the inferior parietal ROI (Figure 3D). This might, however, have been due to low signal to noise of the occipital alpha rather than to an actual difference in waveform stability. A dataset with stronger occipital alpha, e.g., in an eyes-closed setting, may be useful to clarify the question, if the occipital- and a potentially separate inferior parietal waveform may be more clearly distinguishable in the presence of stronger occipital alpha oscillations.

The third alpha waveform that did not match the known three alpha oscillations could, however, not be as easily refuted. The superior parietal waveform only differed significantly from the temporal waveform in their alpha bicoherence frequency and in the relative amplitude of their 2x α harmonic. However, unlike in the previously mentioned questionable cases, neither of these two ROIs was a midline ROI. Moreover, their spatial location was considerable further apart, and the area between the two was either dominated by the sensory-motor rhythm along the central sulcus, or by a parietal area with considerably lower bicoherence coupling strength. Thus, it appeared unlikely, that the lateral parietal waveform, as we observed it, could predominantly reflect a volume-conducted temporal alpha-frequency range oscillation, or vice-

versa. A certain wave-shape similarity to the temporal wave shape may even be related to a certain functional similarity, as temporal and parietal association cortices.

The superior parietal waveform could not be explained by the waveforms at the other remaining ROIs, either: the lateral parietal wave shape was clearly different from the sensory-motor waveform: the significantly different bicoherence alpha frequency, as well as the different dynamic of relative amplitude – significantly lower relative amplitude in the lateral parietal than in the motor ROI in the 2x α harmonic, but significantly higher in the 4x α harmonic (Figure 9C) – clearly distinguished it from the sensory-motor ROI. Even though the superior parietal ROI was located spatially in-between the inferior parietal (and occipital), and the sensory-motor ROIs, its bicoherence alpha frequency was not intermediary to that of the other two (Figure 9B). Therefore, it seems quite unlikely that the lateral parietal alpha waveform may have resulted as a linear signal mixture between occipital/inferior parietal and sensorimotor alpha.

Even though the frequency difference between the superior parietal- and the inferior parietal or the occipital ROI was not significant, which might have been due to some extend of signal overlap, they still clearly differed in their relative harmonic amplitude, consistently in all higher alpha harmonics. Thus, the lateral parietal waveform clearly appeared to be distinct from the inferior parietal or occipital wave shapes.

In addition to these respective pairwise differences, the relative harmonic coupling phase of the lateral parietal ROI appeared to be the most consistent over subjects. No other ROI had a significantly non-uniform distribution of coupling phase beyond the 4x α harmonic. Whereas the coupling phase distribution of the lateral parietal ROI was significantly non-uniform up into the 6x α harmonic (Figure 9E). Thus, the lateral parietal alpha waveform may, in fact, be the alpha wave shape that was most consistent across subjects.

Taking all these aspects together, our findings strongly indicate the presence of a lateral parietal alpha oscillation with a wave shape that is distinct from the waveforms that were associated with the three previously well-established

alpha frequency-range rhythms. It has already been suggested before, that parietal and occipital alpha oscillations might represent functionally distinct rhythms (Barzegaran et al., 2017; Haegens et al., 2014; Sokoliuk et al., 2019) and different occipitoparietal sources demonstrably show heterogeneous responses to visual stimulation (Nuttall et al., 2022). Our observation of a distinct parietal alpha waveform conforms well with these findings. We conclude, therefore, that there appear to be at least four distinct alpha oscillations in the human brain. While, currently, the question remains open whether we may have additionally observed a distinct inferior parietal and/or superior parietal waveform. If confirmed in further studies, the latter might represent a fifth and sixth distinct alpha rhythm.

5.4 Waveform shape as a new window into circuit interactions

Distinguishing alpha oscillations based on their wave shape could make them accessible as separate biomarkers. The differentiated evaluation of alpha oscillations may, for example, allow to pinpoint the functional differences in brains with a neurological or psychiatric disorder more precisely. Alpha sub-bands have already been observed to behave in functionally different ways (Klimesch, 1999, 1997; Klimesch et al., 1998, 1996; Wu et al., 2015) and they were, moreover, related differentially to neurodevelopmental disorders (Debnath et al., 2020; Murias et al., 2007; Van der Lubbe et al., 2019). Such functionally distinct alpha sub-bands could likely be related to distinct underlying alpha oscillations that also produce distinct wave shapes.

Wave shape may be a valuable biomarker. Wave shape represents new dimensions of information that are independent of frequency and amplitude and that could prove useful as complementary diagnostic markers. First notable findings have already been made that strongly support the relevance of changes in waveform parameters as physiological indicators in neurological and psychiatric disease, in particular regarding Parkinson's disease (Cole et al.,

2017; Jackson et al., 2019; O'Keeffe et al., 2020) and Schizophrenia (Bartz et al., 2019).

Wave shape is, furthermore, informative towards the mechanisms that may generate a certain rhythm (Cole and Voytek, 2017; Krishnakumaran et al., 2022). Therefore, wave shape could, eventually, also be informative towards disease-related changes in these mechanisms.

We hope that our comprehensive and widely applicable approach to study wave shape in the Fourier domain will contribute to significantly widen this new window into the analysis of neuronal oscillations.

5.5 Characterizing cross-frequency relationships

Together, the two studies of this thesis mapped and characterized cortical cross-frequency relationships in humans, as they can be observed non-invasively using MEG in resting-state. The dominating neuronal cross-frequency patterns were related to non-sinusoidal oscillations in the alpha-frequency range; and the characteristic cross-frequency features of non-sinusoidal wave shapes may allow the dissociation between functionally distinct alpha oscillations based on their wave shape.

In the first study, we developed a framework to dissociate the spectral nature of cross-frequency signals, and to distinguish between two fundamentally different cases: phase-amplitude coupling between distinct oscillations, and non-sinusoidal wave shapes. Using this framework, we systematically mapped cross-frequency relationships over the human cortex as well as in a wide range of frequencies. We detected no conclusive evidence for canonical phase- to amplitude coupling in the resting state. Instead, we observed a wide cortical distribution of non-sinusoidal theta/alpha oscillations. Furthermore, we showed how spurious phase-amplitude coupling across wide frequency ranges can be caused by physiological artifacts and spectral leakage. (Giehl et al., 2021)

In the second study, we presented an analytical method to analyze non-sinusoidal wave shapes from the spectral perspective, that is, based on their

inherent and characteristic cross-frequency relationships. This tool is particularly noise resistant, and it assesses all potentially relevant features of asymmetric periodic waveforms. Thus, this novel tool first permitted a systematic and comprehensive wave-shape analysis in non-invasive MEG data. Using this tool, we distinguished what are likely functionally distinct occipital-, parietal-, temporal- and sensorimotor resting-state alpha oscillations, solely based on their differentiable non-sinusoidal wave shapes.

Cross-frequency wave-shape features reflect additional dimensions of information about oscillations that are complementary to the band-limited amplitude and phase information (Bartz et al., 2019). The analysis of cross-frequency features may, in consequence, facilitate deeper insights into the mechanistic and functional properties of neuronal oscillations. However, two prerequisites still needed to be fulfilled for a systematic use of this additional information:

1) Since canonical phase-amplitude coupling and wave-shape-related cross-frequency features relate to distinct generative and functional mechanisms, a clear distinction between the two was a prerequisite for the correct interpretation of the measured cross-frequency relationships.

2) The detailed characterization of all potentially relevant wave-shape features was a prerequisite to exploit the full potential of this additional information about oscillations.

The two studies of this thesis provided the respective methodological tools that, together, filled both prerequisites.

5.6 Task modulation

The first study of this thesis mapped cross-frequency patterns in humans in resting-state, and no canonical non-harmonic phase-amplitude coupling could be found. This result might, however, be specific to the resting state. Non-harmonic PAC could be observable in task contexts. These findings clearly demonstrated, however, that great care is necessary for the interpretation of

observed phase-amplitude coupling. (Giehl et al., 2021) An equal level of care will be necessary for the interpretation of observations of cross-frequency coupling in task contexts.

In the second study of this thesis, we described a cortical map of different theta/alpha oscillation wave shapes in resting state. It remains to be investigated how wave shapes may change in the context of different tasks. Moreover, task contexts that are associated with higher power in the delta, beta, or gamma frequency bands than the resting-state might be useful to facilitate the study of the wave shapes in different frequency ranges beyond theta and alpha.

Our novel wave-shape analysis tool descriptively characterizes the shape of a periodic waveform as it may typically be observed in the signal. It currently remains unclear, to what extend the alpha-oscillation wave shapes that we observed are generated by single non-sinusoidal oscillators. The observed wave shapes might as well be the result of two or more distinct oscillators that are operating at harmonically related frequencies, and which are cross-frequency phase-phase as well as cross-frequency amplitude-amplitude coupled in the resting state. One approach to address this open question could be the experimental modulation of oscillations. An evident first candidate for this approach may be the sensorimotor (alpha-frequency range) mu rhythm, and the possible dynamics of its wave shape in relation to the well-described event-related mu and beta desynchronization and to the post-movement beta rebound.

The sensorimotor mu and beta frequencies might be harmonically related frequencies (Pfurtscheller et al., 1997; Salmelin et al., 1995; Salmelin and Hari, 1994). Therefore, these components might constitute the prominent sensorimotor mu wave shape as we also observed it in the second study of this thesis. Sensorimotor mu and beta markedly present with differing temporal dynamics, which seems to be speaking against a single neural generator for both components. While mu as well as beta are, e.g., both suppressed during movement, beta reemerges before mu (Leocani et al., 1997; Salmelin and Hari, 1994) and only beta shows a post-movement rebound, that is, a clear increase

in power above baseline level (Cardellicchio et al., 2020; Jurkiewicz et al., 2006). Moreover, the location of these two rhythms is only partially overlapping; the beta component could be attributed more likely to the motor cortex and the mu component more likely to the sensory cortex (Jurkiewicz et al., 2006; Salmelin and Hari, 1994). These observations may lead to the expectation, that the sensorimotor mu waveshape could, in fact, reflect cross-frequency coupling between independent oscillations, rather than reflect the physiological properties of a single non-sinusoidal oscillator. The coupling between these distinct sensorimotor oscillations might be dynamically adapted during sensory and/or motor tasks and it may facilitate sensorimotor integration.

However, there is likely not only one type of sensorimotor beta. Besides mu-harmonic beta, movement-related beta that was not harmonic to the mu rhythm has also been described, and this independent beta rhythm can even present with its own higher harmonic component (Pfurtscheller et al., 1997). Thus, it currently remains unclear, which of the different beta components is responsible for the observable difference in the temporal dynamics and in the spatial location between sensorimotor beta and sensorimotor mu: the mu-harmonic beta, a second beta rhythm, or both. This question cannot easily be answered by regarding the temporal dynamics and the spatial distribution of only the power of mu and beta. Therefore, the question remains open, whether the mu waveform may reflect the physiological properties of a single neural generator or the cross-frequency coupling between independent oscillations. Wave-shape analysis in the appropriate task contexts may help to address this questions and related questions, by dissociating the involved rhythms and their dynamics more clearly, based on their wave shapes or harmonic coupling profiles in addition to power.

5.7 The healthy and the diseased brain

Various psychiatric and neurological disorders have been associated with changes in neuronal oscillations (Başar, 2013; Başar and Güntekin, 2013; Buzsáki and Watson, 2012; Herrmann and Demiralp, 2005; Mathalon and

Sohal, 2015; Vinogradov and Herman, 2016). Most of these observations, to date, relate to power- and connectivity changes within certain frequency bands. Cross-frequency interaction patterns of oscillations might be useful biomarkers, that could supplement measures of power and connectivity.

Several differences in cross-frequency measures have been reported in different psychiatric populations in recent years (see Yakubov et al., 2022 for a review). So far, distinctions between canonical PAC and potentially wave-shape-related cross-frequency patterns have rarely been considered. Changes in wave shape have been reported explicitly for Schizophrenia (Bartz et al., 2019) and Parkinson's disease (Cole et al., 2017; Jackson et al., 2019); in both cases affecting a sensorimotor rhythm. The apparent variability of wave shapes across subjects that we have noted in the second study of this thesis (see also Schaworonkow and Voytek, 2021) may suggest a close relationship of wave-shape features to interindividual genetic variability; which might, in turn, be related to interindividual differences in perception, thought, and behavior and could, therefore, be particularly relevant for psychiatric and neurological disorders.

The specific advantages of wave shape as a neural biomarker are three-fold. First, wave shape may be used to dissociate different rhythms within the same frequency band, as we have demonstrated in the second project of this thesis. Alterations in the alpha frequency range have been reported for several different neuropsychiatric conditions (Ippolito et al., 2022). However, a disease or disorder that affects rhythmic activity in the alpha frequency band might not necessarily affect all the different rhythms in this frequency band. Different disorders might, e.g., be differentially related to changes in different underlying alpha rhythms. Therefore, with the use of wave-shape analysis that can dissociate between different alpha rhythms, disease-related changes might be more precisely attributed to the respectively affected rhythm(s) within this frequency band. Second, time-Fourier-based wave-shape analysis is not artificially restricted to a single frequency band. It specifically also extracts the relevant information that is formally localized in different sections of the spectrum, that is, the higher harmonics of a wave-shape signal. Conceptually,

FWA may be understood as a specific filter, that extracts the wave-shape information from all relevant frequencies of the spectrum, while suppressing overlapping other activity. This second advantage is closely related to the third advantage: wave-shape analysis may characterize disease-related changes of an affected rhythm in a previously unseen level of detail, since wave-shape features represent additional dimensions of information beyond the fundamental frequency and amplitude (Bartz et al., 2019). Wave shape analysis additionally incorporates the spectral phase information and cross-frequency dependencies. Therefore, wave-shape analysis may uncover differences that were previously not observable, and it could allow more specific classifications of disease related changes, that go beyond changes in power and connectivity. Because of these advantages, wave-shape analysis may substantially expand the usefulness of neural biomarkers for diagnostic purposes, and aid in the identification of potential novel targets for treatments.

Wave-shape-related neural biomarkers might be useful to plan individually adapted therapeutic interventions, or to monitor therapeutic effects. Wave shape might, e.g., be relevant for neurofeedback-, or for brain-computer-interface applications. A bispectral cross-frequency measure is already a part of the Bispectral Index (Kearse et al., 1994; Sigl and Chamoun, 1994), which is being used for monitoring and titrating general anesthesia, with several health benefits when compared to monitoring solely based on clinical parameters (Chiang et al., 2018; Oliveira et al., 2017). Moreover, it has been reported, that cross-frequency analysis might aid in the identification of seizure onset zones in extratemporal lobe epilepsy (Guirgis et al., 2015). Using Fourier-based waveform analysis in this specific application, it might be possible that emergent epileptic waveform features could be detected in earlier stages, that is, before they become dominant enough to be visible to a clinician’s eye in the time domain data. If this were the case, Fourier-based waveform analysis might be of great aid for the identification of the epileptogenic zone for surgical resection, which might improve the post-surgical outcome for patients in the future.

5.8 Invasive recordings

The first study of this thesis investigated cross-frequency relationships in non-invasive MEG recordings. The clear advantage of this non-invasive approach is the relatively complete coverage of the human cortex, which is impossible to achieve with invasive recordings. However, large-scale non-invasive measures may not reflect non-harmonic PAC that could be present at the level of cells and circuits, and which may be detectable with invasive recordings (Giehl et al., 2021). Therefore, the analysis of invasive recordings will be essential to gain a more complete overview of all cross-frequency relationships that may be relevant for brain function.

As was already pointed out before, wave-shape features represent several supplementary dimensions of information beyond the frequency, power, and connectivity of a rhythm (Bartz et al., 2019). Characteristic wave-shape features may be specifically related to underlying neurophysiological and genetic parameters that might, in turn, be related to individual cognitive or emotional characteristics. Invasive data will be essential to investigate the potential links between the detailed wave shape parameters and the underlying network activity and physiology.

A first step might be the investigation and the mapping of wave shapes that can be observed invasively using Electrocorticography (ECoG), or local field potentials (LFP); and an investigation of the relationships of these wave shapes to the local spiking activity. Spiking activity could be related to wave shapes in different ways. There might be one generic relationship between firing and oscillatory wave shape that could be functionally identical all over the brain. E.g., the likelihood of firing might be directly proportional to the amount of depolarization. In this way, many various firing patterns could, in theory, be encoded by the wave shape of an oscillation. To give only the most basic examples: waveforms with a flat, wide top on the depolarized pole and a short pointy peak on the hyperpolarized pole would be associated with relatively long-lasting and uniform spike trains and relatively short pauses of no firing; whereas single spikes at fixed intervals would be encoded by the exactly

reversed wave shape; sawtooth-like waveforms would be associated with either a slow increase and sudden stop of firing, or with a sudden start and slow decrease of firing, depending on the direction of the sawtooth; many more complex options are equally possible, including a combination of phasic- and tonic firing, as well as more than one firing window within a single oscillation cycle. A different possible relationship between oscillatory wave shapes and neuronal firing could be that firing might be proportional to the instantaneous steepness of the depolarizing flank of a periodic wave shape. It might be the case that the wave shape of oscillations specifically influences the temporal firing patterns of neurons, or vice versa, based on one such universal mechanism. Conversely, the relationship between the wave shape of an oscillation and firing may differ depending on the cortical location and the underlying networks; or depending on the different types of neurons, neurotransmitters, and receptors involved. A long-term goal would be to clarify these relationships. If this goal were reached, it might eventually be possible to make informed inferences about firing patterns and neurophysiology, e.g., about the neurotransmitter levels in a particular brain area, solely based on non-invasive recordings of wave shapes. Besides answering basic research questions, this kind of information could be incredibly valuable for diagnostic as well as therapeutic purposes.

5.9 Conclusion

The cross-frequency relationships of neuronal oscillations have been gaining interest recently because they reflect additional dimensions of information in neurophysiological recordings. Evaluated with great methodological care, these additional dimensions of information may allow novel insights into the mechanistic functions of neural oscillations.

The first study of this thesis used a systematic approach to classify human neuronal cross-frequency patterns that were recorded with MEG in resting-state as wave-shape-related (Giehl et al., 2021). Moreover, this study

demonstrated that non-sinusoidal wave shapes are a prominent and wide-spread phenomenon in the resting human brain.

Based on this result, the second study of this thesis demonstrated that cortical non-sinusoidal alpha wave shapes can be distinguished using FWA, a powerful new waveform analysis method. Thus, the prominently available wave-shape information in human MEG data was physiologically relevant. By distinguishing multiple cortical alpha waveforms based on MEG resting-state data, we showed that different alpha rhythms in the brain can be dissociated based on their waveforms.

The wave shape of neural oscillations may be closely related to the physiology of the underlying neural networks (Cole and Voytek, 2017; Krishnakumaran et al., 2022). Therefore, the wave shape of oscillations represents a promising set of biomarkers that might, eventually, permit informed inferences about underlying network physiology, -firing activity, or neurotransmitter dynamics; even based on non-invasive recordings.

Wave-shape analysis is rendered widely accessible and feasible by FWA. Thus, FWA could complement common power-spectral methods, and be widely applicable in neuroscience and beyond.

6 References

Abubaker, M., Al Qasem, W., Kvašňák, E., 2021. Working Memory and Cross-Frequency Coupling of Neuronal Oscillations. Front. Psychol. 12, 756661. https://doi.org/10.3389/fpsyg.2021.756661

Alian, A., Shelley, K., Wu, H.-T., 2022. Amplitude and phase measurements from harmonic analysis may lead to new physiologic insights: lower body negative pressure photoplethysmographic waveforms as an example. J. Clin. Monit. Comput. https://doi.org/10.1007/s10877-022-00866-6

Aru, Juhan, Aru, Jaan, Priesemann, V., Wibral, M., Lana, L., Pipa, G., Singer, W., Vicente, R., 2015. Untangling cross-frequency coupling in neuroscience. Curr. Opin. Neurobiol. 31, 51–61. https://doi.org/10.1016/j.conb.2014.08.002

Barnett, T.P., Johnson, L.C., Naitoh, P., Hicks, N., Nute, C., 1971. Bispectrum analysis of electroencephalogram signals during waking and sleeping. Science 172, 401–402.

Bartz, S., Avarvand, F.S., Leicht, G., Nolte, G., 2019. Analyzing the waveshape of brain oscillations with bicoherence. NeuroImage 188, 145–160. https://doi.org/10.1016/j.neuroimage.2018.11.045

Barzegaran, E., Vildavski, V.Y., Knyazeva, M.G., 2017. Fine Structure of Posterior Alpha Rhythm in Human EEG: Frequency Components, Their Cortical Sources, and Temporal Behavior. Sci. Rep. 7, 8249. https://doi.org/10.1038/s41598-017-08421-z

Başar, E., 2013. Brain oscillations in neuropsychiatric disease. Dialogues Clin. Neurosci. 15, 291–300. https://doi.org/10.31887/DCNS.2013.15.3/ebasar

Başar, E., Güntekin, B., 2013. Chapter 19 - Review of delta, theta, alpha, beta, and gamma response oscillations in neuropsychiatric disorders, in: Başar, E., Başar-Eroğlu, C., Özerdem, A., Rossini, P.M., Yener, G.G. (Eds.), Supplements to Clinical Neurophysiology, Application of Brain Oscillations in Neuropsychiatric Diseases. Elsevier, pp. 303–341. https://doi.org/10.1016/B978-0-7020-5307-8.00019-3

Benjamini, Y., Hochberg, Y., 1995. Controlling the False Discovery Rate: A Practical and Powerful Approach to Multiple Testing. J. R. Stat. Soc. Ser. B Methodol. 57, 289–300. https://doi.org/10.2307/2346101

Berger, H., 1929. Über das Elektrenkephalogramm des Menschen. Arch. Für Psychiatr. Nervenkrankh. 87, 527–570. https://doi.org/10.1007/BF01797193

Bonnefond, M., Kastner, S., Jensen, O., 2017. Communication between Brain Areas Based on Nested Oscillations. eneuro 4, ENEURO.0153-16.2017. https://doi.org/10.1523/ENEURO.0153-16.2017

Buzsaki, G., 2006. Rhythms of the Brain, Illustrated Edition. ed. Oxford University Press.

Buzsáki, G., Draguhn, A., 2004. Neuronal Oscillations in Cortical Networks. Science 304, 1926–1929. https://doi.org/10.1126/science.1099745

Buzsáki, G., Rappelsberger, P., Kellényi, L., 1985. Depth profiles of hippocampal rhythmic slow activity ('theta rhythm') depend on behaviour. Electroencephalogr. Clin. Neurophysiol. 61, 77–88. https://doi.org/10.1016/0013-4694(85)91075-2

Buzsáki, G., Watson, B.O., 2012. Brain rhythms and neural syntax: implications for efficient coding of cognitive content and neuropsychiatric disease. Dialogues Clin. Neurosci. 14, 345–367. https://doi.org/10.31887/DCNS.2012.14.4/gbuzsaki

Canolty, R.T., Edwards, E., Dalal, S.S., Soltani, M., Nagarajan, S.S., Kirsch, H.E., Berger, M.S., Barbaro, N.M., Knight, R.T., 2006. High gamma power is phase-locked to theta oscillations in human neocortex. Science 313, 1626–1628. https://doi.org/10.1126/science.1128115

Canolty, R.T., Knight, R.T., 2010. The functional role of cross-frequency coupling. Trends Cogn. Sci. 14, 506–515. https://doi.org/10.1016/j.tics.2010.09.001

Cardellicchio, P., Hilt, P.M., Dolfini, E., Fadiga, L., D'Ausilio, A., 2020. Beta Rebound as an Index of Temporal Integration of Somatosensory and Motor Signals. Front. Syst. Neurosci. 14, 63. https://doi.org/10.3389/fnsys.2020.00063

Carl, C., Açık, A., König, P., Engel, A.K., Hipp, J.F., 2012. The saccadic spike artifact in MEG. NeuroImage 59, 1657–1667. https://doi.org/10.1016/j.neuroimage.2011.09.020

Chacko, R.V., Kim, B., Jung, S.W., Daitch, A.L., Roland, J.L., Metcalf, N.V., Corbetta, M., Shulman, G.L., Leuthardt, E.C., 2018. Distinct phase-amplitude couplings distinguish cognitive processes in human attention. NeuroImage 175, 111–121. https://doi.org/10.1016/j.neuroimage.2018.03.003

Chella, F., Marzetti, L., Pizzella, V., Zappasodi, F., Nolte, G., 2014. Third order spectral analysis robust to mixing artifacts for mapping cross-frequency interactions in EEG/MEG. NeuroImage 91, 146–161. https://doi.org/10.1016/j.neuroimage.2013.12.064

Chiang, M.-H., Wu, S.-C., Hsu, S.-W., Chin, J.-C., 2018. Bispectral Index and non-Bispectral Index anesthetic protocols on postoperative recovery outcomes. Minerva Anestesiol. 84. https://doi.org/10.23736/S0375-9393.17.12033-X

Cole, S., Voytek, B., 2019. Cycle-by-cycle analysis of neural oscillations. J. Neurophysiol. 122, 849–861. https://doi.org/10.1152/jn.00273.2019

Cole, S.R., van der Meij, R., Peterson, E.J., de Hemptinne, C., Starr, P.A., Voytek, B., 2017. Nonsinusoidal Beta Oscillations Reflect Cortical Pathophysiology in Parkinson's Disease. J. Neurosci. 37, 4830–4840. https://doi.org/10.1523/JNEUROSCI.2208-16.2017

Cole, S.R., Voytek, B., 2017. Brain Oscillations and the Importance of Waveform Shape. Trends Cogn. Sci. 21, 137–149. https://doi.org/10.1016/j.tics.2016.12.008

Colgin, L.L., 2015. Theta–gamma coupling in the entorhinal–hippocampal system. Curr. Opin. Neurobiol. 31, 45–50. https://doi.org/10.1016/j.conb.2014.08.001

Csicsvari, J., Jamieson, B., Wise, K.D., Buzsáki, G., 2003. Mechanisms of Gamma Oscillations in the Hippocampus of the Behaving Rat. Neuron 37, 311–322. https://doi.org/10.1016/S0896-6273(02)01169-8

Debnath, R., Viola Miller, N., Morales, S., Seddio, K.R., Fox, N.A., 2020. Investigating brain electrical activity and functional connectivity in adolescents with clinically elevated levels of ADHD symptoms in alpha frequency band. Brain Res. 147142. https://doi.org/10.1016/j.brainres.2020.147142

Dellavale, D., Urdapilleta, E., Cámpora, N., Velarde, O.M., Kochen, S., Mato, G., 2020. Two types of ictal phase-amplitude couplings in epilepsy patients revealed by spectral harmonicity of intracerebral EEG recordings. Clin. Neurophysiol. 131, 1866–1885. https://doi.org/10.1016/j.clinph.2020.04.160

Dvorak, D., Fenton, A.A., 2014. Toward a proper estimation of phase–amplitude coupling in neural oscillations. J. Neurosci. Methods 225, 42–56. https://doi.org/10.1016/j.jneumeth.2014.01.002

Elgar, S., 1987. Relationships involving third moments and bispectra of a harmonic process. IEEE Trans. Acoust. Speech Signal Process. 35, 1725–1726. https://doi.org/10.1109/TASSP.1987.1165090

Fell, J., Axmacher, N., 2011. The role of phase synchronization in memory processes. Nat. Rev. Neurosci. 12, 105–118. https://doi.org/10.1038/nrn2979

Feshchenko, V.A., Reinsel, R.A., Veselis, R.A., 2001. Multiplicity of the α Rhythm in Normal Humans. J. Clin. Neurophysiol. 18, 331–344.

Fisher, N.I., 1993. Statistical analysis of circular data. Cambridge University Press, Cambridge.

Fries, P., 2015. Rhythms for Cognition: Communication through Coherence. Neuron 88, 220–235. https://doi.org/10.1016/j.neuron.2015.09.034

Fries, P., 2005. A mechanism for cognitive dynamics: neuronal communication through neuronal coherence. Trends Cogn. Sci. 9, 474–480. https://doi.org/10.1016/j.tics.2005.08.011

Fujisawa, S., Buzsáki, G., 2011. A 4 Hz Oscillation Adaptively Synchronizes Prefrontal, VTA, and Hippocampal Activities. Neuron 72, 153–165. https://doi.org/10.1016/j.neuron.2011.08.018

Gastaut, H., Terzian, H., Gastaut, Y., 1952. [Study of a little electroencephalographic activity: rolandic arched rhythm]. Mars. Med. 89, 296–310.

Gerber, E.M., Sadeh, B., Ward, A., Knight, R.T., Deouell, L.Y., 2016. Non-Sinusoidal Activity Can Produce Cross-Frequency Coupling in Cortical Signals in the Absence of Functional Interaction between Neural Sources. PloS One 11, e0167351. https://doi.org/10.1371/journal.pone.0167351

Giehl, J., Noury, N., Siegel, M., 2021. Dissociating harmonic and non-harmonic phase-amplitude coupling in the human brain. NeuroImage 227, 117648. https://doi.org/10.1016/j.neuroimage.2020.117648

Giehl, J., Siegel, M., 2024. Spectral waveform analysis dissociates human cortical alpha rhythms. BioRxiv 2024.03.16.585296. https://doi.org/10.1101/2024.03.16.585296

González, J., Cavelli, M., Mondino, A., Rubido, N., BL Tort, A., Torterolo, P., 2020. Communication Through Coherence by Means of Cross-frequency Coupling. Neuroscience 449, 157–164. https://doi.org/10.1016/j.neuroscience.2020.09.019

Gross, J., Kujala, J., Hamalainen, M., Timmermann, L., Schnitzler, A., Salmelin, R., 2001. Dynamic imaging of coherent sources: Studying neural interactions in the human brain. Proc. Natl. Acad. Sci. U. S. A. 98, 694–699. https://doi.org/10.1073/pnas.98.2.694

Guirgis, M., Chinvarun, Y., Campo, M. del, Carlen, P.L., Bardakjian, B.L., 2015. Defining regions of interest using cross-frequency coupling in

extratemporal lobe epilepsy patients. J. Neural Eng. 12, 026011. https://doi.org/10.1088/1741-2560/12/2/026011

Haegens, S., Cousijn, H., Wallis, G., Harrison, P.J., Nobre, A.C., 2014. Inter- and intra-individual variability in alpha peak frequency. NeuroImage 92, 46–55. https://doi.org/10.1016/j.neuroimage.2014.01.049

Hagihira, S., Takashina, M., Mori, T., Mashimo, T., Yoshiya, I., 2001. Practical issues in bispectral analysis of electroencephalographic signals. Anesth. Analg. 93, 966–970, table of contents.

Hari, R., Salmelin, R., Mäkelä, J.P., Salenius, S., Helle, M., 1997. Magnetoencephalographic cortical rhythms. Int. J. Psychophysiol. 26, 51–62. https://doi.org/10.1016/S0167-8760(97)00755-1

Herrmann, C.S., Demiralp, T., 2005. Human EEG gamma oscillations in neuropsychiatric disorders. Clin. Neurophysiol. 116, 2719–2733. https://doi.org/10.1016/j.clinph.2005.07.007

Hipp, J.F., Siegel, M., 2015. BOLD fMRI Correlation Reflects Frequency-Specific Neuronal Correlation. Curr. Biol. CB 25, 1368–1374. https://doi.org/10.1016/j.cub.2015.03.049

Hipp, J.F., Siegel, M., 2013. Dissociating neuronal gamma-band activity from cranial and ocular muscle activity in EEG. Front. Hum. Neurosci. 7, 338. https://doi.org/10.3389/fnhum.2013.00338

Hyafil, A., 2015. Misidentifications of specific forms of cross-frequency coupling: three warnings. Front. Neurosci. 9, 370. https://doi.org/10.3389/fnins.2015.00370

Hyafil, A., Giraud, A.-L., Fontolan, L., Gutkin, B., 2015. Neural Cross-Frequency Coupling: Connecting Architectures, Mechanisms, and Functions. Trends Neurosci. 38, 725–740. https://doi.org/10.1016/j.tins.2015.09.001

Ippolito, G., Bertaccini, R., Tarasi, L., Di Gregorio, F., Trajkovic, J., Battaglia, S., Romei, V., 2022. The Role of Alpha Oscillations among the Main

Neuropsychiatric Disorders in the Adult and Developing Human Brain: Evidence from the Last 10 Years of Research. Biomedicines 10, 3189. https://doi.org/10.3390/biomedicines10123189

Jackson, N., Cole, S.R., Voytek, B., Swann, N.C., 2019. Characteristics of Waveform Shape in Parkinson's Disease Detected with Scalp Electroencephalography. eneuro 6, ENEURO.0151-19.2019. https://doi.org/10.1523/ENEURO.0151-19.2019

Jensen, O., Bonnefond, M., VanRullen, R., 2012. An oscillatory mechanism for prioritizing salient unattended stimuli. Trends Cogn. Sci. 16, 200–206. https://doi.org/10.1016/j.tics.2012.03.002

Jensen, O., Colgin, L.L., 2007. Cross-frequency coupling between neuronal oscillations. Trends Cogn. Sci. 11, 267–269. https://doi.org/10.1016/j.tics.2007.05.003

Jensen, O., Lisman, J.E., 2005. Hippocampal sequence-encoding driven by a cortical multi-item working memory buffer. Trends Neurosci. 28, 67–72. https://doi.org/10.1016/j.tins.2004.12.001

Jensen, O., Mazaheri, A., 2010. Shaping Functional Architecture by Oscillatory Alpha Activity: Gating by Inhibition. Front. Hum. Neurosci. 4.

Jensen, O., Spaak, E., Park, H., 2016. Discriminating Valid from Spurious Indices of Phase-Amplitude Coupling. eNeuro 3. https://doi.org/10.1523/ENEURO.0334-16.2016

Jurkiewicz, M.T., Gaetz, W.C., Bostan, A.C., Cheyne, D., 2006. Post-movement beta rebound is generated in motor cortex: Evidence from neuromagnetic recordings. NeuroImage 32, 1281–1289. https://doi.org/10.1016/j.neuroimage.2006.06.005

Kearse, L.A., Manberg, P., Chamoun, N., deBros, F., Zaslavsky, A., 1994. Bispectral Analysis of the Electroencephalogram Correlates with Patient Movement to Skin Incision during Propofol/Nitrous Oxide Anesthesia.

Anesthesiology 81, 1365–1370. https://doi.org/10.1097/00000542-199412000-00010

Klimesch, W., 1999. EEG alpha and theta oscillations reflect cognitive and memory performance: a review and analysis. Brain Res. Rev. 29, 169–195. https://doi.org/10.1016/S0165-0173(98)00056-3

Klimesch, W., 1997. EEG-alpha rhythms and memory processes. Int. J. Psychophysiol. 26, 319–340. https://doi.org/10.1016/S0167-8760(97)00773-3

Klimesch, W., Doppelmayr, M., Russegger, H., Pachinger, T., Schwaiger, J., 1998. Induced alpha band power changes in the human EEG and attention. Neurosci. Lett. 244, 73–76. https://doi.org/10.1016/S0304-3940(98)00122-0

Klimesch, W., Schimke, H., Doppelmayr, M., Ripper, B., Schwaiger, J., Pfurtscheller, G., 1996. Event-related desynchronization (ERD) and the Dm effect: Does alpha desynchronization during encoding predict later recall performance? Int. J. Psychophysiol. 24, 47–60. https://doi.org/10.1016/S0167-8760(96)00054-2

Kovach, C.K., Oya, H., Kawasaki, H., 2018. The bispectrum and its relationship to phase-amplitude coupling. NeuroImage 173, 518–539. https://doi.org/10.1016/j.neuroimage.2018.02.033

Kramer, M.A., Tort, A.B.L., Kopell, N.J., 2008. Sharp edge artifacts and spurious coupling in EEG frequency comodulation measures. J. Neurosci. Methods 170, 352–357. https://doi.org/10.1016/j.jneumeth.2008.01.020

Krishnakumaran, R., Raees, M., Ray, S., 2022. Shape analysis of gamma rhythm supports a superlinear inhibitory regime in an inhibition-stabilized network. PLOS Comput. Biol. 18, e1009886. https://doi.org/10.1371/journal.pcbi.1009886

Kuhlman, W.N., 1978. Functional topography of the human mu rhythm. Electroencephalogr. Clin. Neurophysiol. 44, 83–93. https://doi.org/10.1016/0013-4694(78)90107-4

Lakatos, P., Shah, A.S., Knuth, K.H., Ulbert, I., Karmos, G., Schroeder, C.E., 2005. An Oscillatory Hierarchy Controlling Neuronal Excitability and Stimulus Processing in the Auditory Cortex. J. Neurophysiol. 94, 1904–1911. https://doi.org/10.1152/jn.00263.2005

Lehtelä, L., Salmelin, R., Hari, R., 1997. Evidence for reactive magnetic 10-Hz rhythm in the human auditory cortex. Neurosci. Lett. 222, 111–114. https://doi.org/10.1016/S0304-3940(97)13361-4

Leocani, L., Toro, C., Manganotti, P., Zhuang, P., Hallett, M., 1997. Event-related coherence and event-related desynchronization/synchronization in the 10 Hz and 20 Hz EEG during self-paced movements. Electroencephalogr. Clin. Neurophysiol. Potentials Sect. 104, 199–206. https://doi.org/10.1016/S0168-5597(96)96051-7

Lisman, J., Idiart, M., 1995. Storage of 7 +/- 2 short-term memories in oscillatory subcycles. Science 267, 1512–1515. https://doi.org/10.1126/science.7878473

Lozano-Soldevilla, D., Ter Huurne, N., Oostenveld, R., 2016. Neuronal Oscillations with Non-sinusoidal Morphology Produce Spurious Phase-to-Amplitude Coupling and Directionality. Front. Comput. Neurosci. 10, 87. https://doi.org/10.3389/fncom.2016.00087

Mathalon, D.H., Sohal, V.S., 2015. Neural Oscillations and Synchrony in Brain Dysfunction and Neuropsychiatric Disorders: It's About Time. JAMA Psychiatry 72, 840–844. https://doi.org/10.1001/jamapsychiatry.2015.0483

McLelland, D., VanRullen, R., 2016. Theta-Gamma Coding Meets Communication-through-Coherence: Neuronal Oscillatory Multiplexing Theories Reconciled. PLOS Comput. Biol. 12, e1005162. https://doi.org/10.1371/journal.pcbi.1005162

Meidahl, A.C., Moll, C.K.E., van Wijk, B.C.M., Gulberti, A., Tinkhauser, G., Westphal, M., Engel, A.K., Hamel, W., Brown, P., Sharott, A., 2019. Synchronised spiking activity underlies phase amplitude coupling in the

subthalamic nucleus of Parkinson's disease patients. Neurobiol. Dis. 127, 101–113. https://doi.org/10.1016/j.nbd.2019.02.005

Milkovich, N., Gkousioudi, A., Seta, F., Suki, B., Zhang, Y., 2022. Harmonic Distortion of Blood Pressure Waveform as a Measure of Arterial Stiffness. Front. Bioeng. Biotechnol. 10, 842754. https://doi.org/10.3389/fbioe.2022.842754

Mosteller, F., Fisher, R.A., 1948. Questions and Answers. Am. Stat. 2, 30–31. https://doi.org/10.2307/2681650

Murias, M., Swanson, J.M., Srinivasan, R., 2007. Functional Connectivity of Frontal Cortex in Healthy and ADHD Children Reflected in EEG Coherence. Cereb. Cortex 17, 1788–1799. https://doi.org/10.1093/cercor/bhl089

Nandi, B., Swiatek, P., Kocsis, B., Ding, M., 2019. Inferring the direction of rhythmic neural transmission via inter-regional phase-amplitude coupling (ir-PAC). Sci. Rep. 9, 6933. https://doi.org/10.1038/s41598-019-43272-w

Niedermeyer, E., 1991. The "Third Rhythm": Further Observations. Clin. Electroencephalogr. 22, 83–96. https://doi.org/10.1177/155005949102200208

Niedermeyer, E., 1990. Alpha-Like Rhythmical Activity of the Temporal Lobe. Clin. Electroencephalogr. 21, 210–224. https://doi.org/10.1177/155005949002100410

Nuttall, R., Jäger, C., Zimmermann, J., Archila-Melendez, M.E., Preibisch, C., Taylor, P., Sauseng, P., Wohlschläger, A., Sorg, C., Dowsett, J., 2022. Evoked responses to rhythmic visual stimulation vary across sources of intrinsic alpha activity in humans. Sci. Rep. 12, 5986. https://doi.org/10.1038/s41598-022-09922-2

O'Keeffe, A.B., Malekmohammadi, M., Sparks, H., Pouratian, N., 2020. Synchrony Drives Motor Cortex Beta Bursting, Waveform Dynamics, and Phase-Amplitude Coupling in Parkinson's Disease. J. Neurosci. 40, 5833–5846. https://doi.org/10.1523/JNEUROSCI.1996-19.2020

Oliveira, C.R.D., Bernardo, W.M., Nunes, V.M., 2017. Benefit of general anesthesia monitored by bispectral index compared with monitoring guided only by clinical parameters. Systematic review and meta-analysis. Braz. J. Anesthesiol. Engl. Ed. 67, 72–84. https://doi.org/10.1016/j.bjane.2015.09.001

Oostenveld, R., Fries, P., Maris, E., Schoffelen, J.-M., 2011. FieldTrip: Open source software for advanced analysis of MEG, EEG, and invasive electrophysiological data. Comput. Intell. Neurosci. 2011, 156869. https://doi.org/10.1155/2011/156869

Palva, J.M., 2005. Phase Synchrony among Neuronal Oscillations in the Human Cortex. J. Neurosci. 25, 3962–3972. https://doi.org/10.1523/JNEUROSCI.4250-04.2005

Pfurtscheller, G., Stancák, A., Edlinger, G., 1997. On the existence of different types of central beta rhythms below 30 Hz. Electroencephalogr. Clin. Neurophysiol. 102, 316–325. https://doi.org/10.1016/s0013-4694(96)96612-2

Pineda, J.A., 2005. The functional significance of mu rhythms: Translating “seeing” and “hearing” into “doing.” Brain Res. Rev. 50, 57–68. https://doi.org/10.1016/j.brainresrev.2005.04.005

Salmelin, R., Forss, N., Knuutila, J., Hari, R., 1995. Bilateral activation of the human somatomotor cortex by distal hand movements. Electroencephalogr. Clin. Neurophysiol. 95, 444–452. https://doi.org/10.1016/0013-4694(95)00193-X

Salmelin, R., Hari, R., 1994. Spatiotemporal characteristics of sensorimotor neuromagnetic rhythms related to thumb movement. Neuroscience 60, 537–550. https://doi.org/10.1016/0306-4522(94)90263-1

Schaworonkow, N., Voytek, B., 2021. Enhancing oscillations in intracranial electrophysiological recordings with data-driven spatial filters. PLOS Comput. Biol. 17, e1009298. https://doi.org/10.1371/journal.pcbi.1009298

Shahbazi Avarvand, F., Bartz, S., Andreou, C., Samek, W., Leicht, G., Mulert, C., Engel, A.K., Nolte, G., 2018. Localizing bicoherence from EEG and MEG. NeuroImage 174, 352–363. https://doi.org/10.1016/j.neuroimage.2018.01.044

Sheremet, A., Kennedy, J.P., Qin, Y., Zhou, Y., Lovett, S.D., Burke, S.N., Maurer, A.P., 2019. Theta-gamma cascades and running speed. J. Neurophysiol. 121, 444–458. https://doi.org/10.1152/jn.00636.2018

Sherman, M.A., Lee, S., Law, R., Haegens, S., Thorn, C.A., Hämäläinen, M.S., Moore, C.I., Jones, S.R., 2016. Neural mechanisms of transient neocortical beta rhythms: Converging evidence from humans, computational modeling, monkeys, and mice. Proc. Natl. Acad. Sci. 113, E4885–E4894. https://doi.org/10.1073/pnas.1604135113

Siebenhühner, F., Wang, S.H., Arnulfo, G., Lampinen, A., Nobili, L., Palva, J.M., Palva, S., 2020. Genuine cross-frequency coupling networks in human resting-state electrophysiological recordings. PLOS Biol. 18, e3000685. https://doi.org/10.1371/journal.pbio.3000685

Siegel, M., Donner, T.H., Engel, A.K., 2012. Spectral fingerprints of large-scale neuronal interactions. Nat. Rev. Neurosci. 13, 121–134. https://doi.org/10.1038/nrn3137

Siems, M., Siegel, M., 2020. Dissociated neuronal phase- and amplitude-coupling patterns in the human brain. NeuroImage 209, 116538. https://doi.org/10.1016/j.neuroimage.2020.116538

Sigl, J.C., Chamoun, N.G., 1994. An introduction to bispectral analysis for the electroencephalogram. J. Clin. Monit. 10, 392–404. https://doi.org/10.1007/BF01618421

Sokoliuk, R., Mayhew, S.D., Aquino, K.M., Wilson, R., Brookes, M.J., Francis, S.T., Hanslmayr, S., Mullinger, K.J., 2019. Two Spatially Distinct Posterior Alpha Sources Fulfill Different Functional Roles in Attention. J. Neurosci. 39, 7183–7194. https://doi.org/10.1523/JNEUROSCI.1993-18.2019

Tallon-Baudry, C., Bertrand, O., 1999. Oscillatory gamma activity in humans and its role in object representation. Trends Cogn. Sci. 3, 151–162. https://doi.org/10.1016/S1364-6613(99)01299-1

Tenke, C., Kayser, J., 2005. Reference-free quantification of EEG spectra: Combining current source density (CSD) and frequency principal components analysis (fPCA). Clin. Neurophysiol. 116, 2826–2846. https://doi.org/10.1016/j.clinph.2005.08.007

Tiihonen, J., Hari, R., Kajola, M., Karhu, J., Ahlfors, S., Tissari, S., 1991. Magnetoencephalographic 10-Hz rhythm from the human auditory cortex. Neurosci. Lett. 129, 303–305. https://doi.org/10.1016/0304-3940(91)90486-D

Tiihonen, J., Kajola, M., Hari, R., 1989. Magnetic mu rhythm in man. Neuroscience 32, 793–800. https://doi.org/10.1016/0306-4522(89)90299-6

Tort, A.B.L., Komorowski, R., Eichenbaum, H., Kopell, N., 2010. Measuring phase-amplitude coupling between neuronal oscillations of different frequencies. J. Neurophysiol. 104, 1195–1210. https://doi.org/10.1152/jn.00106.2010

Van der Lubbe, R.H.J., de Kleine, E., Rataj, K., 2019. Dyslexic individuals orient but do not sustain visual attention: Electrophysiological support from the lower and upper alpha bands. Neuropsychologia 125, 30–41. https://doi.org/10.1016/j.neuropsychologia.2019.01.013

van der Meij, R., Kahana, M., Maris, E., 2012. Phase-Amplitude Coupling in Human Electrocorticography Is Spatially Distributed and Phase Diverse. J. Neurosci. 32, 111–123. https://doi.org/10.1523/JNEUROSCI.4816-11.2012

Van Essen, D.C., Smith, S.M., Barch, D.M., Behrens, T.E.J., Yacoub, E., Ugurbil, K., WU-Minn HCP Consortium, 2013. The WU-Minn Human Connectome Project: an overview. NeuroImage 80, 62–79. https://doi.org/10.1016/j.neuroimage.2013.05.041

Van Veen, B.D., van Drongelen, W., Yuchtman, M., Suzuki, A., 1997. Localization of brain electrical activity via linearly constrained minimum

variance spatial filtering. IEEE Trans. Biomed. Eng. 44, 867–880. https://doi.org/10.1109/10.623056

Vaz, A.P., Yaffe, R.B., Wittig, J.H., Inati, S.K., Zaghloul, K.A., 2017. Dual origins of measured phase-amplitude coupling reveal distinct neural mechanisms underlying episodic memory in the human cortex. NeuroImage 148, 148–159. https://doi.org/10.1016/j.neuroimage.2017.01.001

Velarde, O.M., Urdapilleta, E., Mato, G., Dellavale, D., 2019. Bifurcation structure determines different phase-amplitude coupling patterns in the activity of biologically plausible neural networks. NeuroImage 202, 116031. https://doi.org/10.1016/j.neuroimage.2019.116031

Vinogradov, S., Herman, A., 2016. Psychiatric Illnesses as Oscillatory Connectomopathies. Neuropsychopharmacology 41, 387–388. https://doi.org/10.1038/npp.2015.308

von Nicolai, C., Engler, G., Sharott, A., Engel, A.K., Moll, C.K., Siegel, M., 2014. Corticostriatal coordination through coherent phase-amplitude coupling. J. Neurosci. Off. J. Soc. Neurosci. 34, 5938–5948. https://doi.org/10.1523/JNEUROSCI.5007-13.2014

White, J.A., Banks, M.I., Pearce, R.A., Kopell, N.J., 2000. Networks of interneurons with fast and slow γ-aminobutyric acid type A (GABAA) kinetics provide substrate for mixed gamma-theta rhythm. Proc. Natl. Acad. Sci. 97, 8128–8133. https://doi.org/10.1073/pnas.100124097

Wu, S., Hitchman, G., Tan, J., Zhao, Y., Tang, D., Wang, L., Chen, A., 2015. The neural dynamic mechanisms of asymmetric switch costs in a combined Stroop-task-switching paradigm. Sci. Rep. 5, 10240. https://doi.org/10.1038/srep10240

Yakubov, B., Das, S., Zomorrodi, R., Blumberger, D.M., Enticott, P.G., Kirkovski, M., Rajji, T.K., Desarkar, P., 2022. Cross-frequency coupling in psychiatric disorders: A systematic review. Neurosci. Biobehav. Rev. 138, 104690. https://doi.org/10.1016/j.neubiorev.2022.104690

7 Acknowledgments

I would like to thank my supervisor Markus Siegel for the freedom to study what I truly cared about, particularly in the second part of this project.

Thank you to my advisory board members Christoph Braun and Andreas Bartels for their genuine interest in my project, their support and their kind encouragement.

I would like to thank Joerg Hipp and Anna Antonia Pape who collected some of the data that I was allowed to use.

A special thank you goes to Paul Hege, who helped me to ensure that the mathematical appendices were formally correct and comprehensible, and to Vera Voigtländer and Paul Hege for their helpful comments on this thesis.

I am also very thankful for the existence of the Human Connectome Project, which has been a fantastic resource for the projects of this thesis. Thank you to everyone involved.

Thank you, David Röll, for your unwavering support and for being proud of me. It means a lot to me.

Appendix

Appendix A. Reconstructing the relative harmonic phase

Statement:

Equation 3 ($\phi_{\mathrm{k}} = \measuredangle e^{(-i\cdot\sum_{n=1}^{k-1}\measuredangle B(f_1, n\cdot f_1))}$) reconstructs the pairwise relative harmonic phases ϕ_{k} as the (negative) circular cumulative sum over the corresponding n=1 to n=k-1 harmonic bicoherence phases $\measuredangle B(f_1, n\cdot f_1)$. Equation 3 is valid, if the bicoherence phase captures the phase-difference between the cross-frequency coherences of two subsequent harmonic waveform components. That is, if:

$\measuredangle B(f_1, n\cdot f_1) \equiv \measuredangle(C(f_1, f_{n+1})\cdot C(f_1, f_n)^*)$ (Equation A1)

Here, $*$ denotes the complex conjugate, ≡ denotes an equivalence that we will demonstrate below, $f_{n+1} = (n+1)\cdot f_1$, $f_n = n\cdot f_1$, and cross-frequency coherence was defined as follows:

$$C(f_1, n\cdot f_1) = \frac{\langle A_{f_1}(\mathrm{t})\cdot A_{f_n}(\mathrm{t})\cdot \mathrm{e}^{i\cdot\left(\frac{f_n}{f_1}\varphi_{f_1}(t)-\varphi_{f_n}(t)\right)}\rangle}{\langle A_{f_1}(\mathrm{t})\cdot A_{f_n}(\mathrm{t})\rangle}$$

Here, $A_f(\mathrm{t})$ denotes the Amplitude time course, $\varphi_f(t)$ the phase time course and $\langle\,\rangle$ denotes the average over time.
To conserve a relative simplicity of the notation, we will be omitting the normalization factors in the derivation below.

Derivation:

Momentarily disregarding the temporal average and considering only a single point in time T with $T\epsilon t$, we can rewrite the right side of Equation A1 (without the normalization factor) as:

$\measuredangle(c_T(f_1, f_{n+1})\cdot c_T(f_1, f_n)^*) =$

$$= \measuredangle\left(A_{f_1}(\mathrm{T}) \cdot A_{f_{n+1}}(\mathrm{T}) \cdot \mathrm{e}^{i\cdot\left(\frac{f_{n+1}}{f_1}\cdot\varphi_{f_1}(T)-\varphi_{f_{n+1}}(T)\right)} \cdot A_{f_1}(T) \cdot A_{f_n}(T) \cdot e^{-i\cdot\left(\frac{f_n}{f_1}\cdot\varphi_{f_1}(T)-\varphi_{f_n}(T)\right)}\right)$$

$$= \measuredangle\left(A_{f_1}(\mathrm{T}) \cdot\ A_{f_1}(\mathrm{T}) \cdot A_{f_{n+1}}(\mathrm{T}) \cdot A_{f_n}(\mathrm{T}) \cdot \mathrm{e}^{i\cdot\left(\varphi_{f_1}(T)+\varphi_{f_n}(T)-\varphi_{f_{n+1}}(T)\right)}\right)$$

Except for a difference in amplitude weighting, this is practically identical to the bispectrum without the temporal average, and considering only a single point in time T with $T\epsilon t$. Omitting the normalization factor of bicoherence leaves the bispectrum:

$$\measuredangle b_T(f_1, f_n, f_{n+1}) =$$

$$\measuredangle\left(A_{f_1}(\mathrm{T}) \cdot A_{f_{n+1}}(\mathrm{T}) \cdot A_{f_n}(\mathrm{T}) \cdot \mathrm{e}^{i\cdot\left(\varphi_{f_1}(T)+\varphi_{f_n}(T)-\varphi_{f_{n+1}}(T)\right)}\right)$$

This equivalence remains valid when re-including the temporal averages, if and only if the following three requirements are all fulfilled: there is significant (valid) $c_{T_v}(f_1, f_{n+1})$ at some times T_v ($T_v\ \epsilon\ t$) and significant $c_{T_v}(f_1, f_n)$ at the identical times T_v and the angle $\measuredangle\left(c_{T_v}(f_1, f_{n+1}) \cdot c_{T_v}(f_1, f_n)^*\right)$ is stationary over these times T_v. Any unrelated contributions to A(t) and $\varphi(t)$ of any f_1, f_n, or f_{n+1}, that are not phase-locked to all, f_1, f_n and f_{n+1}, are expected to result in cancellation, and thus vanish, in the temporal average of bicoherence. What difference remains to $\measuredangle B(f_1, f_n)$, when these requirements are fulfilled, is a difference in amplitude weighting and –normalization, which is negligible. These three requirements are fulfilled for harmonic components of stationary non-sinusoidal periodic waveform shapes, where all three frequencies (f_1, f_n and f_{n+1}) are, by definition, jointly harmonically coupled. Thus, it is valid to use Equation 3 to reconstruct relative harmonic phases ϕ_{k} of non-sinusoidal periodic waveforms (Q.E.D.).

Appendix B. Reconstructing the relative harmonic amplitude

For a stationary non-sinusoidal periodic waveform, it holds that:

$A_k(t) = \boldsymbol{A_k} \cdot A_1(t)$ (Equation B1)

where $\boldsymbol{A_k} = const$. Here, $A_1(t)$ is the amplitude time course of the fundamental harmonic; $A_k(t)$ is the amplitude time course of the kth harmonic of the same waveform; and $\boldsymbol{A_k}$ is the constant/stationary relative harmonic amplitude of the kth harmonic in relation to the fundamental ($k = 1$) harmonic.

$$\boldsymbol{A_k} = \frac{\langle A_1(t)A_{k-1}(t)A_k(t)e^{i(\varphi_1(t)+\varphi_{k-1}(t)-\varphi_k(t))}\rangle}{\langle A_1(t)A_{k-1}(t)A_1(t)e^{i(\varphi_1(t)+\varphi_{k-1}(t)-\varphi_k(t))}\rangle}$$ (Equation 4)

The dividend of Equation 4 is the bispectrum and the divisor is a normalization factor that we designed specifically for the extraction of the relative harmonic amplitudes $\boldsymbol{A_k}$.

Equation 4 can be derived under the assumption that Equation B1 holds. For if we substitute Equation B1 into the right-hand side of Equation 4 we get:

$$\frac{\langle A_1(t)\cdot\boldsymbol{A_{k-1}}A_1(t)\cdot\boldsymbol{A_k}A_1(t)\cdot e^{i(\varphi_1(t)+\varphi_{k-1}(t)-\varphi_k(t))}\rangle}{\langle A_1(t)\cdot\boldsymbol{A_{k-1}}A_1(t)\cdot A_1(t)e^{i(\varphi_1(t)+\varphi_{k-1}(t)-\varphi_k(t))}\rangle} =$$

$$= \frac{\boldsymbol{A_{k-1}}\cdot\boldsymbol{A_k}\cdot\langle A_1(t)^3 e^{i(\varphi_1(t)+\varphi_{k-1}(t)-\varphi_k(t))}\rangle}{\boldsymbol{A_{k-1}}\cdot\langle A_1(t)^3 e^{i(\varphi_1(t)+\varphi_{k-1}(t)-\varphi_k(t))}\rangle} = \boldsymbol{A_k}$$; Q.E.D

It is important to note that Equation 4 is only valid where harmonic coupling has been established and, therefore, Equation B1 can be assumed to hold. Contributions to any A(t) and $\varphi(t)$ that are not phase-locked to the waveform signal are expected to result in cancellation and, thus, vanish in the average. For practical application, we suggest to use real($\boldsymbol{A_k}$) and to exclude any estimates with a considerable imaginary component imag($\boldsymbol{A_k}$).

Appendix C. Circular variance

Equation 6 can be derived from Equation 5 as follows. Equation 5 defines circular variance as:

$Var_{circ}(Z) = E(|Z - E[Z]|)^2 =$ (Equation 5)

$= E(Z - E[Z])E(Z - E[Z])^* =$

$= \frac{\sum(Z-E[Z])(Z-E[Z])^*}{N} = \frac{SSQ_{circ}(Z)}{N}$ (Equation C1)

$= E(Z - E[Z])E(Z^* - E[Z]^*) =$

$= E[ZZ^* - ZE[Z]^* - Z^*E[Z] + E[Z]E[Z]^*] =$

$= E[ZZ^*] - E[Z]E[Z]^* - E[Z^*]E[Z] + E[Z]E[Z]^* =$

$= E[ZZ^*] - E[Z^*]E[Z] =$

$= \frac{\sum(ZZ^*)}{N} - \frac{\sum(Z^*)\sum(Z)}{N^2} = Var_{circ}(Z)$ (Equation C2)

$= 1 - |E[Z]|$ (Fisher, 1993)

From Equation C1 and C2 it follows that:

$SS_{circ}(Z) = Var_{circ}(Z) \cdot N$

Thus:

$SS_{circ}(Z) = \sum(ZZ^*) - \frac{\sum(Z^*)\sum(Z)}{N}$ (Equation 6; Q.E.D).

As $ZZ^* = |Z|^2$ it follows further that:

$$SS_{circ} = \sum |Z|^2 - \frac{|\sum Z|^2}{N}$$

From relating SS_{circ} to $SS(X)$ with:

$$SS(X) = \sum x^2 - \frac{(\sum x)^2}{N}$$

it is trivial to conclude that additivity of variances, which is fulfilled for $SS(X)$, is also fulfilled for $SS_{circ}(Z)$. $SS_{circ}(Z)$ can alternatively also be computed as:

$SS_{circ}(Z) = N \cdot (1 - |E[Z]|\ )$

Appendix D. Composition of harmonic signals in Figure 10D

The non-sinusoidal signals in Figure 10D were generated according to:

$x(t) = \sum_{k=1}^{N} \frac{1}{w^{(k-1)}} cos(2\pi k f_1 t + (k-1)\varphi_s)$ (Equation D1)

We used $f_1 = 10Hz$, $N = 10$ and $\varphi_s = 0, 0.25\pi, 0.5\pi, 0.75\pi, \pi, 1.25\pi, 1.5\pi$ and 1.75π, respectively, for the 8 different plotted signals, starting at 0° in counterclockwise order. I defined a waveform constant w in Equation D1 as the constant fulfilling $pt_{x(t)} = \cos(\varphi_s)$, $rd_{x(t)} = \sin(\varphi_s)$ and $\sqrt{pt_{x(t)}{}^2 + rd_{x(t)}{}^2} = 1$ for $N \to \infty$; and where $\measuredangle b_{x(t)}(f_1, k \cdot f_1) = -\varphi_s$ for all $k \in [1, .., N-1]$. Here, $pt_{x(t)}$ is the peak-trough (a)symmetry and $rd_{x(t)}$ the rise-decay (a)symmetry computed over full cycles of $x(t)$, and $\measuredangle b_{x(t)}$ is the bicoherence phase angle of $x(t)$ at the frequencies specified. This waveform constant was approximated as $w = 2.34521$.

It might be that $w = \sqrt{5.5}$. To prove or disprove this was, however, far outside the scope of this thesis, so I did not attempt it.